# Experimental Study of Bubble Growth in Stromboli Basalt Melts at 1 Atmosphere

Liping Bai
Earth and Planetary Sciences
3450 University Street
McGill University, Montréal, Quebec, Canada H3A 2A7

January, 2007

**A thesis submitted to McGill University in partial fulfillment of the requirements of the degree of Master of Science**

Library and
Archives Canada

Published Heritage
Branch

395 Wellington Street
Ottawa ON K1A 0N4
Canada

Bibliothèque et
Archives Canada

Direction du
Patrimoine de l'édition

395, rue Wellington
Ottawa ON K1A 0N4
Canada

*Your file Votre référence*
*ISBN: 978-0-494-32896-5*
*Our file Notre référence*
*ISBN: 978-0-494-32896-5*

NOTICE:
The author has granted a non-exclusive license allowing Library and Archives Canada to reproduce, publish, archive, preserve, conserve, communicate to the public by telecommunication or on the Internet, loan, distribute and sell theses worldwide, for commercial or non-commercial purposes, in microform, paper, electronic and/or any other formats.

The author retains copyright ownership and moral rights in this thesis. Neither the thesis nor substantial extracts from it may be printed or otherwise reproduced without the author's permission.

AVIS:
L'auteur a accordé une licence non exclusive permettant à la Bibliothèque et Archives Canada de reproduire, publier, archiver, sauvegarder, conserver, transmettre au public par télécommunication ou par l'Internet, prêter, distribuer et vendre des thèses partout dans le monde, à des fins commerciales ou autres, sur support microforme, papier, électronique et/ou autres formats.

L'auteur conserve la propriété du droit d'auteur et des droits moraux qui protège cette thèse. Ni la thèse ni des extraits substantiels de celle-ci ne doivent être imprimés ou autrement reproduits sans son autorisation.

---

In compliance with the Canadian Privacy Act some supporting forms may have been removed from this thesis.

While these forms may be included in the document page count, their removal does not represent any loss of content from the thesis.

Conformément à la loi canadienne sur la protection de la vie privée, quelques formulaires secondaires ont été enlevés de cette thèse.

Bien que ces formulaires aient inclus dans la pagination, il n'y aura aucun contenu manquant.

Canada

# ABSTRACT

In order to investigate bubble formation and growth at 1 atmosphere, degassing experiments using a Stromboli basalt with dissolved $H_2O$ or $H_2O + CO_2$ were performed in a custom furnace on a beamline at the Advanced Photon Source. The glasses were synthesized at 1250 °C and 1000 MPa, with ~ 3.0 wt %, ~ 5.0 wt %, or ~ 7.0 wt % $H_2O$ or with mixtures of $H_2O + CO_2$, ~ 3.0 wt% $H_2O$ and ~ 440 ppm $CO_2$, ~ 5.0 wt% $H_2O$ and ~ 880 ppm $CO_2$, ~ 7.0 wt% $H_2O$ and ~ 1480 ppm $CO_2$, then heated on the beamlime while recording the bubble growth. The 3D bubble size distributions in the quenched samples were then studied with synchrotron X-ray microtomography.

The experimental results show that bubble nucleation and growth are volatile-concentration dependent. Bubbles can easily nucleate in melts initially containing high volatile concentrations. $CO_2$ has no significant effect on bubble formation and growth because of low $CO_2$ concentrations. Multiple nucleation events occur in most of these degassing samples, and they are more pronounced in more supersaturated melts. Bubble growth is initially controlled by viscosity near glass transition temperatures and by diffusion at higher temperatures where melt viscous relaxation occurs rapidly. Bubble foam forms when bubbles are highly connected due to coalescence, and bubbles begin pop, 10 to 20 seconds after the foam is developed. The degree of bubble coalescence increases with time, and bubble coalescence can significantly change the bubble size distribution. Bubble size distributions follow power-law relations at vesicularities of 1.0% to 65%, and bubble size distributions evolve from power-law relations to exponential relations at vesicularities of 65% to 83%. This evolution is associated with the change from far-from-equilibrium degassing to near-equilibrium degassing.

The experimental results imply that during basaltic eruptions both far-from-equilibrium degassing and near-equilibrium degassing can occur. The far-from-equilibrium degassing generally generates the power-law bubble size distributions whereas the near-equilibrium degassing produces exponential bubble size distributions. Bubbles begin to pop when the vesicularities attain 65% to 83%. Bubble expansion in the foam possibly accounts for the mechanism of magma fragmentation.

# RÉSUMÉ

Afin d'étudier la formation et la croissance de bulles sous pression d'une atmosphère, des expériences de dégazage sur un basalte de Stromboli, avec $H_2O$ ou $H_2O + CO_2$ dissouts, ont été exécutées dans un four pilote sous rayonnement synchrotron à l'APS (Advanced Photon Source). Les verres ont été synthétisés à une température de 1250°C et une pression de 1000 MPa, avec des teneurs en eau dissoute de ~ 3.0, ~ 5.0 ou ~ 7.0% (en poids), et des mélanges $H_2O + CO_2$ à teneurs de ~ 3.0% $H_2O$ (en poids) et 440 ppm $CO_2$, ~ 5% $H_2O$ et 880 ppm $CO_2$, et de ~ 7.0% $H_2O$ et 1480 ppm $CO_2$. La croissance des bulles est enregistrée pendant le chauffage du mélange en utilisant le rayonnement synchrotron. Les distributions tridimensionnelles de la taille des bulles dans les échantillons trempés ont été étudiées par microtomographie à rayon X synchrotron.

Les résultats expérimentaux démontrent que la nucléation et la croissance des bulles dépendent de la concentration des substances volatiles. Les bulles peuvent facilement germer dans les fontes contenant des teneurs initiales élevées en substances volatiles. En raison de sa faible concentration, le $CO_2$ n'a aucun effet significatif sur la nucléation et la croissance des bulles. Des évènements multiples de nucléation se produisent dans la majorité de ces échantillons de dégazage, et ces évènements sont plus prononcés dans les fontes plus fortement sursaturées. Dans la région des températures de transition du verre, la croissance des bulles est contrôlée par la viscosité. Aux température plus élevées, où la relaxation visqueuse se produit rapidement, la diffusion contrôle la croissance des bulles. Une mousse de bulle se forme lorsque les bulles sont fortement connectées à cause du phénomène de coalescence. Les bulles commencent à se désintégrer dix à vingt secondes après l'apparition de la mousse. Le degré de coalescence des bulles augmente avec le temps, et leur coalescence peut changer significativement leur distribution de taille. A basse vésicularité, (de 1.0 à 65%), la distribution de taille des bulles suit la loi des puissances. A vésicularité élevée (de 65 à 83%) la distribution de taille évolue d'une relation de loi des puissances à une relation exponentielle. Cette évolution est associée à une transition d'un dégazage en déséquilibre au dégazage en quasi-équilibre.

Les résultats expérimentaux démontrent que pendant les éruptions basaltiques le dégazage peut se produire en déséquilibre ou en quasi-équilibre. Un dégazage qui n'a pas lieu à l'équilibre résulte en une distribution exponentielle de taille des bulles. Les bulles commencent à se désintégrer quand la vésicularité atteint de 65 à 83%. L'expansion des bulles dans la mousse explique probablement le mécanisme de fragmentation magmatique.

# ACKNOWLEDGEMENTS

Thirty three degassing experiments were performed in my work. Three degassing experiments were performed at our lab. Thirty in-situ degassing experiments were performed at GeoSoilEnviroCARS (Sector 13), Advanced Photon Source (APS), Argonne National Laboratory. GeoSoilEnviroCARS is supported by the National Science Foundation-Earth Sciences (EAR-0622171), Department of Energy-Geosciences (DE-FG02-94ER14466) and the State of Illinois. Use of the Advanced Photon Source was supported by the U.S. Department of Energy, Office of Science, Office of Basic Energy Sciences, under Contract No. DE-AC02-06CH11357.

I thank for Don Baker's critical suggestions and comments on my experiments and writing. I also thank him for his encouragement for me to challenge the frontiers of the research fields. He likes to push me to go out to feel the life in McGill and Montreal. I also thank for my colleagues, Yanan Liu, Maria Alletti and Naji-Tom Samaha who have worked in our lab. To work with them gave me a wonderful experience in my life. I acknowledge Mark Rivers' helpful information and suggestions on the tomography analysis during my work at APS. I also thank for Lang Shi for giving me the opportunity to do electron microscope analysis. I acknowledge support of this work from the Department of Earth and Planetary Sciences, McGill University.

# Table of Contents

# 1 INTRODUCTION

The physical processes driving volcanic eruptions have been investigated by numerous experiments (e.g., Stein and Spera, 1992; Martel and Bureau, 2001; Mangan et al., 2004) and simulations (e.g., Proussevitch and Sahagian, 1996, 1998; Zhang, 1999). All of these studies relate the stresses driving eruptive behavior to magma degassing. During magma ascent from the chamber to the surface pressure decreases and the volatiles dissolved at depth exsolve to form gas bubbles due to the decreasing solubility of volatiles (Sparks, 1978). This is the basic origin of all volcanic degassing activity. Obviously, magma degassing is an important process that will cause the magma density to decrease, decompression rate to increase, and hence the flow to accelerate, finally leading to an eruption. The degassing also influences the volcano eruption style. Whether an eruption is explosive or effusive mainly depends on the behavior of the gas phase within the magma. Generally, rapid bubble formation in the magma can result in violent explosive eruptions, whereas slow bubble formation results in effusive eruptions (Yamada et al., 2005); this is because rapid expansion of the gas phase can result in the dramatic acceleration of the vesiculating magma, leading to sudden, violent explosions (Wilson, 1980).

The magma degassing process consists of two fundamental processes, bubble nucleation and bubble growth. Magma degassing starts with bubble nucleation. Magmas can nucleate bubbles during storage at depth, as shown by the 1991 eruption of Pinatubo volcano and the Bishop Tuff eruption of Long Valley Caldera, which trapped magmas in melt inclusions that contained bubbles at depth (Wallace et al., 1999). As a magma rises, the pressure of the magma decreases and becomes less than the solubility pressure of volatiles. When the degree of supersaturation becomes large enough, bubbles nucleate. The phenomenon of nucleation is essentially an energy exchange process that follows classical nucleation theory (Toramaru, 1995). The activation energy required to create a stable bubble nucleus is supplied by the vaporization energy of the volatile species in the supersaturated silicate melt (Mangan et al., 2004). Following Hurwitz and Navon (1994), this can be described by:

$$\Delta F = \frac{16\pi\sigma^3}{3\Delta P^2}$$

where $\Delta F$ is the Helmholtz free energy required to form the curved bubble interface separating the gas from melt; the excess pressure, $\Delta P$, is the difference between the ambient pressure and the equilibrium vapor pressure of the melt; and $\sigma$ is the surface free energy at the gas-melt interface. Two kinds of nucleation exist; homogeneous nucleation requires high volatile supersaturation in the melt whereas heterogeneous nucleation occurs on crystals or any solid surface and requires less supersaturation (Mangan et al., 2004). Nucleation of bubbles can control the behavior of the gas phase in conduits and the vesiculation dynamics.

Bubble growth is controlled by two distinguishable components. One component is diffusive bubble growth due to the diffusion of the volatiles from the supersaturated melt to the bubble. Diffusive bubble growth occurs at a constant pressure and it is irreversible. The second component is expansion of existing gas in the bubble as pressure is reduced.

It begins with the simple expansion of a bubble with constant mass, then mass is added to the bubble through diffusion from the melt in response to the reduction in solubility in order to maintain chemical equilibrium during decompression (Proussevitch and Sahagian, 1998).

One important consequence of bubble growth is the formation of magma foams. As magma moves toward the surface and the pressure acting on it decreases, existing gas bubbles expand and small new bubbles are continually created as gas exsolves further. If the total gas bubble volume fraction becomes large enough, bubbles begin to connect together to form a continuous foam phase. The formation of magma foam controls explosive eruptions (Proussevitch et al., 1993; Klug et al., 2002), which are associated with the magma fragmentation. Magma fragmentation generally occurs when the total bubble volume fraction reaches a critical value of ~ 70% to 80% (Sparks, 1978), and the depth at which magma fragmentation occurs depends on the total mass fraction of volatiles contained in the magma (Melnik, 1999). It is assumed that during magma fragmentation a bubbly or foamy magma is transformed into a gas-pyroclast dispersion (Sparks, 1978). This mode of fragmentation is believed to be the bursting of the relatively large bubbles disrupting the magma foam into pieces. Several other mechanisms to account for magma fragmentation have also been proposed, including propagation of a decompression wave (Mader et al., 1997), strain-induced magma fragmentation (Papale, 1999), and gas bubble overpressure exceeding the magma tensile strength (Zhang, 1999). These different mechanisms are controversial as to whether magma fragmentation is a consequence of the textural evolution of magma to a foam or whether magma fragmentation is just the result of stresses that exceed the tensile strength of the magma foam (Marti et al., 1999). In fact, the fragmentation process of the magma may evolve differently due to variations in the decompression rates, magma compositions and bubble content. The textures observed in tube pumices from Romadas Caldera (Central Andes, NW Argentina) indicate that bubble growth, stretching and shearing occur simultaneously, and that all these precede magma fragmentation (Marti et al., 1999). Recently, Gonnermann and Manga (2003) provided a new proposal, opposite to the common views that have been presented, proposing that explosive volcanism may not be an inevitable consequence of magma fragmentation; this is because of the generation of intermittent permeable fracture networks generated by non-explosive fragmentation near the conduit walls, which may be important for magma degassing. Thus, finding the fragmentation mechanism is the key to resolving the above controversy. The dynamics of textural evolution of magma to a foam can shed light on magma fragmentation, therefore magma vesiculation experiments under different conditions of pressure, temperature, volatile concentration, and time need to be conducted.

Up to now magma degassing was mainly investigated by experimental degassing studies, complex numerical simulations or measuring vesicles in natural pumice clasts. Various degassing experiments at high pressures were conducted on rhyolite (Hurwitz and Navon, 1994; Gardner et al., 1999; Larsen and Gardner, 2000; Martel and Bureau, 2001; Larsen et al., 2004; Mangan et al., 2004) and albite (Baker et al., 2006). These high pressure degassing experiments were performed by isothermal decompression and bubble formation and growth were controlled by isothermal degassing, therefore volatile exsolution was not influenced by thermal effects. Bubble nucleation and growth were controlled by decompression rate, melt viscosity, and volatile contents. Meanwhile, bubble nucleation and bubble growth dynamics in silicate melts have been explored through complex numerical models (Sparks, 1978; Proussevitch et al., 1993; Proussevitch and Sahagian, 1998). Both experimental work and simulation models have provided us information about bubble growth and bubble nucleation in silicate melts.

Recently, numerous textural investigations on natural samples of pumice, scoria or basaltic lava have been conducted (e.g., Fink et al., 1992; Gaonac'h et al., 1996; Mangan and Cashman, 1996; Marti et al., 1999; Klug et al., 2002). These studies provide data on the key parameters of bubble size distributions, the number density of bubbles, the bubble growth rate, and the vesicularity. The bubble size distribution is one of the most important parameters that is controlled by the processes of bubble nucleation and bubble growth. The cumulative bubble number density combines information about the statistical distribution of bubble sizes and density in the sample, so the distribution and probability density functions can be linked through the cumulative bubble number density (Marsh, 1988; Lovejoy et al., 2004). Gaonac'h et al. (1996) and Blower et al (2001, 2002) developed exponential and power law functions to describe the bubble size distributions of volcanic rocks. They found that bubble size distributions could be characterized by variations in the power functions. Power law size distributions are described by the equation:

$$N(V) \propto V^{-(d+1)} \Rightarrow N(>V) \propto V^{-d}$$

where N(V) is the number of bubbles of a size (volume) V, N(>V) is the number of bubbles with volume greater than V, and d is the power law exponent. We choose the log logistic form of the equation to express power law bubble size distributions. Bubble size distributions mostly follow either power-law relations, exponential relations, or unimodal relations, depending on the mechanism of degassing associated with bubble nucleation and bubble growth, and upon bubble coalescence (Gaonac'h et al., 1996; Blower et al., 2001, 2002). Power-law and exponential bubble size distributions can be both observed in volcanic rocks (Blower et al., 2002) and in high pressure degassing experiments (Baker et al., 2006), suggesting that bubble size distributions may evolve with a change of degassing conditions.

It is worth pointing out that natural volcanic rocks can not provide us direct information about bubble size distributions and vesiculation upon the onset of eruption because bubble size distributions in pumice or lava can be modified by various eruption processes, including vesiculation occurring during surface advance of extrusives after a magma has reached Earth's surface (Fink et al., 1992), bubble expansion and collapse after fragmentation (Thomas et al., 1994), bubble coalescence (Cashman et al., 1994), Ostwald ripening (Herd and Pinkerton, 1997), and bubble bursting during magma fragmentation, which creates wide ranges of fragment sizes (Vergniolle et al., 1996). In addition, most previous studies of bubble size distributions were obtained from two dimensional images of bubbles and converting two dimensional (2D) structures to three dimensional (3D) structures. Transferring 2D structures to 3D structures can not resolve the problems resulting from objects with non-convex shapes or with some degree of interconnection (Sahagian and Proussevitch, 1998).

Thus, the information gained from previous studies can not reflect bubble growth and bubble size distribution on the time scale of vesiculation during eruption or magma fragmentation. Therefore, in-situ investigations of bubble formation and bubble growth under near-surface conditions are needed. Although previous studies investigating rhyolitic magma degassing at 1 bar and high temperatures indicated that magma vesiculation is affected by magma viscosity, volatile content, and the rate of volatile exsolution (Bagdassarov and Dinwell, 1993; Bagdassarov et al., 1996), until now there have been few degassing experimental studies conducted on basaltic compositions, such as the Stromboli sample investigated herein. In comparison with rhyolitic magma, basaltic magma is significantly less viscous, consequently the degassing rate as well as the bubble growth rate in basaltic magma may behave differently. Therefore investigations on Stromboli basalt magma degassing may directly provide information about the relation between the bubble formation and growth, the rate of the vesiculation process, and the intensity of magma vesiculation during explosive eruptions.

In this study in-situ degassing experiments at one atmosphere were conducted on volatile-undersaturated glasses of Stromboli basalt synthesized at 1250 °C and 1000 MPa. These glasses, with various amounts of volatiles, were heated in-situ in an X-ray beamline at one atmosphere. The bubble formation, bubble growth and bubble coalescence processes were observed in-situ using X-ray radiography. The 3D bubble size distributions in the quenched samples were then studied with synchrotron X-ray microtomography. The focus of our study was to investigate the bubble size distribution evolution during one atmosphere degassing, interactions between bubbles that may change the bubble size distributions, and related processes that control bubble formation and growth in basaltic magma systems. In particular we investigated 3D bubble size distributions in different stages of in-situ degassing to study the bubble nucleation and growth. The implications of these results for surface magma degassing as well as magma fragmentation were then considered.

# 2 EXPERIMENTAL AND ANALYTICAL METHODS

## 2.1 Experimental methods

The one atmosphere degassing experiments were conducted on hydrated glasses of Stromboli basalt. The hydrated glasses were synthesized at 1250 $^{o}$C and 1000 MPa in a piston cylinder. The starting material was a ground powder with an average grain size of 100 μm. The samples were loaded in platinum capsules, 3.0 mm in diameter and about 10 mm in length. The loaded capsules contained about 40 to 50 mg of rock powder, with one of the following combinations of volatiles: ~ 3.0 wt% $H_2O$; ~ 3.0% $H_2O$ and 440 ppm $CO_2$; ~ 5.0 wt% $H_2O$; ~ 5.0 wt% $H_2O$ and 880 ppm $CO_2$; ~ 7.0 wt% $H_2O$; ~ 7.0 wt% $H_2O$ and 1480 ppm $CO_2$. The water was distilled and deionized, and the $CO_2$ was produced by the decomposition of $MgCO_3$ added as a powder to the rock mix. To make sure that there was no water loss during welding, the capsule was weighed before and after welding. If the weight of the loaded capsule before and after welding was significantly different, the loaded capsule was not accepted for the run. In order to verify whether the capsule was sealed, the loaded capsules were put in a 110 °C oven for at least 1.0 hour and then weighed again. This heating also leads to water being homogeneously distributed in the rock powder.

Two capsules were packed in a crushible alumina cylinder with a small amount of pyrophyllite powder to ensure that the water in the melts was not lost during hydration. The alumina cylinder was put inside a 19.1 mm NaCl – pyrex – graphite furnace assembly (Baker, 2004). To start the experiment, the piston cylinder was pressurized to 200 MPa at room temperature, then the power was applied to heat the assembly and the temperature increased to 1250 °C at a rate of 100 °C/min. The pressure was increased from 200 MPa to 1000 MPa as the temperature increased. During the experiments, temperatures were measured and controlled with W5%Re-W26%Re thermocouples, positioned in the centre of the alumina cylinder in the sample assembly (Baker, 2004). After the samples were held at 1000 MPa and 1250 °C for 1.0 hour, except for sample St7 which was hydrated for 2 hours, they were isobarically quenched to 600 °C within 15 seconds. Scanning electron microscope analysis on the quenched samples shows that these quenched glasses are crystal-free and that only a few samples contained bubbles (smaller than 4 μm in diameter).

Each glass synthesized at high pressure was sectioned into chips and each chip was heated at 1 atm to a different temperature on the GSECARS (Advanced Photon Source) Synchrotron beamline in a custom furnace (Fig. 1). This technique allows us to investigate the bubble growth process at different stages of vesicularity. The X-ray beam from the bending magnet source had an energy of 20 keV. The furnace was mounted on a rotating stage in the X-ray beam. The furnace was made of Kanthal wire connected to a DC power supply which allowed temperature to be controlled directly. The sample, a chip of synthesized glass, ~ 3.0 mm in diameter and 2.0 to 3.0 mm in length, was situated in the boron nitride holder that was placed in the center of furnace. The Pt-Rh/Pt thermocouple was positioned on the top of the ceramic above the sample inside. The distance between the thermocouple and the sample is 10 mm. The temperature recorded by the voltmeter was considered as the temperature of the outside of the furnace. The calibration of the temperature at the thermocouple against the temperature in the center of the furnace was performed after the in-situ experiments. The calibration result is shown in Fig. 2. During the experiments the samples were heated at a rate of ~ 42 $^{o}$C/min to the desired temperatures at which bubble growth or bubble popping was observed, then the foamed glasses were quenched by turning off the power supply. The duration of each experiment varied from 8 to 25 minutes. The degassing process was monitored by X-ray radiography using the CCD camera which allows in-situ X-ray observation of the bubble growth and coalescence.

A small number of high pressure bubble nucleation and growth experiments were performed in the piston-cylinder. In these experiments melts were produced using the same techniques as described above, but instead of terminating the experiment by an isobaric quench from the synthesis conditions, the experiments were isothermally decompressed at approximately 82 to 90 MPa per minute to 370 or 250 MPa and held at those conditions for a duration from 0 to 360 seconds before isobaric quenching.

## 2.2 Analytical methods

The run products of the degassing experiments at 1 atm and high pressures were analysed using Synchrotron X-ray microtomography. The great advantage of this method is that we can investigate three dimensional structures of the glass samples without destroying them. In recent years Synchrotron X-ray microtomography has been used to study volcanic rocks because it can obtain 3D microstructural information including vesicle sizes, shapes, distributions, and orientations of vesicles and the other phases in the samples (Song et al., 2001). The X-ray beam had an energy of 24 keV. The resolution used in the tomography analysis was 4.85 μm. Microtomography analysis was conducted by collecting X-ray images during 180 degrees rotation with the sample rotated at 1/4 degree resolution resulting in 720 images. Transmitted X-rays were converted into visible light with a YAG phosphor screen that was imaged with a cooled CCD camera (Fig. 1).

The 3D images obtained by Synchrotron X-ray tomography were analyzed with Image J (Abramoff et al., 2004; Rasband, 1997–2005) and the Blob3D software program written by Richard Ketcham (Department of Geological Sciences, University of Texas at Austin). About 100 to 400 tomographic images of a 3D section of a sample were analyzed. In the Blob3D program, a 3D data volume consists of voxels which are equivalent to the pixels that comprise a 2D slice of image. The melt in the image is defined as the matrix component, and an individual bubble within this data volume is represented by a set of voxels, and is defined as the bubble component. Then the bubble can be separated from the melt after three steps: segmentation, separation, and extraction. The volume of individual bubbles can be measured during the extraction step. The detailed procedure can be found in the Blob3D software program by Richard Ketcham (Department of Geological Sciences, University of Texas at Austin). The main problem in synchrotron X-ray microtomography results from the ring artifacts observed in the tomographic images. The ring artifacts are mostly caused by beam position instability, and are more obvious in the less vesiculated samples in our experiments. The ring artifacts can be reduced or removed by increasing the whiteness of the background of images using the Smooth and Brightness/Contrast functions of the Image J program.

# 3 EXPERIMENTAL RESULTS

## 3.1 In-situ observations during degassing

Bubble growth and coalescence were directly observed in 30 experiments (Table 1). Bubbles nucleate easily at lower temperature in melts initially containing high volatile concentrations. Generally the temperature at which bubbles begin to nucleate and grow in melts containing pure $H_2O$ is lower than in melts containing both $H_2O$ and $CO_2$. The in-situ observations of bubble formation and growth processes are illustrated in Fig. 3. The glass began to experience thermal expansion when heated to the temperature range of 665 to 760 $^{o}$C, but X-ray microtomography analysis shows that no bubbles are detectable at this temperature. Bubble formation and growth can not be observed until the temperature attained 760 to 1160 $^{o}$C. Once the bubbles formed they grew as temperature increased, indicated by the expansion of glass, but the expansion rate was slow, suggesting that bubbles nucleated and grew at a low rate during the early stage of degassing. Rapid bubble growth occurred above 1160°C, accompanied by significant bubble expansion. With continuously increasing temperature bubbles began to coalesce within 100 to 200 s. When the bubbles were highly connected and formed a foam they popped within 10 to 20 s. The tomography analysis indicated that the vesicularities of these foams with popping bubbles vary from ~ 65% to 83%. This observation was made on most of the experiments, but a few experiments, St84c, St58a – d, and St59a – d, were significantly different.

Although these anomalous samples began to expand at low temperatures, they remained constant in shape with additional heating until ~ 800 °C at which point they remarkably began to contract slowly as temperatures were increased from 842 to 1012 °C, although no bubbles were observed. Above 1100 °C the glass began to expand again accompanied by obvious bubble growth. The phenomenon of bubble popping associated with bubble growth and coalescence was also observed in St84c, St58a, St58d and St59a at high temperatures. The contractions that occurred in these samples were probably associated with the heating history. Samples St84a – d were chips from one glass, but only one chip, St84c, was observed to contract and this chip was heated at a slower rate in comparison with St84a, d, and e. The contractions in our experiments mostly occurred in a temperature range of 816 to 895 °C, above the glass transition temperatures of basalts measured by Giordano et al. (2005). However the detailed physical mechanism responsible for the contraction is difficult to determine. A possibility that can not be excluded is that these glasses contained very small bubbles formed during isobaric quenching, and these bubbles will be lost by resorption into the melt during early stages of heating which might lead to glass contraction.

During in-situ degassing, large bubble growth zones and small bubble growth zones were observed in some samples when heated to relatively low temperatures. These bubble growth zones were possibly due to the temperature gradient in the samples, because the samples were situated approximately in the center of the furnace which has the highest temperature, and there was a temperature gradient from the center to the outside of samples due to the rapid heating used in these experiments.

### 3.2 Bubble size distributions

The bubble size distributions of selected experimental run products as well as one natural Stromboli pumice are plotted in Figs. 4 and 5. The natural pumice is from the April 5, 2003 eruption of Stromboli and is the same material as ground and melted for our bubble growth experiments. The relations between normalized bubble numbers and bubble volume show the process of bubble growth with time. At shorter bubble growth times the peaks corresponding to the number of bubbles with volumes of 1000 to 10000 $\mu m^3$ are prominent in the histogram of bubble size distributions. At this stage bubbles vary significantly in size, and small bubbles with volumes of 1000 to 10000 $\mu m^3$ were dominant. The bubble size distributions vary in a narrow range (Fig. 4a). As bubbles grow with time, the number of small bubbles per unit volume decreases while the number of larger bubbles per unit volume tend to increase. As a result, bubble size distributions shift toward larger sizes, and two or three discrete peaks corresponding to different bubble populations occur. With bubble growth the first peak associated with the small bubbles decreases compared to the low vesicularity samples, and the maximum peak, which corresponds to the most abundant bubbles of medium size, shifts to the right in the histogram of bubble size distributions. A striking peak associated with small bubbles, volumes of ~ 1000 $\mu m^3$, appears above the temperature of 1189 °C, suggesting the occurrence of secondary nucleation events (Fig. 4b). In our experiments the growth of the small peak corresponding to secondary bubble nucleation with volumes of ~ 1000 $\mu m^3$ appears more prominent in the more supersaturated melts (Fig. 4d, 5f). Due to bubble growth and coalescence with time, the total number of bubbles per unit volume decreases, and bubbles become connected to form a giant bubble, reflected by the flattened slope of the histogram of bubble size distributions. At high vesicularities, above 65%, bubbles tend to evolve toward a single size, including the bubbles forming the foam.

Figures 4 and 5 also demonstrate that the bubble size distributions in degassing samples display power-law relations at early degassing stages, mostly producing a power-law exponent of 1.0 at lower vesicularities of 1% to 18% (Fig. 4a and Fig. 5a, d; Table 1). Correspondingly there is only one dominant peak in the histogram of bubble size distributions. With increasing growth the bubble size distributions of these samples display power-law relations with higher exponents of 1.2 to 1.8, and some tend to display a power-law relation with an exponential tail for the vesicularity range of 18% to 65% (Fig. 4b and Fig. 5e). Bubble size distributions in the run products with vesicularities below 65% are consistent with the natural sample that displays a power-law relation with an exponent of 1.0 (Fig. 4e). The most remarkable variation in the bubble size distributions is the evolution from power-law toward exponential at vesicularities of 65%

or greater (Fig. 4c, d and Fig. 5b, c, f). This observation is common in most of these highly vesiculated samples except sample St53a and St59a, where bubble size distributions still display a power-law relation at vesicularities of 75.86% and 82.3%.

In the high pressure degassing experiments bubbles tend to be of similar size, and all bubble size distributions display an exponential relation at vesicularities of 1.6 % to 15.8% (Fig.6).

### 3.3 Bubble foam structures and vesicularities

Microtomography of the run products indicates that bubbles are inhomogeneously distributed at low temperature. Most bubbles are not spherical in shape, but the non-spherical bubbles evolve to spherical bubbles as bubble growth time and temperature increase. The bubble structures in the melts indicate that coalescence takes place at low temperatures and is characterized by thinning and rupture of walls between the larger and smaller bubbles at an early stage. At higher temperatures coalescence is characterized by bubbles of similar size merging to form a large bubble. Due to bubble growth and coalescence, foams form in the melts, and the volumes of the foams vary between $10^{-3}$ $mm^3$ and 4.5 $mm^3$. The foam structures can form at either low or high temperatures (Fig. 7a – d). The foams at low temperatures consist of a small number of bubbles with significant differences in size, and the foams at high temperatures are generally formed by bubbles of similar size. 3D images of foams show that the thickness of walls between two bubbles varies significantly at low temperatures, which is in sharp contrast with those of samples quenched at high temperatures.

The structures of the bubble foam in St7a, b, c were different from those in the other samples. As illustrated by Fig. 8, at temperatures in the range of 925 to 1160 °C, most of the bubbles in samples St7a, b, c are spherical, and they are coalesced to form large bubbles which are surrounded by small bubbles. The bubbles are more homogeneous at low temperatures in comparison with the other samples, suggesting that bubbles already nucleated and grew below 925 °C. This implies that bubbles in St7 St7a, b, c began to nucleate at relatively low temperatures.

The temperature range over which non-spherical bubble foams transformed into spherical bubble foams is small, approximately 20 to 60 °C, implying that once bubbles nucleate and grow in the late stage of degassing, temperature does not have a significant effect on bubble growth. The foam structures vary significantly within a narrow temperature range. This significant transition takes approximately 30 to 85 s, suggesting that transitions from non-spherical bubble foam structures to spherical bubble foam structures occur rapidly.

# 4 DISCUSSION

## 4.1 Relation between bubble growth and glass transition temperature

The in-situ degassing observations show that the temperatures at which bubbles began to nucleate and grow is volatile-concentration dependent. The vesicularities of samples vary from 1.01% to 82.57%, depending on the degassing history. Generally bubbles grow at relatively low temperatures in melts initially containing high volatile concentrations. In melts containing ~ 3.0% $H_2O$ or ~ 3.0% $H_2O$ and 440 ppm $CO_2$, bubbles began to nucleate and grow in the temperature range of ~ 1100 to 1160 °C, while bubbles began to nucleate and grow in the temperature range of ~ 760 to 930 °C in melts initially containing ~ 7.0% $H_2O$ or ~ 7.0% $H_2O$ and 1480 ppm $CO_2$. This illustrates that different concentrations of volatiles in the melts affect bubble nucleation and bubble growth in basaltic melts. According to the results of calorimetric measurements by Giordano et al. (2005), hydrous basalt glass transition temperatures are in the range of 500 to 700 °C, depending on the volatile concentration. The temperature at which bubble nucleation and growth were observed lies in the range of ~ 760 to 1160 °C, which is above the basalt glass transition temperatures. Our observations indicate that bubble nucleation and growth occur above the glass transition temperature, and that our observations of bubble nucleation and growth and are in supercooled basaltic melts, not glass. Experimental examination also indicates that below or across the glass transition temperature water does not exsolve from the hydrous samples (Giordano et al., 2005). It is well known that the glass transition temperatures are affected by thermal history (Giordano et al., 2005; Mysen and Richet, 2005). In our experiments the temperature at which bubble nucleation and growth were observed spans a wide range of ~ 760 to 1160 °C. The wide temperature difference may be due to the fast heating rate during our degassing experiments. During our experiments the heating rate is controlled to be about 42 K/min, which is significantly higher than that of Giordano et al. (2005), 5 K/min. The high temperature at which bubbles begin to nucleate and grow during some of our experiments is attributed to the fast heating rate, which shifts the glass transition temperatures to high values (Mysen and Richet, 2005).

In our experiments bubble nucleation and growth rates in the temperature interval near the glass transition is low; slow bubble growth lasts for 20 to 200 s. Bubble growth is characterized by volume expansion at this stage. When samples are heated to temperatures far above the glass transition temperature, bubbles grow rapidly and last for 10 to 20 s before popping. Bubble growth is characterized by coalescence and expansion at this stage. The slow initial growth rate was also observed in other studies, and it is regarded as a result of the surface tension and/or melt viscosity affect (Sparks, 1978; Navon et al., 1998). In comparison to previous numerical and experimental studies (e.g., Sparks, 1978; Navon et al., 1998), we suggest that the slow initial growth rate results from high melt viscosity near the glass transition temperature. Because our degassing is under constant pressure, bubble growth can be constrained by the model of Navon et al. (1998). According to Navon et al. (1998), bubble growth under constant ambient pressure in supersaturated melts can be expressed by:

$$P_g - P_f = \frac{2\sigma}{R} + 4\eta\frac{\upsilon_R}{R} \qquad (1)$$

Where $P_g$ is the gas pressure in the bubble, $P_f$ is the ambient pressure, $\sigma$ is the surface tension, $\upsilon_R$ is bubble growth rate, R is the bubble radius, and $\eta$ is the melt viscosity. For one atmosphere degassing $P_g - P_f$ is constant. Bubbles obtained in the initial stage of our experiment are relatively large ($R \geq 5.5$ μm) and therefore the surface tension contribution can be ignored. Hence the initial bubble growth rate is viscosity dependent ($\upsilon_R \sim R/4\eta$). The observed bubble volume expansion also suggests that bubble growth at this stage is limited by viscosity (Bagdassarov and Dingwell, 1993). This is inconsistent with the high pressure degassing model where bubble growth in basalt melt is supposed to be limited only by volatile diffusion as viscous relaxation is relatively rapid in low viscosity melts (Proussevitch and Sahagian, 1998). Our experiments allow us to examine the time scale of viscosity controlled bubble growth and diffusion-controlled bubble growth based on the calculation of the time scale for $\tau_v$ and $\tau_d$ (Navon et al., 1998):

$$\tau_v = \frac{\eta}{\Delta P} \qquad (2)$$

$$\tau_d = \frac{R^2}{D} \qquad (3)$$

where $\tau_v$ is time scale for viscous deformation controlled bubble growth, and $\tau_d$ is time scale for diffusion controlled bubble growth. R is bubble radius, D is the diffusion coefficient of water, and $\eta$ is the melt viscosity. Based on the viscosity investigation of Giordano and Dingwell (2003), we estimate the viscosity near the glass transition temperature at $10^5$ to $10^7$ Pa s and 10 to 100 Pa s at temperatures above 1200 $^{o}$C; the diffusion coefficient of water is estimated to be ~ $10^{-11}$ m$^2$ s$^{-1}$ (Lyakhovsky et al., 1996). We calculate $\tau_v$ is in the range of 1 to 100 s near the glass transition temperature, and $\tau_d$ is in the range of 1 to 3 s for bubbles with radii 5 to 6 μm. These are approximately consistent with our in-situ observations showing that the slow bubble growth stage generally lasts for 20 to 100 s, and rapid bubble growth lasts for 10 to 20 s. The good agreement between our calculation based on the model of Navon et al. (1998) and our experimental observations suggest that bubble growth is controlled by viscosity in the early stage and diffusion in the later stage of our experiments. The bubbles are non-spherical at the early stage of bubble growth. This is possibly due to the high melt viscosity which limits the ability of melt relaxation to produce a spherical bubble shape in the low-temperature, early stage of bubble growth.

Our experiments proceed from low temperature to high whereas in nature it is expected that bubble growth begins at high temperature and continues to low. Thus, if vesiculation begins in a basaltic magma at near-liquidus conditions diffusion should control bubble growth. However, if vesiculation does not occur until near-solidus conditions in the basaltic magma chamber there is the potential for viscosity controlled bubble growth.

### 4.2 Evolution of bubble size distributions

To determine the type of distribution that best fits the data we fit both an exponential and a power-law function to bubble size distributions. Our results demonstrate that bubble size distributions display a strong correlation with the vesicularity of samples as illustrated in Figs. 4 and 5. At vesicularities of 2.9% to 29.1% bubble size distributions display power-law relations with power-law exponents of 0.92 to 1.0, as indicated by the correlation coefficient of the power-law fit to the cumulative bubble number density and bubble volume, which is near 0.99 for most of these samples. We selected the same range of volumes and fit an exponential function to bubble size distributions in these samples which did not clearly display exponential behaviour (Fig. 4a, b and Fig. 5a, d, e). As bubbles grow with time the vesicularity increases and bubble size distributions tend to display a power-law with a steeper exponent. As bubble growth continues bubble size distributions tend to evolve toward exponential relations at vesicularities of 65% to 83%; this is verified by our fit for the cumulative bubble number density. The exponential correlation coefficients for experiments with vesicularities greater than 65% range from 0.96 to 0.98, which is similar to the power-law correlation coefficients ranging from 0.97 to 0.98 (Fig. 4c, d and Fig. 5b, c, f). Based on these observations we infer that at vesicularities below 65% bubble size distributions follow a power-law relation; at vesicularities above 65% bubble size distributions follow an exponential relation for most of the samples, suggesting that there is a transition from a power-law to an exponential bubble size distribution as degassing and bubble growth continue with time.

The exponential bubble size distributions observed at 1 atm suggest that the degassing systems attain near-equilibrium degassing conditions; this is supported by the high pressure degassing results where all bubble size distributions follow exponential functions (Fig.6). In the high pressure degassing experiments the water remains in the capsule and the system attains near-equilibrium, resulting in exponential bubble size distributions. During the degassing experiments at 1 atm, when bubble growth is controlled by diffusion at a vesicularity above 65%, volatile diffusion is rapid enough to allow the system to reach near-equilibrium degassing. Theoretical models also indicate that basaltic melts with significantly lower viscosities and faster water diffusivities should degas in equilibrium even at fast decompression rates (Proussevitch and Sahagian, 1996, 1998). The mechanisms for producing power-law or exponential law distributions have been also investigated by previous studies (Gaonac'h et al, 1996; Blower et al., 2001). These studies show that far-from-equilibrium degassing associated with multiple nucleation events and bubble coalescence are the most plausible mechanisms for generating the power-law bubble size distributions. Therefore we conclude that degassing in our experiments at a vesicularity below 65% is controlled by far-from-equilibrium degassing whereas at a vesicularity above 65% degassing is at near-equilibrium conditions. In some more supersaturated melts degassing still displays power-law bubble size distributions at a vesicularity above 65%; this is possibly the result of multiple nucleation events (discussed below).

### 4.3 Multiple nucleation events

The information gained from the bubble size distributions as well the foam structures in the melts indicates the occurrence of multiple nucleation events during our experiments. As illustrated by the histograms of bubble size distributions (Figs. 4, 5), small bubbles, as indicated by the small peak at ~ 1000 $\mathrm{um}^3$, are not present at short bubble growth times, but as degassing continues small bubbles begin to form. Two dimensional images and three dimensional foam structures also indicate that the melt pockets between the larger bubbles with volumes of $10^4$ to $10^6$ $\mu\mathrm{m}^3$ are occupied by the smaller bubbles with volumes of $10^2$ to $10^3$ $\mu\mathrm{m}^3$ nucleated during a later stage (Fig. 7c, d). These observations suggest that during the degassing process the first generation of bubbles grows rapidly once nucleated. Because these bubbles deplete the volatiles in the surrounding melt during their growth, there is no more nucleation in the region surrounding the first generation of bubbles early in their growth. As degassing continues, the volatiles in the melt pockets between the larger bubbles nucleate new bubbles, resulting in secondary nucleation events. This interpretation is consistent with Blower et al.'s (2002) and Yamada et al.'s

(2005) results. This observation of multiple nucleation events in our experiments is more obvious in the samples containing high volatile concentrations, suggesting that multiple nucleation events are more pronounced in the more supersaturated melts, as expected.

The effect of multiple nucleation events on the dynamics of the degassing process remains a problem. In our experiments the second generation bubbles not only affect the total bubble number density, but also influence the bubble size distributions. At high vesicularity most bubble size distributions tend to evolve to exponential bubble size distributions; however in some experiments the bubble size distributions still display a power-law relation with a high power-law exponent of 1.0. This is possibly attributed to multiple nucleation events. Previous studies also suggested that power-law bubble size distributions can result from several nucleation events in the volatile-rich melt pockets between existing bubbles (Blower et al., 2002). However, Yamada et al.'s (2005) model indicates that multiple nucleation events do not always result in the formation of a power-law bubble size distributions, because nucleation in the volatile-rich regions terminates after a short duration due to the quick filling up of the region surrounding the first generation of bubbles by the second generation of bubbles.

### 4.4 Bubble coalescence

The X-ray microtomography indicates that bubble coalescence occurs simultaneously with bubble expansion at vesicularities above 18%, but at vesicularities of 1% to 18% although some bubble coalescence is observed, most bubbles are distributed separately and inter-bubble distances range from 10 to 25 μm, as a result they are not close enough to affect each others' growth, implying coalescence is not dominant at the early bubble growth stage. Our experimental results show that bubble coalescence affects the evolution of bubble populations and the development of foam structures. Coalescence decreases the number of small bubbles with volumes of $10^2$ to $10^3$ μm$^3$, increases the number of medium bubbles with volumes of $10^4$ to $10^5$ μm$^3$, and consequently changes the bubble size distributions, as illustrated in Figs. 4 and 5. However, other studies indicated that the structure of foams can also be altered by Ostwald ripening characterized by steady diffusive transfer of gas between bubbles through films during bubble growth (Mangan and Cashman, 1996; Herd and Pinkerton, 1997; Larsen et al., 2004). Ostwald ripening is driven by the pressure excess inside bubbles, which is high for small bubbles and low for large bubbles according to the Young - Laplace law, and results in gas transfer from the smallest to the largest bubbles (Herd and Pinkerton, 1997). However, in our experiments bubble interaction is dominated by bubble coalescence, and no Oswald ripening is observed.

The coalescence rate is one of the most important factors controlling the degassing mechanism (Herd and Pinkerton, 1997). In our experiments coalescence is observed to occur accompanied by expansion, and the coalescence rate increases with time. Bubble coalescence rates depend on the timescale of thinning of the melt film separating two bubbles to a critical value, film rupture, and relaxation (Navon et al., 1998). Studies have investigated coalescence rates based on the properties of the phase and particle size (Herd and Pinkerton, 1997). In our experiments we can not measure the coalescence rate directly. The in-situ observations and bubble structures show that at vesicularities below ~

18% bubble coalescence is very slow and bubble growth is dominated by expansion at this stage. At vesicularities of ~ 18% to 65% coalescence is accompanied by expansion, but coalescence is more pronounced due to the increase of bubble number and decrease of inter-bubble distances. But the bubble coalescence rate is still relatively low. Through comparison of bubble structures and in-situ observations in this vesicularity range we suggest that slow coalescence results from the relatively high melt viscosity. Because bubble growth is limited by viscosity at this stage, it takes a longer time for a coalesced pair of bubbles to thin the wall between them, relax and obtain a spherical shape. Bubble coalescence occurs rapidly once viscosity controlled bubble growth is transformed to diffusion controlled growth. Particularly at vesicularities of ~ 65% to 83% coalescence can lead to bubble popping within 10 s after foams were formed. This is possibly because coalescence results in the dramatic expansion of bubbles. Previous studies suggested that the rate of increase of bubble radius due to coalescence is dependent on the mechanism of disruption (Proussevitch et al., 1993). If coalescence occurs by rupture of inter-bubble films, bubble radius grows as $\tau^{1/3}$ and if coalescence occurs by rupture of plateau borders, it grows as $\tau$, but our observations are not precise enough to measure the difference between these power laws. Maybe at the high vesicularity when foam forms, the connected bubbles are relatively large ($\geq \sim 10^{-4}$ mm$^3$), and plateau borders are less stable than melt films (Proussevitch et al., 1993). In this case, bubble coalescence occurs by rupture of plateaus, and as a result, bubbles expand rapidly, leading to bubble popping.

Coalescence plays an important role in volcanic eruptions. Coalescence controls formation of magma foams (Lovejoy et al., 2004) and influences the bubble number density and bubble size distribution (Gaonac'h et al., 1996; Larsen et al., 2004); this is verified by our experimental results. However the effect of coalescence on the dynamics of degassing is not well known. Based on our experimental results we suggest that coalescence accounted for the transformation from far-from-equilibrium degassing at low vesicularity to near-equilibrium degassing at high vesicularity. At low vesicularity, although coalescence increases the number of bubbles in the medium size range, the volatile concentration gradient between the bubble and the highly supersaturated melt is probably much higher (Larsen and Gardner, 2000). As a result, the bubble size distribution follows a power-law relation associated with far-from-equilibrium degassing. As bubble coalescence proceeds with the increase of vesicularitiy, bubble volumes tend to be sub-equal, and coalescence consequently leads to the formation of a spherical foam with bubbles of the same size, and the melt film is strongly thinned between bubbles. The plateau between bubbles is significantly reduced to the order of $10^2$ to $10^3$ $\mu m^2$. Meanwhile bubble coalescence increases the interfacial area of foam and reduces the surface area of bubbles (Proussevitch et al., 1993). At this stage the volatile concentration gradient is small and highly localized around the bubble (Larsen and Gardner, 2000). As a result, volatile diffusion from the supersaturated melts toward the bubble-melt interface becomes fast and degassing evolves into near-equilibrium degassing.

### 4.5 Effect of $CO_2$ on degassing

Recently, a great deal of attention has been focused on the eruptive behavior of volcanoes with different concentrations of water as well as different bubble contents (Allard et al., 1991; Mader et al., 1994). In natural magma systems the concentration of $CO_2$ is commonly thought to be far below that of water (Stein and Spera, 1992); however, $CO_2$ may play an important role in the degassing of a magma system, as a relatively small amount of $CO_2$ in the magmatic gas can significantly affect the gas saturation pressure (Holloway and Blank, 1994) and change the distribution of volatiles in a magma system (Sparks et al., 1999). Our experiments indicate that bubbles can nucleate and grow in a relatively shorter time or at lower temperatures to form a foam with a vesicularity of ~ 65% to 83% in melts containing pure $H_2O$ compared to conditions with both $H_2O$ and $CO_2$, suggesting that bubbles nucleate and grow relatively slowly in melts containing $CO_2$. However it is hard to assume that this phenomenon results from the affect of $CO_2$ on melt properties that control degassing, as $CO_2$ concentration is very low in our experiments. Simulations also indicate that $CO_2$ has no effect on magma properties when its content is of the order of tens to hundreds of ppm (Papale and Polacci, 1999). The bubble size distributions in $H_2O$-containing melts or $H_2O$- and $CO_2$-containing melts reveal no obviously different behavior, suggesting that $CO_2$ has a negligible effect on bubble size distributions under our experimental conditions. However the effects of large concentrations of dissolved $CO_2$ on the dynamics of degassing need to be investigated by future experimental measurements.

### 4.6 Implications

The bubble size distributions in our degassing samples with vesicularities below 65% are consistent with the natural rock sample which also displays a power-law bubble size distribution. The foam structures of the natural sample indicate that the bubbles coalesced to form a huge bubble with small bubbles imbedded in the pockets between large bubbles.

The only significant difference between experiments and the natural sample is that most of the bubbles in the natural sample are preferentially aligned due to flow.

Similar power-law bubble size distributions are also pronounced in the other natural volcanic rocks. Bubble size analysis on basaltic lavas from Mount Etna also indicated that bubble size distributions follow a power-law relation, but the power-law exponents vary significantly in different samples (Gaonac'h et al., 1996). Blower et al. (2002) analyzed the bubble size distribution in scoria samples from the basaltic sub-Plinian eruption of Izu-Oshima, Japan and found both power-law and exponential bubble size distributions. The mechanism of continuous coalescence (Gaonac'h et al., 1996) or multiple nucleation events (Blower et al., 2002) accounts for the power-law bubble size distributions. Our results imply that bubble size distributions during basaltic degassing depend on the evolution of the degassing system. When degassing occurs by far-from-equilibrium degassing, multiple nucleation events are pronounced, which generate power-law bubble size distributions. When the system reaches near-equilibrium degassing, bubble coalescence is dominant, which results in exponential bubble size distributions. Whether degassing occurs by far-from-equilibrium degassing or near-equilibrium correlates with the vesiculation and degree of supersaturation, and this change in degassing types occurs rapidly in basaltic magmas.

Our experimental results also provide information about magma fragmentation. The experiments show that foams begin to collapse when vesicularities attain ~ 65%, lower than the critical value of 70% to 80% for magma fragmentation (Sparks, 1978). The contrast in the value between the experimental studies and natural samples may result from different shapes of bubbles, different bubble size ranges, and different pressures of bubble growth. The vesicle size distribution in lava from Kilauea also indicates an average vesicularity of 66% when bubbles are spherical in shape (Mangan et al., 1993). This is similar to our experimental results, suggesting that magma fragmentation can be affected by the shapes and sizes of bubbles in the magma foam. In our experiments once a spherical foam is formed in the magma, bubbles rapidly pop by expansion, within 10 to 20 seconds. Bubble popping resulted from coalescence and expansion, which in nature is controlled by the pressure difference between the bubbles and the mixture of gas and particles above the disruption level (Vergniolle et al., 2004). In our experiments, the observation of foam collapse due to bubble expansion when vesicularities attain ~ 65% is consistent with the proposal of Sparks (1978), implying that bubble expansion in the foam possibly accounts for the mechanism of magma fragmentation. Due to the low viscosity, bubbles in basalt pop rapidly, suggesting that magma fragmentation can easily be expected to occur during basalt eruption. As basalt magma has a relatively low viscosity, the eruption due to foam collapse is less energetic in comparison to the eruption of melts of greater viscosity (Proussevitch and Sahagian, 1993).

# 5 CONCLUSIONS

(1) Stromboli basalt degassing at one atmosphere evolves from far-from-equilibrium degassing at low vesicularities, below 65%, to near-equilibrium degassing at higher vesicularities. Consequently, bubble size distributions evolve from power-law relations to

exponential relations.

(2) Multiple nucleation events are more pronounced in more supersaturated melts. Multiple nucleation events are at least partially responsible for the occurrence of power-law bubble size distributions in melts at high vesicularity.

(3) In our experiments bubble growth is initially controlled by viscosity near the glass transition where melt viscosities are high and by diffusion at higher temperatures where viscous relaxation occurs rapidly; in natural samples diffusion is expected to control bubble growth at near-liquidus temperatures.

(4) Bubble coalescence accompanied by bubble expansion can significantly change the bubble size distribution during bubble growth. During the bubble growth stage controlled by viscosity, bubble coalescence rate is slow and bubble coalescence is not obvious. The bubble coalescence rate increases significantly in the bubble growth stage controlled by diffusion.

(5) The experimental results imply that during an explosive eruption degassing occurs either by near-equilibrium or far-from-equilibrium degassing, depending on the development of the degree of supersaturation and the extent of bubble coalescence when magmas ascend from the conduit to the surface. Bubble expansion in the foam may be the mechanism responsible for magma fragmentation.

# REFERENCES

Abramoff, M D, Magelhaes P J, Ram S J, Image processing with ImageJ, *Biophotonics Inter*, 2004, 11: 36–42

Allard P, Carbonnelle J, Dajlevic D, Bronec J L E, Morel P, Robe M C, Maurenas J M, Faivre-Pierret R, Martin D, Sabroux J C, Zettwoog P, Eruptive and diffuse emissions of $CO_2$ from Mount Etna, *Nature*, 1991, 351: 387–391

Baker D R, Piston-cylinder calibration at 400 to 500 MPa: A comparison of using water solubility in albite melt and NaCl melting, *American Mineralogist*, 2004, 89: 1553–1556

Baker D R, Lang P, Robert G, Bergevin J-F, Allard E, Bai L-P, Bubble growth in slightly supersaturated albite melt at constant pressure, *Geochimica et Cosmochimica Acta*, 2006, 70: 1821–1838

Bagdassarov N S, Dingwell D B, Deformation of foamed rhyolites under internal and external stresses: An experimental investigation, *Bulletin of Volcanology*, 1993, 55: 147–154

Bagdassarov N S, Dingwell D B, Wilding M C, Rhyolite magma degassing: An experimental study of melt vesiculation, *Bulletin of Volcanology*, 1996, 57: 587–601

Blower J D, Keating J P, Mader H M, Phillips J C, Inferring volcanic degassing processes from vesicle size distributions, *Geophysical Research Letters*, 2001, 28: 347–350

Blower J D, Keating J P, Mader H.M, Phillips J C, The evolution of bubble size distributions in volcanic eruptions, *Journal of Volcanology and Geothermal Research*, 2003, 120: 1–23

Cashman K V, Mangan M T, Newman S, Surface degassing and modifications to vesicle size distributions in active basalt flows, *Journal of Volcanology and Geothermal Research*, 1994, 61: 45–68

Fink J H, Anderson S W, Manley C R, Textural constraints on effusive silicic volcanism - Beyond the permeable foam model, *Journal of Geophysical Research*, 1992, 97 (B6): 9073–9083

Gaonac'h H, Lovejoy S, Stix J, Schertzer D, A scaling growth model for bubbles in basaltic lava flows, *Earth and Planetary Science Letters*, 1996, 139: 395–409

Gardner J, Hilton M, Carroll M, Experimental constraints on degassing of magma: Isothermal bubble growth during continuous decompression from high pressure, *Earth and Planetary Science Letters*, 1999, 168: 201–218

Giordano D, Dingwell D B, Non-Arrhenian multicomponent melt viscosity: A model, *Earth and Planetary Science Letters*, 2003, 208: 337–349

Giordano D, Nichols A R L, Dingwell D B, Glass transition temperatures of natural hydrous melts: A relationship with shear viscosity and implications for the welding process, *Journal of Volcanology and Geothermal Research*, 2005, 142: 105–118

Gonnermann H M, Manga M, Explosive volcanism may not be an inevitable consequence of magma fragmentation, *Nature*, 2003, 426: 432–435

Herd R, Pinkerton H, Bubble coalescence in basaltic lava: Its impact on the evolution of bubble populations, *Journal of Volcanology and Geothermal Research*, 1997, 75: 137–157

Holloway J R, Blank J G, Application of experimental results to C-O-H species in natural melts, *Reviews in Mineralogy*, 1994, 30: 187– 230

Hurwitz S, Navon O, Bubble nucleation in rhyolitic melts: Experiments at high pressure, temperature, and water content, *Earth and Planetary Science Letters*, 1994, 122: 267–280

Klug C, Cashman K V, Bacon C R, Structure and physical characteristics of pumice from the climatic eruption of Mount Mazama (Crater Lake), Oregon, *Bulletin of Volcanology*, 2002, 64: 486–501

Larsen J F, Gardner J E, Experimental constraints on bubble interactions in rhyolite melts: Implications for vesicle size distributions, *Earth and Planetary Science Letters*, 2000, 180: 201–214

Larsen J F, Denis M H, Gardner J E, Experimental study of bubble coalescence in rhyolitic and phonolitic melts, *Geochimica et Cosmochimica Acta*, 2004, 68: 333–344

Lovejoy S, Gaonac'h, Schertzer D, Bubble distributions and dynamics: The expansion–coalescence equation, *Journal of Geophysical Research*, 2004, 109 (B11203), doi:10.1029/2003JB002823

Lyakhovsky V, Hurwitz S, Navon O, Bubble growth in rhyolitic melts: Experimental and numerical investigation, *Bulletin of Volcanology*, 1996, 58: 19–32

Mader H M, Zhang Y, Phillips J C, Sparks R S J, Sturtevant B, Stolper E, Experimental simulations of explosive degassing magma, *Nature*, 1994, 372: 85–88

Mader H D, Brodsky E E, Howard D, Sturtevant B, Laboratory simulations of sustained volcanic erutpions, *Nature*, 1997, 388: 462–464

Mangan M T, Cashman K V, Newman S, Vesiculation of basaltic magma during eruption, *Geology*, 1993, 21: 157–160

Mangan M T, Cashman K V, The structure of basaltic scoria and reticulite and inferences for vesiculation, foam formation, and fragmentation in lava fountains, *Journal of Volcanology and Geothermal Research*, 1996, 73: 1–18

Mangan M, Mastin L, Sisson T, Gas evolution in eruptive conduits: Combining insights from high temperature and pressure decompression experiments with steady-state flow modeling, *Journal of Volcanology and Geothermal Research*, 2004, 129: 23–36

Martel C, Bureau H, In situ high-pressure and high-temperature bubble growth in silicic melts, *Earth and Planetary Science Letters*, 2001, 191: 115–127

Marti J, Soriano C, Dingwell D B, Tube pumices as strain markers of the ductile-brittle transition during magma fragmentation, *Nature*, 1999, 402: 650–653

Marsh B D, Crystal size distributions (CSD) in rocks and the kinetics and dynamics of crystallization: 1. Theory, *Contributions to Mineralogy and Petrology*, 1988, 99: 277–291

Melnik O E, Volcanology: Fragmenting magma, *Nature*, 1999, 397: 394–395

Mysen B O, Richet P, Silicate glasses and melts: Properties and structure, Elsevier, Amsterdam, 2005, pp: 35–68

Navon O, Chekhmir A, Lyakhovsky V, Bubble growth in highly viscous melts: Theory, experiments, and autoexplosivity of dome lavas, *Earth and Planetary Science Letters*, 1998, 160: 763–776

Papale P, Strain-induced magma fragmentation in explosive eruptions, *Nature*, 1999, 397: 425–428

Papale P, Polacci M, Role of carbon dioxide in the dynamics of magma ascent in explosive eruptions, *Bulletin of Volcanology*, 1999, 60: 583–594

Proussevitch A A, Sahagian D L, Kutolin V A, Stability of foams in silicate melts, *Journal of Volcanology and Geothermal Research*, 1993, 59: 161–178

Proussevitch A A, Sahagian D L, Dynamics of coupled diffusive and decompressive bubble growth in magmatic systems, *Journal of Geophysical Research*, 1996, 101 (B8): 17447–17456

Proussevitch A A, Sahagian D L, Dynamics and energetics of bubble growth in magmas: Analytical formulation and numerical modeling, *Journal of Geophysical Research*, 1998, 103 (B8): 18223–18251

Rasband W S, ImageJ, U. S. National Institutes of Health, Bethesda, Maryland, USA, 1997–2005, http://rsb.info.nih.gov/ij/

Sahagian D L, Proussevitch A A, 3D particle size distributions from 2D observations: Stereology for natural applications, *Journal of Volcanology and Geothermal Research*, 1998, 84: 173–196

Song S R, Jones K W, Lindquist B W, Dowd B A, Sahagian D L, Synchrotron X-ray computed microtomography: Studies on vesiculated basaltic rocks, *Bulletin of Volcanology*, 2001, 63: 252–263

Sparks R S J, The dynamics of bubble formation and growth in magmas: A review and analysis, *Journal of Volcanology and Geothermal Research*, 1978, 3: 1–37

Sparks R S J, Barclay J, Jaupart C, Mader H M, Phillips J C, Physical aspects of magmatic degassing: 1. Experimental and theoretical constraints on vesiculation, *Reviews in Mineralogy*, 1994, 30: 413–443

Stein D J, Spera F J, Rheology and microstructure of magmatic emulsions: Theory and experiments, *Journal of Volcanology and Geothermal Research*, 1992, 49: 157–174

Thomas N, Jaupart C, Vergniolle S, On the vesicularity of pumice, *Journal of Geophysical Research*, 1994, 99 (B8): 15633–15644

Toramaru A, Numerical study of nucleation and growth of bubbles in viscous magma, *Journal of Geophysical Research*, 1995, 100 (B2): 1913–1932

Vergniolle S, Brandeis G, Mareschal J C, Strombolian explosions: Eruption dynamics determined from acoustic measurements, *Journal of Geophysical Research*, 1996, 101 (B9): 20449–20466

Vergniolle S, Boichu M, Caplan-Auerbach J, Acoustic measurements of the 1999 basaltic eruption of Shishaldin volcano, Alaska: 1. Origin of Strombolian activity, *Journal of Volcanology and Geothermal Research*, 2004, 137: 109–134

Wallace P J, Anderson A T Jr., Davis A M, Gradients in $H_2O$, $CO_2$, and exsolved gas in a large-volume silicic magma system: Interpreting the record preserved in melt inclusions from the Bishop Tuff, *Journal of Geophysical Research*, 1999, 104 (B9): 20097–20122

Wilson L, Relationships between pressure, volatile content and ejecta velocity in three types of volcanic eruption, *Journal of Volcanology and Geothermal Research*, 1980, 8: 297–313

Yamada K, Tanaka H, Nakazawa K, Emori H, A new theory of bubble formation in magma, *Journal of Geophysical Research*, 2005, 110 (B02203): 1–17

Zhang Y, A criterion for the fragmentation of bubbly magma based on brittle failure theory, *Nature*, 1999, 402: 648–650

# FIGURES

**Fig. 1.** Schematic illustration of the experimental setup for in-situ degassing on the GSECARS Synchrotron beamline at the Advanced Photon Source (APS), Argonne National Lab, Chicago.

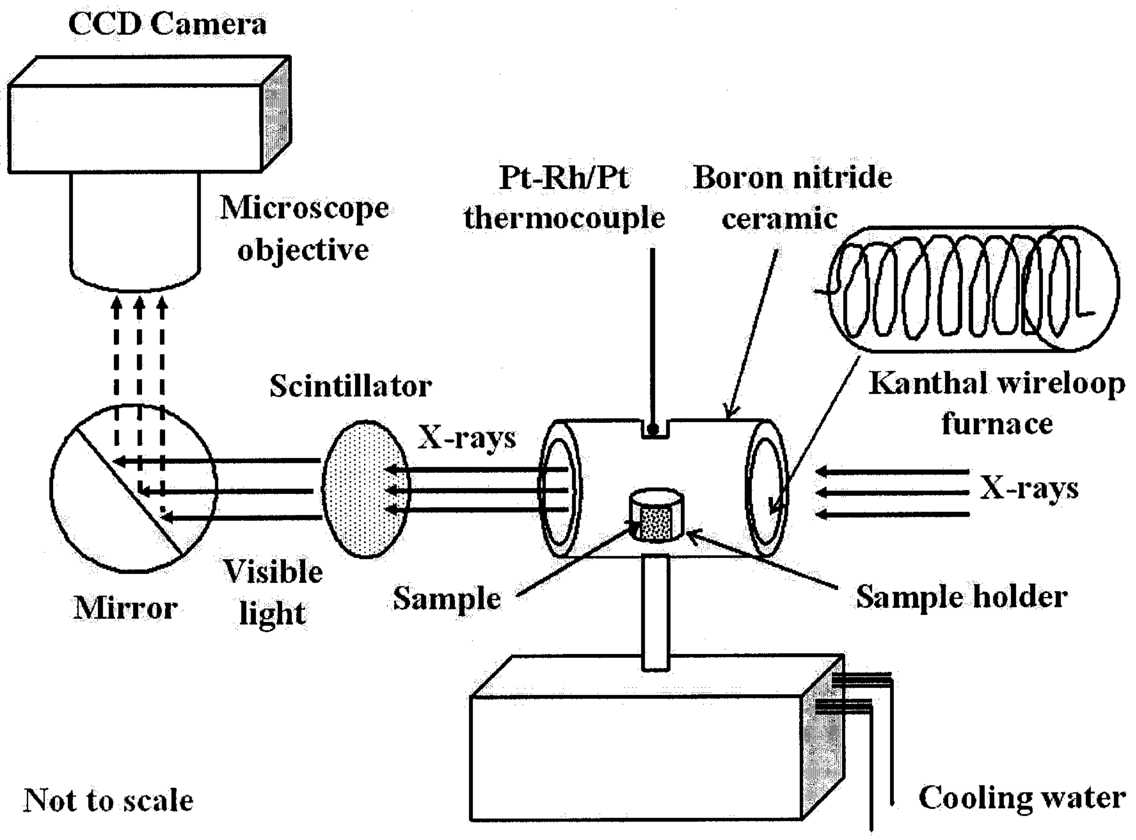

**Fig. 2.** Calibration of the temperatures of the furnace against the temperatures of samples inside the furnace.

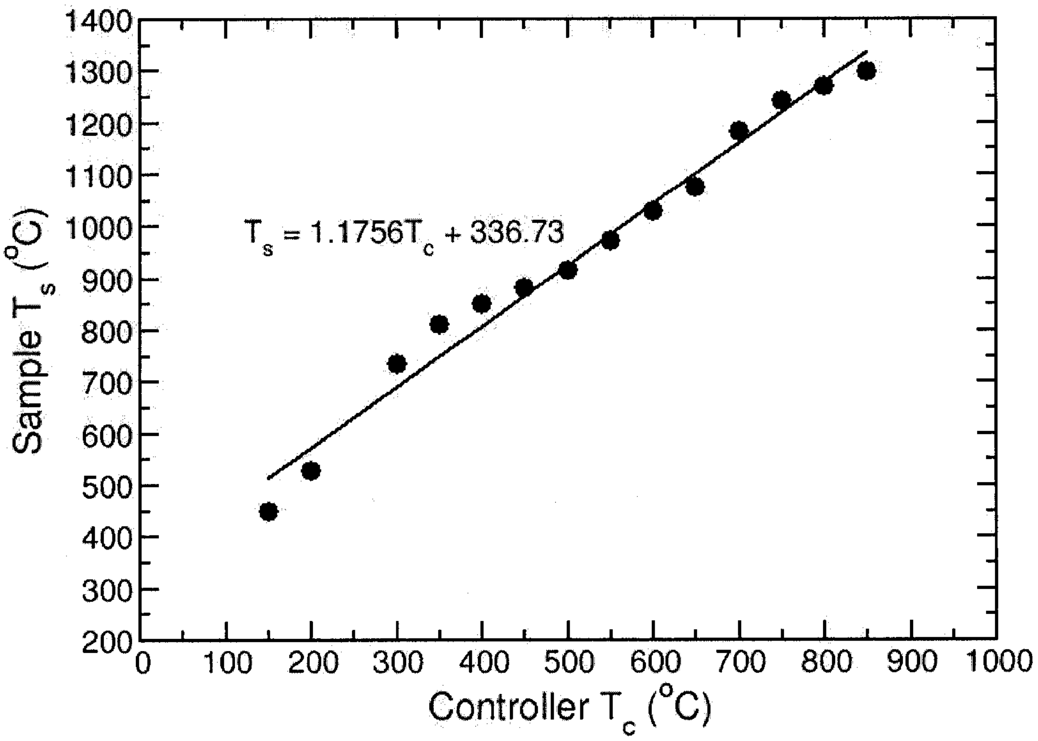

**Fig. 3.** In situ observations of bubble growth in sample St84c initially containing 6.24 wt% $H_2O$ and 822 ppm $CO_2$. The time sequence is t = 0, 427, 1290, 1490 s. The initial glass is about 3.0 mm in diameter and 2.5 mm in thickness. The glass in the furnace begins to expand after it is heated for 427 s, then it remains approximately constant in shape. The glass begins to shrink from 1030 to 1140 s and then expands again due to bubble growth. Bubbles begin to pop rapidly after 1490 s.

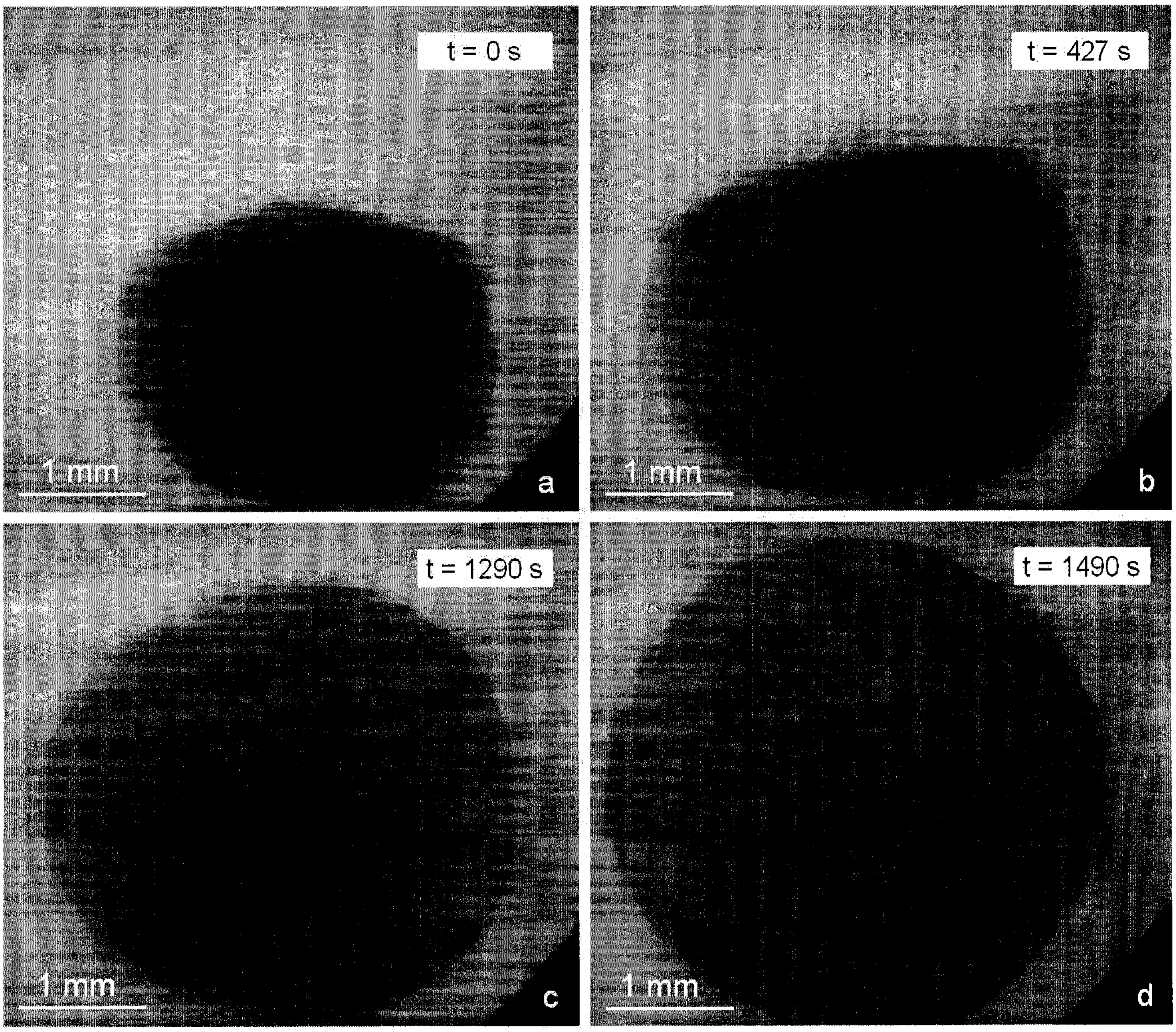

**Fig. 4.** Log – log plots of the bubble size distributions measured from X-ray microtomography for samples St84ab, c, d, e containing 6.24 wt% $H_2O$ and 822 ppm $CO_2$. The bars are the distributions of bubble sizes indicated by log V ~ log N, the open circles and the line fit to them are the bubble size distribution indicated by log (N>V) ~ log V. V: bubble volume; N: bubble number; $\phi$: vesicularity; c: correlation coefficient.

**a** At a vesicularity of 2.9%, the bubble size distribution follows a power-law relation, showing a narrow bubble size distribution. Small bubbles are dominant. **b** At a vesicularity of 25.6%, the bubble size distribution shifts to larger sizes, showing bubble growth and coalescence. A peak corresponding to bubble volumes of ~ 1000 $\mu m^3$ appears, implying the occurrence of multiple nucleation events. **c** At a vesicularity of 72%, bubble size distributions tend to evolve to an exponential relation. Bubble numbers per unit volume decrease significantly, and a foam is formed due to coalescence. **d** At a vesicularity of 82.3%, the bubble size distribution shows an evolution to an exponential relation, and the bubble size has a broad distribution. **e** Natural sample with a vesicularity of 72%, showing a power-law bubble size distribution with an exponent of 1.0.

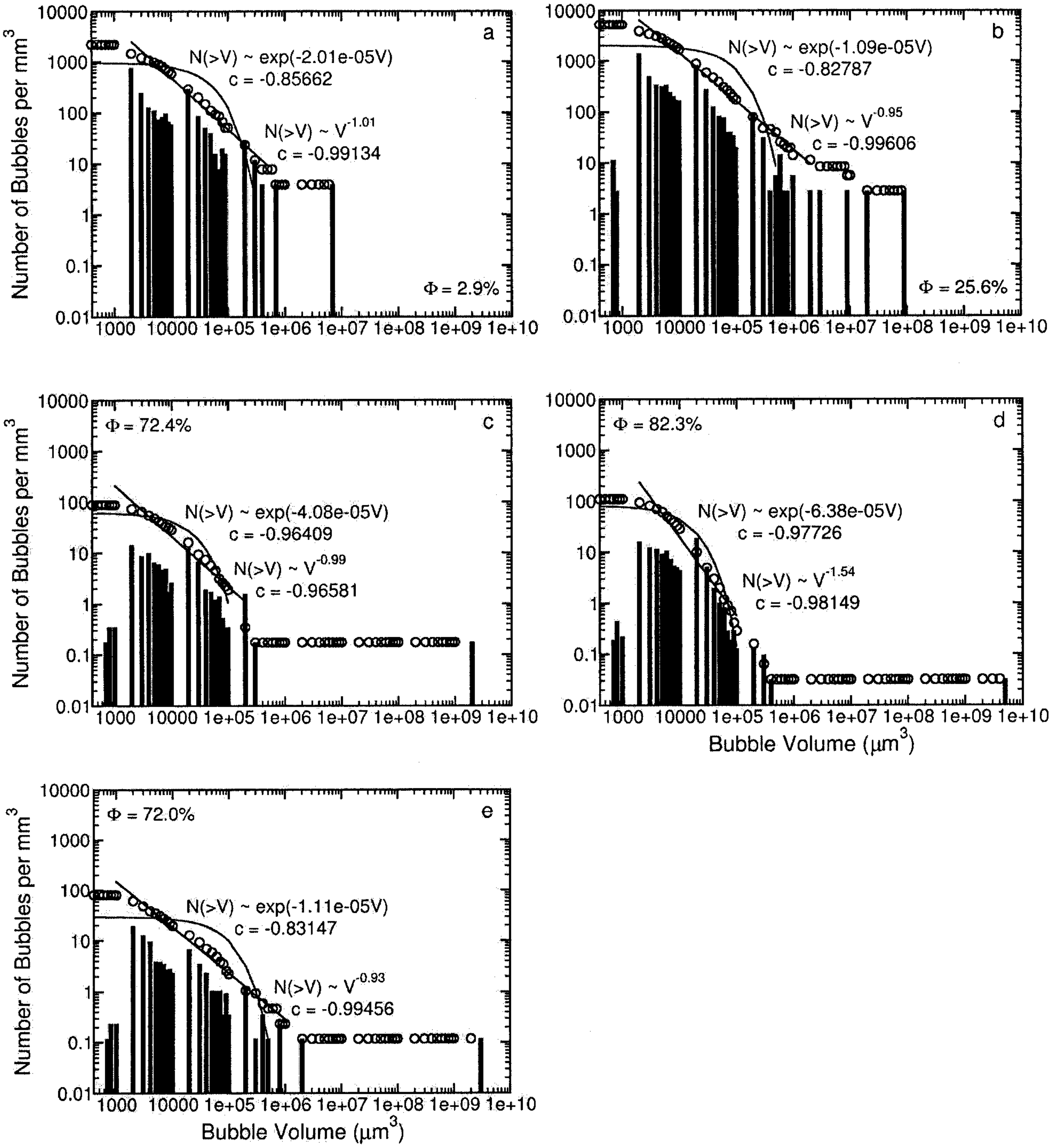
Number of Bubbles per mm$^3$
Bubble Volume (μm$^3$)
10000
1000
100
10
1
0.1
0.01
1000
10000
1e+05
1e+06
1e+07
1e+08
1e+09
1e+10
a
N(>V) ~ exp(-2.01e-05V)
c = -0.85662
N(>V) ~ V$^{-1.01}$
c = -0.99134
Φ = 2.9%
b
N(>V) ~ exp(-1.09e-05V)
c = -0.82787
N(>V) ~ V$^{-0.95}$
c = -0.99606
Φ = 25.6%
c
Φ = 72.4%
N(>V) ~ exp(-4.08e-05V)
c = -0.96409
N(>V) ~ V$^{-0.99}$
c = -0.96581
d
Φ = 82.3%
N(>V) ~ exp(-6.38e-05V)
c = -0.97726
N(>V) ~ V$^{-1.54}$
c = -0.98149
e
Φ = 72.0%
N(>V) ~ exp(-1.11e-05V)
c = -0.83147
N(>V) ~ V$^{-0.93}$
c = -0.99456

**Fig. 5.** Log – log plots of bubble size distributions measured from X-ray microtomography for samples St58a, b, d containing 2.91 wt% $H_2O$ and samples St65a, b, c containing 7.17 wt% $H_2O$ and 1478 ppm $CO_2$. **a** to **c** correspond to samples St58a, St58b, St58d, **d** to **f** correspond to samples St65a, St65b, St65c. The bars are the distribution of bubble sizes indicated by log V ~ log N, the open circles and the line fit to them are the bubble size distributions indicated by log (N>V) ~ log V. V: bubble volume; N: bubble number; $\phi$: vesicularity; c: correlation coefficient.

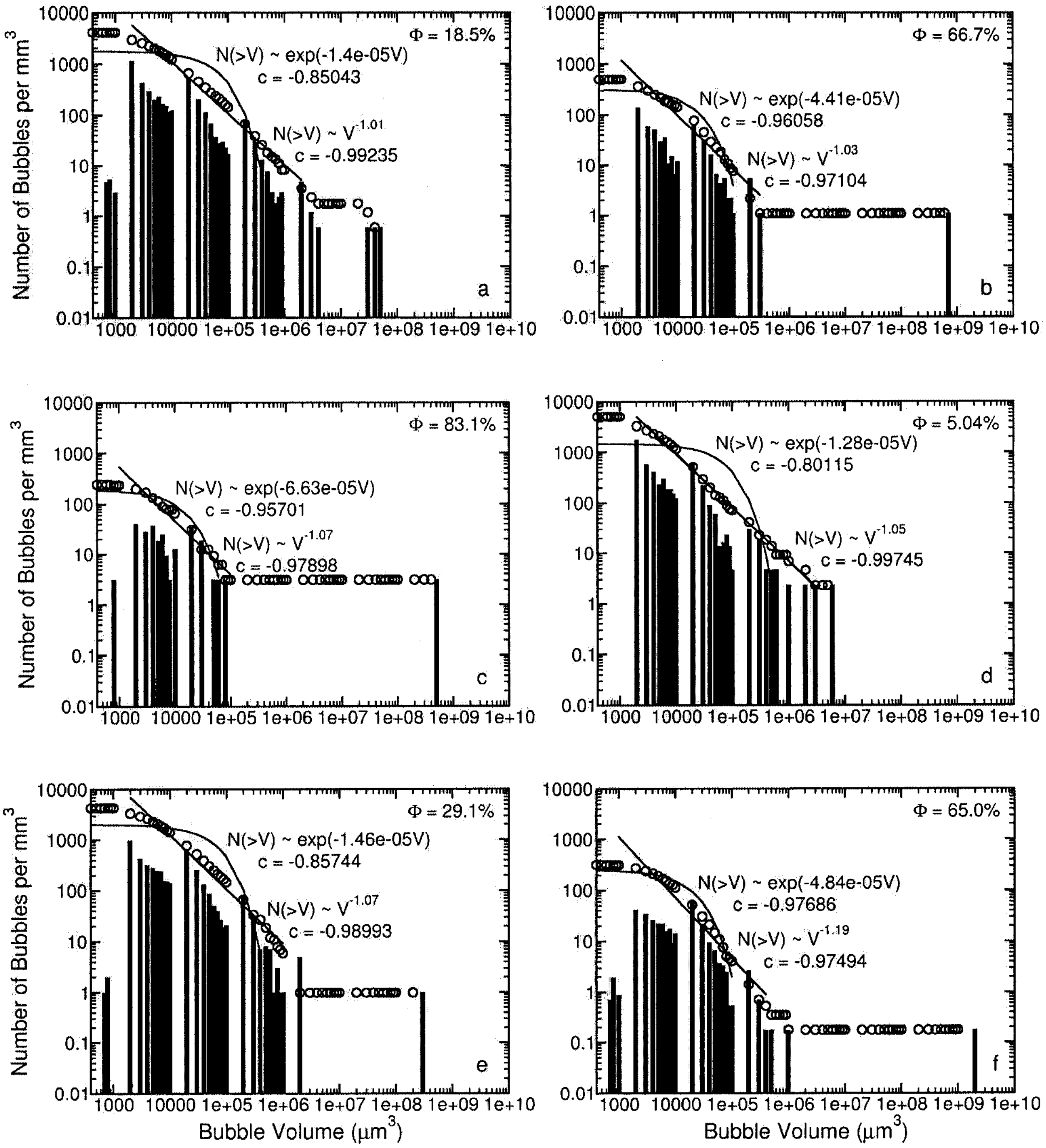
Number of Bubbles per mm$^3$
Bubble Volume (μm$^3$)
10000
1000
100
10
1
0.1
0.01
1000 10000 1e+05 1e+06 1e+07 1e+08 1e+09 1e+10
Φ = 18.5%
N(>V) ~ exp(-1.4e-05V)
c = -0.85043
N(>V) ~ V$^{-1.01}$
c = -0.99235
a
Φ = 66.7%
N(>V) ~ exp(-4.41e-05V)
c = -0.96058
N(>V) ~ V$^{-1.03}$
c = -0.97104
b
Φ = 83.1%
N(>V) ~ exp(-6.63e-05V)
c = -0.95701
N(>V) ~ V$^{-1.07}$
c = -0.97898
c
Φ = 5.04%
N(>V) ~ exp(-1.28e-05V)
c = -0.80115
N(>V) ~ V$^{-1.05}$
c = -0.99745
d
Φ = 29.1%
N(>V) ~ exp(-1.46e-05V)
c = -0.85744
N(>V) ~ V$^{-1.07}$
c = -0.98993
e
Φ = 65.0%
N(>V) ~ exp(-4.84e-05V)
c = -0.97686
N(>V) ~ V$^{-1.19}$
c = -0.97494
f

**Fig. 6.** Log – log plots of the bubble size distributions measured from X-ray microtomography for high pressure degassing samples St69, St42, and St25 and the images of 2D slices from each of these samples, showing that the bubble size distributions follow exponential relations. The 2D slice pictured is 1442.3 x 1351.8 microns. $\phi$: vesicularity.

**a** Sample St69 containing 5.6 wt% $H_2O$ degassed by a decrease in pressure from 1000 MPa to 370 MPa. The bubble growth time is 21 s. **b** Sample St42 containing 5.3 wt% $H_2O$ and 877 ppm $CO_2$ degassed by a decrease in pressure from 1000 MPa to 370 MPa. The bubble growth time is 360 s. **c** Sample St25 containing 7.5 wt% $H_2O$ degassed by a decrease in pressure from 1000 MPa to 250 MPa. The bubble growth time is 15 s.

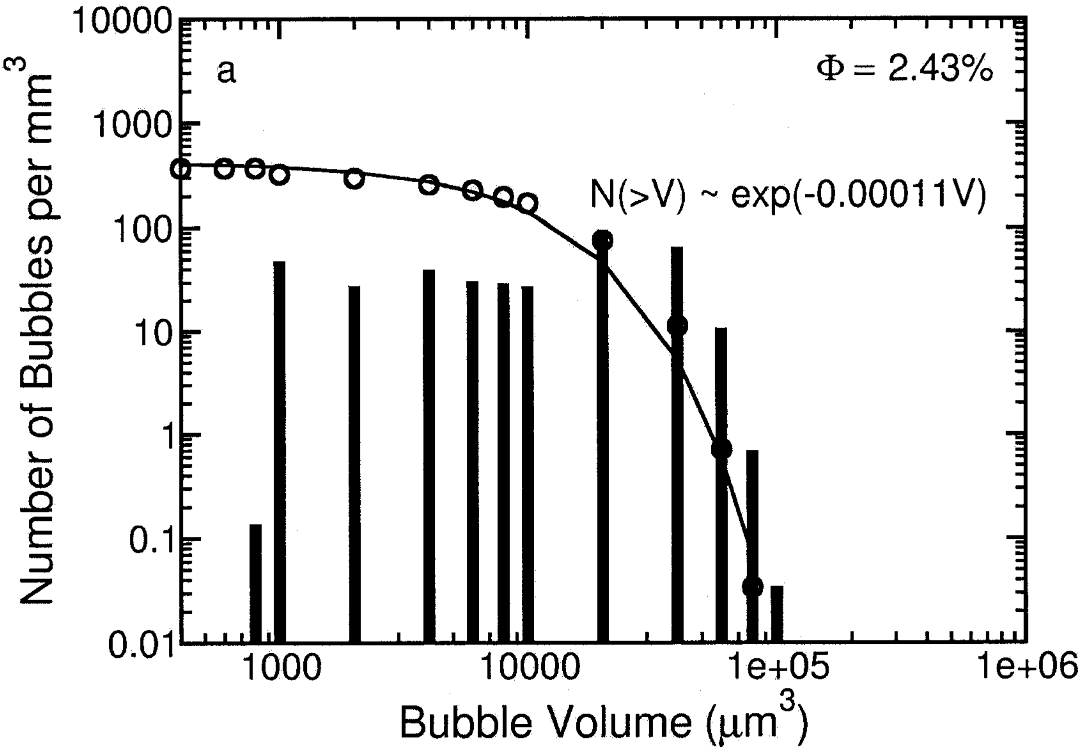

a
Φ = 2.43%
N(>V) ~ exp(-0.00011V)
Number of Bubbles per mm$^3$
10000
1000
100
10
1
0.1
0.01
1000
10000
1e+05
1e+06
Bubble Volume (μm$^3$)

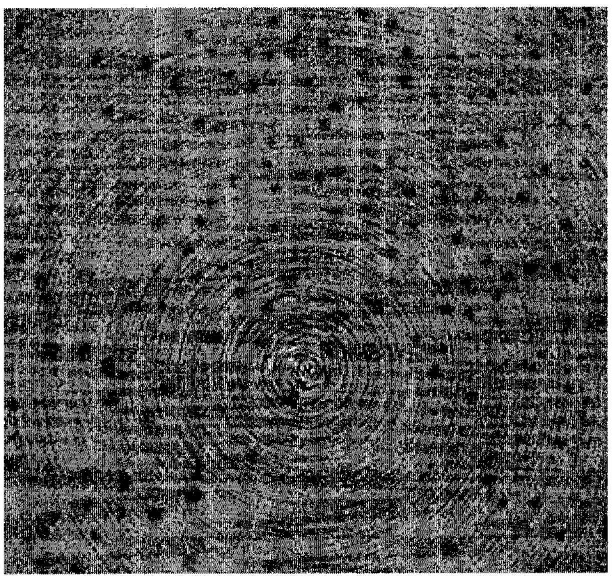

**a**

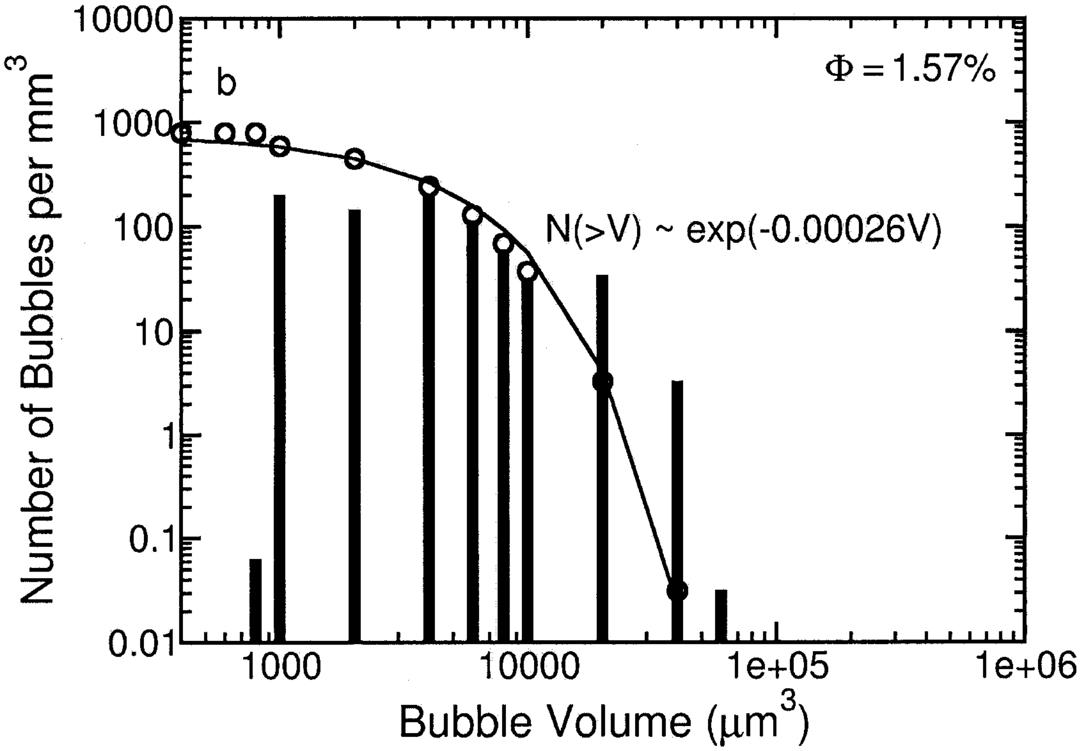
b
Φ = 1.57%
N(>V) ~ exp(-0.00026V)
Number of Bubbles per mm$^3$
10000
1000
100
10
1
0.1
0.01
1000
10000
1e+05
1e+06
Bubble Volume (μm$^3$)

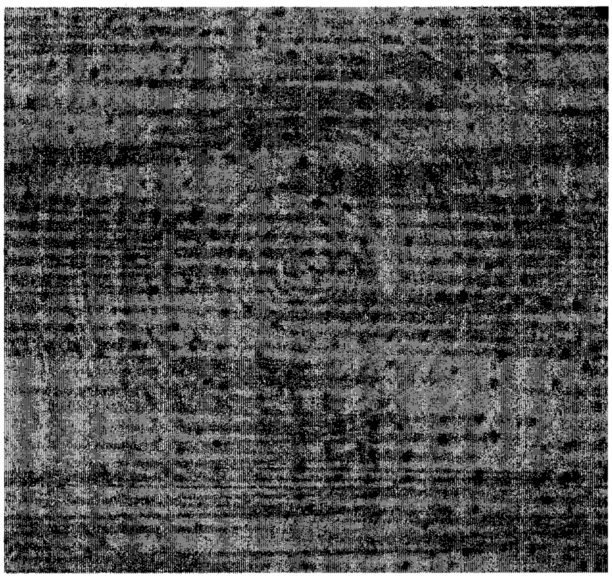

b

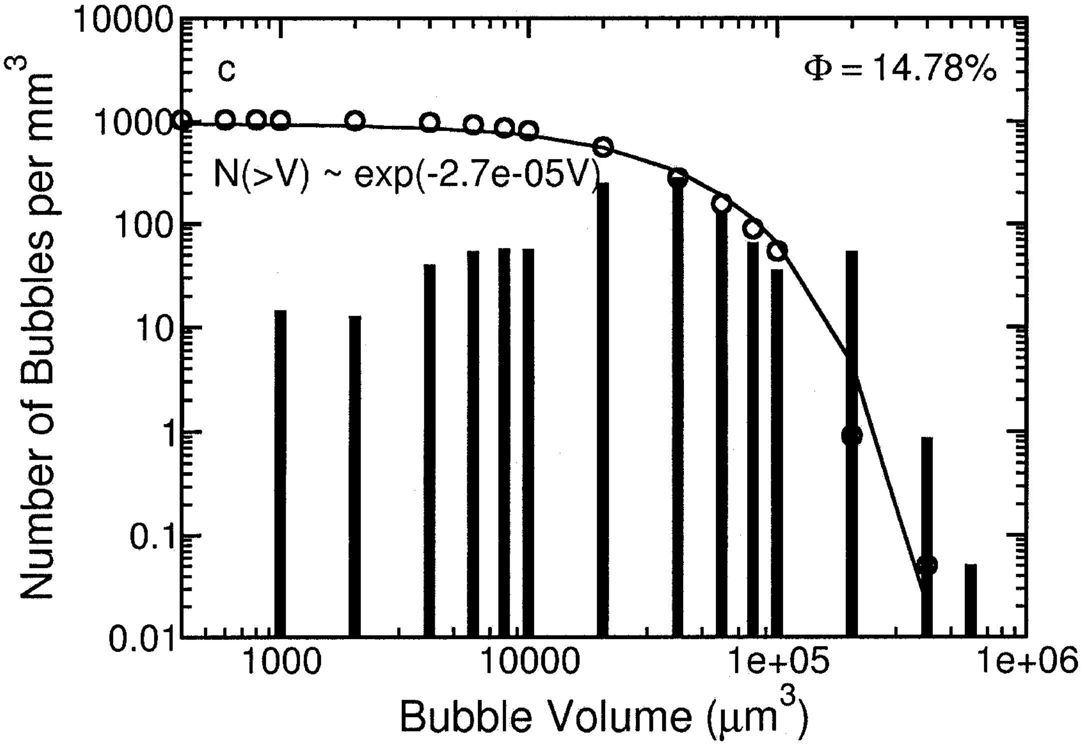
c
Φ = 14.78%
N(>V) ~ exp(-2.7e-05V)
Number of Bubbles per mm$^3$
10000
1000
100
10
1
0.1
0.01
1000
10000
1e+05
1e+06
Bubble Volume (μm$^3$)

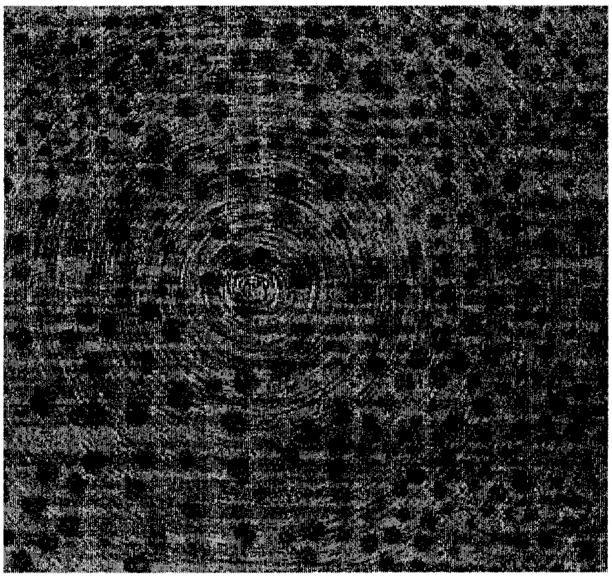

**c**

**Fig. 7.** Bubble foam structure of Stromboli basalt initially containing 6.24 wt% $H_2O$ and 822 ppm $CO_2$ and the natural Stromboli basalt sample.

**a** St84d, quenched at 1166 °C. Most bubbles are not connected, bubbles are not spherical, and bubble size varies significantly. **b** St84e, quenched at 1189 °C. Bubbles are connected to form a non-spherical foam, the bubble size varies significantly. **c** St84ab, quenched at about 1207 °C. The spherical foam is formed, but bubbles in the foam vary significantly in size. **d** St84c, quenched at 1221 °C. The spherical foam consists of bubbles similar in size. **e** Natural sample.

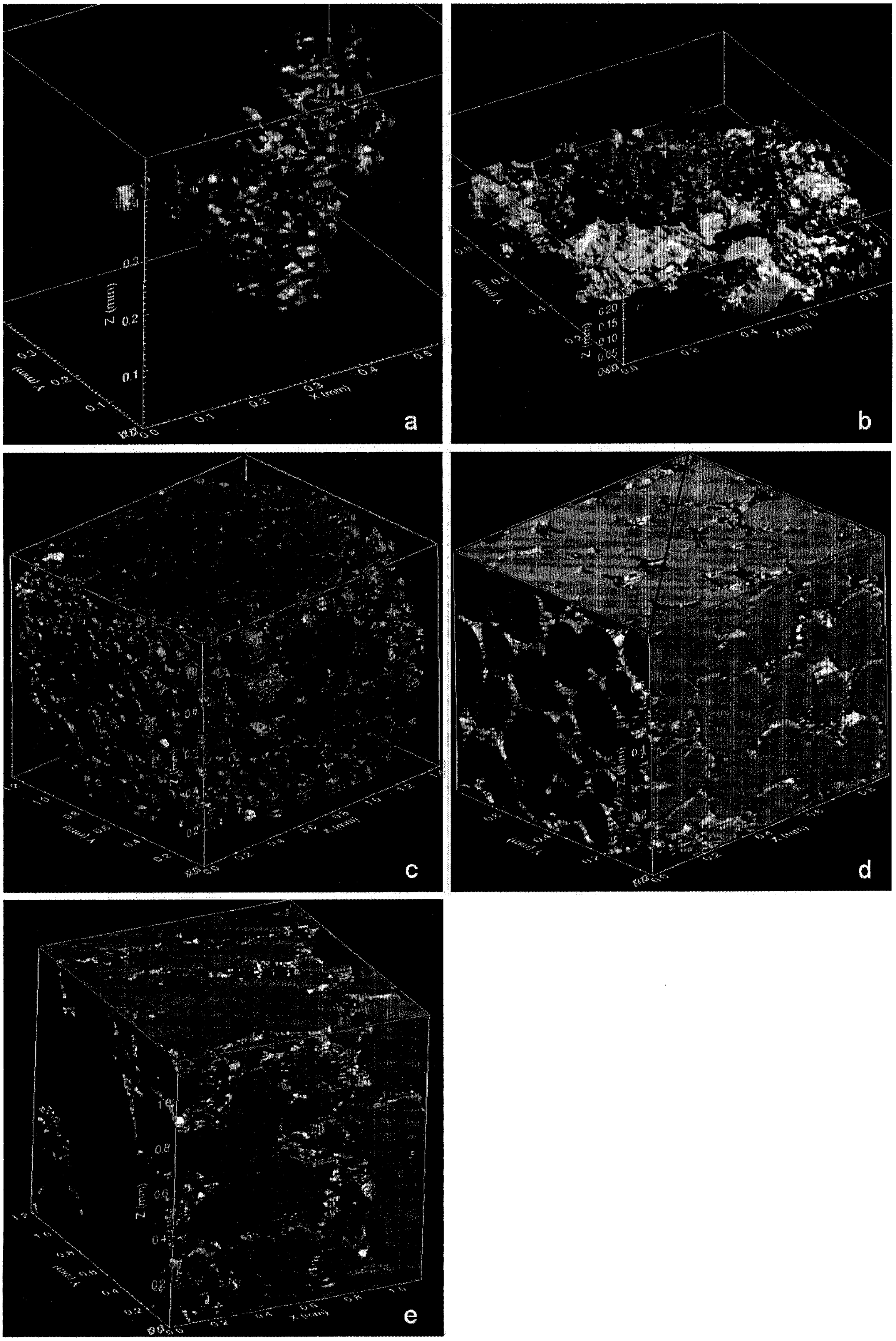
Z (mm)
Y (mm)
X (mm)
a
Z (mm)
Y (mm)
X (mm)
b
Z (mm)
Y (mm)
X (mm)
c
Z (mm)
Y (mm)
X (mm)
d
Z (mm)
Y (mm)
X (mm)
e

**Fig. 8.** Tomographic images of 2D section and 3D bubble structure in Stromboli basalt glass of St7a initially containing 7.3 wt% $H_2O$. **a** Images of 2D slices, showing that bubbles are homogenously distributed in the melt. The 2D slice pictured is 1270.7 × 1309.1 microns. **b** 3D bubble structure, showing that the coalescence of bubbles.

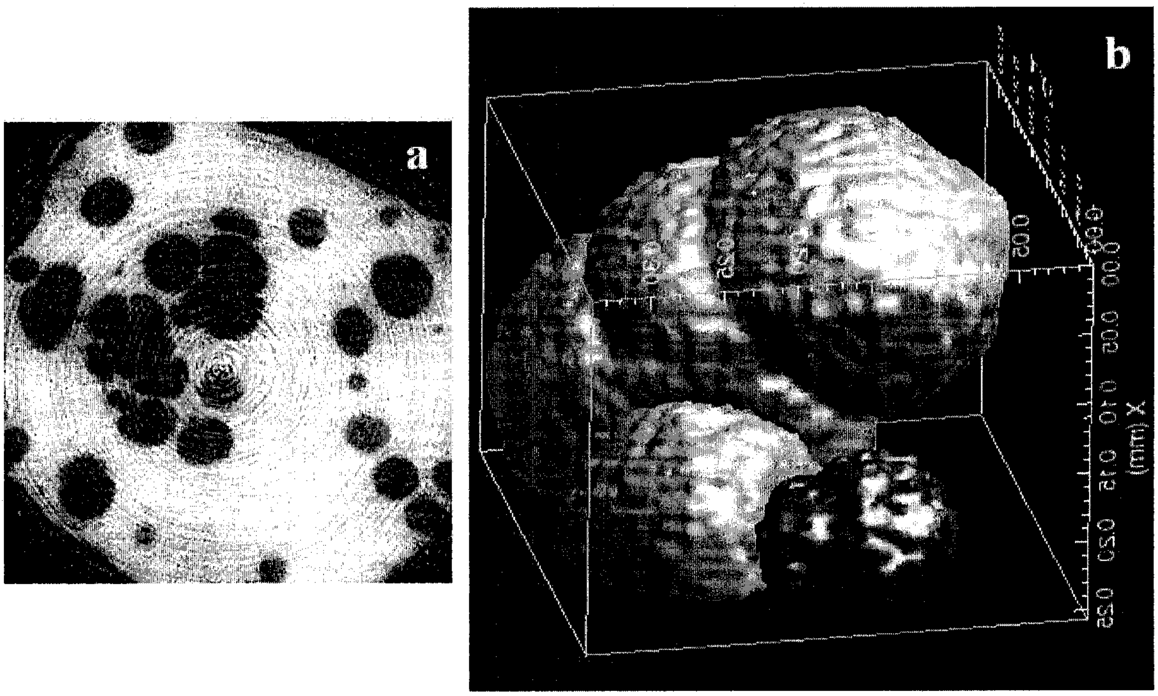

# APPENDIX I: RUN TABLES

**Table 1**. Degassing experiments at 1 atm

| Run | Volatile concentration | $\phi$ (%) | T ($^0$C) | Distribution type | Power law exponent |
|---|---|---|---|---|---|
| St58c | 2.91% $H_2O$ | No bubbles | 701 | — | — |
| St58b | 2.91% $H_2O$ | 18.5 | 1101 | Power law | 1.01 |
| St58a | 2.91% $H_2O$ | 66.7 | 1160 | Exponential | — |
| St58d | 2.91% $H_2O$ | 83.10 | 1218 | Exponential | — |
| St53b | 4.68 % $H_2O$ | No bubbles | 1101 | — | — |
| St53c | 4.68 % $H_2O$ | 3.20 | 1130 | Power law | 0.98 |
| St53a | 4.68 % $H_2O$ | 75.86 | 1230 | Power law | 0.88 |
| St64a | 7.05 % $H_2O$ | 5.63 | 1167 | Power law | 0.94 |
| St64b | 7.05 % $H_2O$ | 64.5 | 1224 | Exponential | — |
| St83d | 6.93 % $H_2O$ | 3.8 | 930 | Power law | 1.41 |
| St83a | 6.93 % $H_2O$ | 7.1 | 975 | Power law | 1.08 |
| St83c | 6.93 % $H_2O$ | 14.0 | 1071 | Power law | 0.96 |
| St83b | 6.93 % $H_2O$ | 16.3 | 1218 | Power law | 1.0 |
| St7b | 7.32 % $H_2O$ | 22.75 | 925 | — | — |
| St7a | 7.32 % $H_2O$ | 31.05 | 1043 | Power law | 0.92 |
| St7c | 7.32 % $H_2O$ | 72.30 | 1160 | Exponential | — |
| St59b | 3.29% $H_2O$, 440 ppm $CO_2$ | No bubbles | 836 | — | — |
| St59c | 3.29% $H_2O$, 440 ppm $CO_2$ | No bubbles | 1130 | — | — |
| St59d | 3.29% $H_2O$, 440 ppm $CO_2$ | 1.01 | 1202 | Power law | 1.18 |
| St59a | 3.29% $H_2O$, 440 ppm $CO_2$ | 82.57 | 1267 | Power law | 0.96 |
| St66c | 5.55 % $H_2O$, 874 ppm $CO_2$ | 1.85 | 761 | Power law | 0.98 |
| St66a | 5.55 % $H_2O$, 874 ppm $CO_2$ | 23.66 | 1218 | Power law | 1.08 |
| St66b | 5.55 % $H_2O$, 874 ppm $CO_2$ | 46.3 | 1245 | Power law | 0.87 |
| St84d | 6.24 % $H_2O$, 822 ppm $CO_2$ | 2.9 | 1165 | Power law | 1.01 |
| St84e | 6.24 % $H_2O$, 822 ppm $CO_2$ | 25.6 | 1189 | Power law | 0.95 |
| St84ab | 6.24 % $H_2O$, 822 ppm $CO_2$ | 72.4 | 1206 | Exponential | — |
| St84c | 6.24 % $H_2O$, 822 ppm $CO_2$ | 82.3 | 1221 | Exponential | — |
| St65c | 7.17 % $H_2O$, 1478 ppm $CO_2$ | 5.04 | 1260 | Power law | 1.05 |

| | | | | | |
|---|---|---|---|---|---|
| St65b | 7.17 % $H_2O$, 1478 ppm $CO_2$ | 29.1 | 1289 | Power law | 1.07 |
| St65a | 7.17 % $H_2O$, 1478 ppm $CO_2$ | 65.0 | 1321 | Exponential | — |

The composition of the Stromboli basalt used in this study is $SiO_2$: 50.8; $TiO_2$: 0.94; $Al_2O_3$: 18.5; $FeO^{total}$: 6.38; MnO: 0.15; MgO: 6.35; CaO: 12.20; $Na_2O$: 2.43; $K_2O$: 1.89; $P_2O_5$: 0.38; Total: 100.02.

The glasses were synthesized at 1000 MPa and 1250 °C and hydrated for 1 hour except for St7 (a – c) which were hydrated for 2 hours.

**Table 2**. Degassing experiments at high pressures

| **Run** | **Volatile concentration** | **Degassing pressure (MPa)** | **Decompression rate (MPa/min)** | **Bubble growth time (s)** | **Vesicularity (%)** |
|---|---|---|---|---|---|
| St69 | 5.6% $H_2O$ | 370 | 82 | 21 | 2.43 |
| St42 | 5.3% $H_2O$,<br>877 ppm $CO_2$ | 370 | 88 | 360 | 1.57 |
| St25 | 7.5% $H_2O$ | 250 | 90 | 15 | 14.78 |

The hydration pressure was 1000 MPa, the hydration temperature was 1250 °C, and the hydration time was 1 hour. All bubble size distributions were best fit with exponential functions.

# APPENDIX II:

# BUBBLE SIZE DISTRIBUTIONS IN 1 ATM EXPERIMENTS

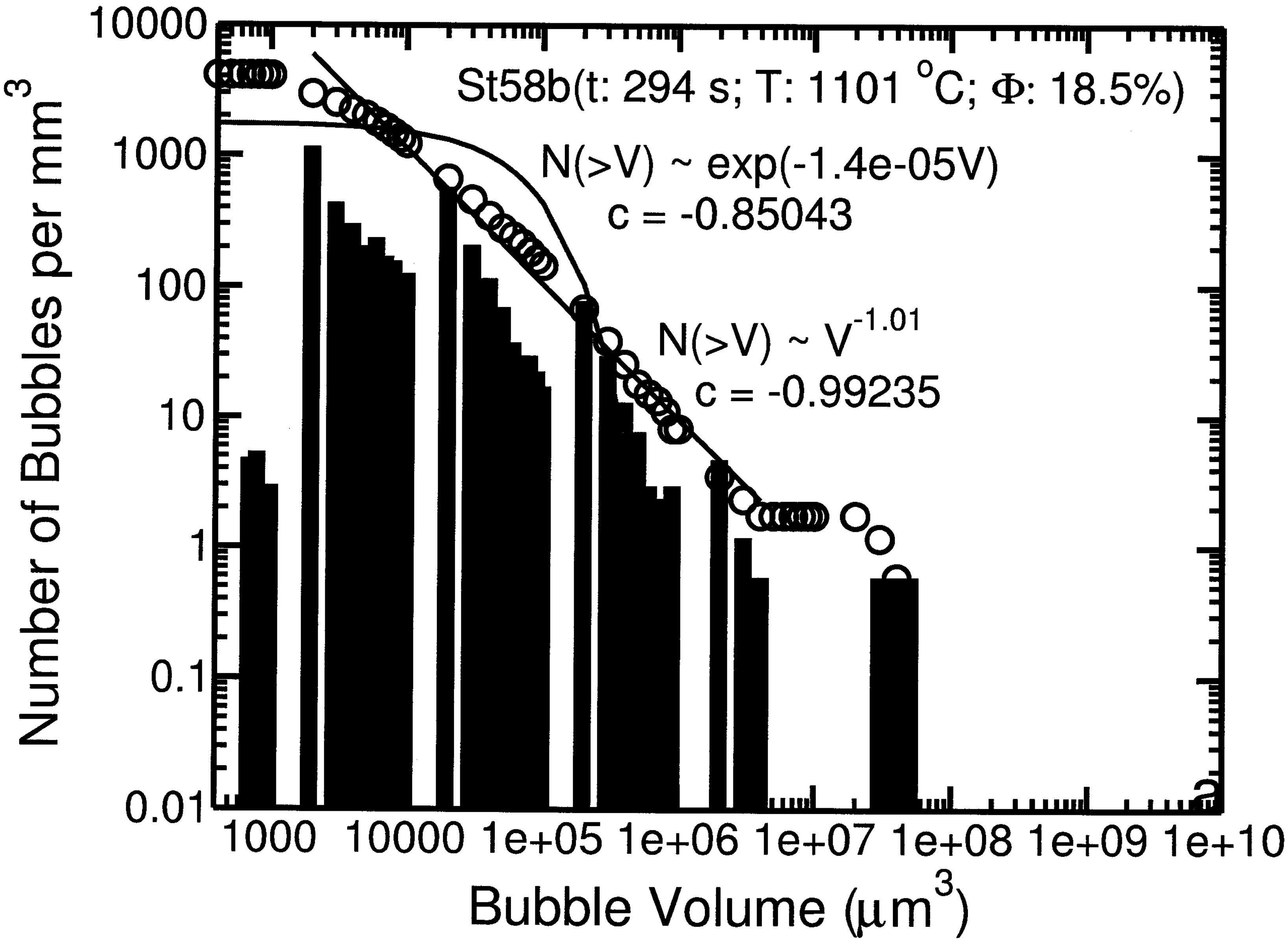
St58b(t: 294 s; T: 1101 °C; Φ: 18.5%)
N(>V) ~ exp(-1.4e-05V)
c = -0.85043
N(>V) ~ V^-1.01
c = -0.99235
Number of Bubbles per mm^3
10000
1000
100
10
1
0.1
0.01
1000
10000
1e+05
1e+06
1e+07
1e+08
1e+09
1e+10
Bubble Volume (μm^3)

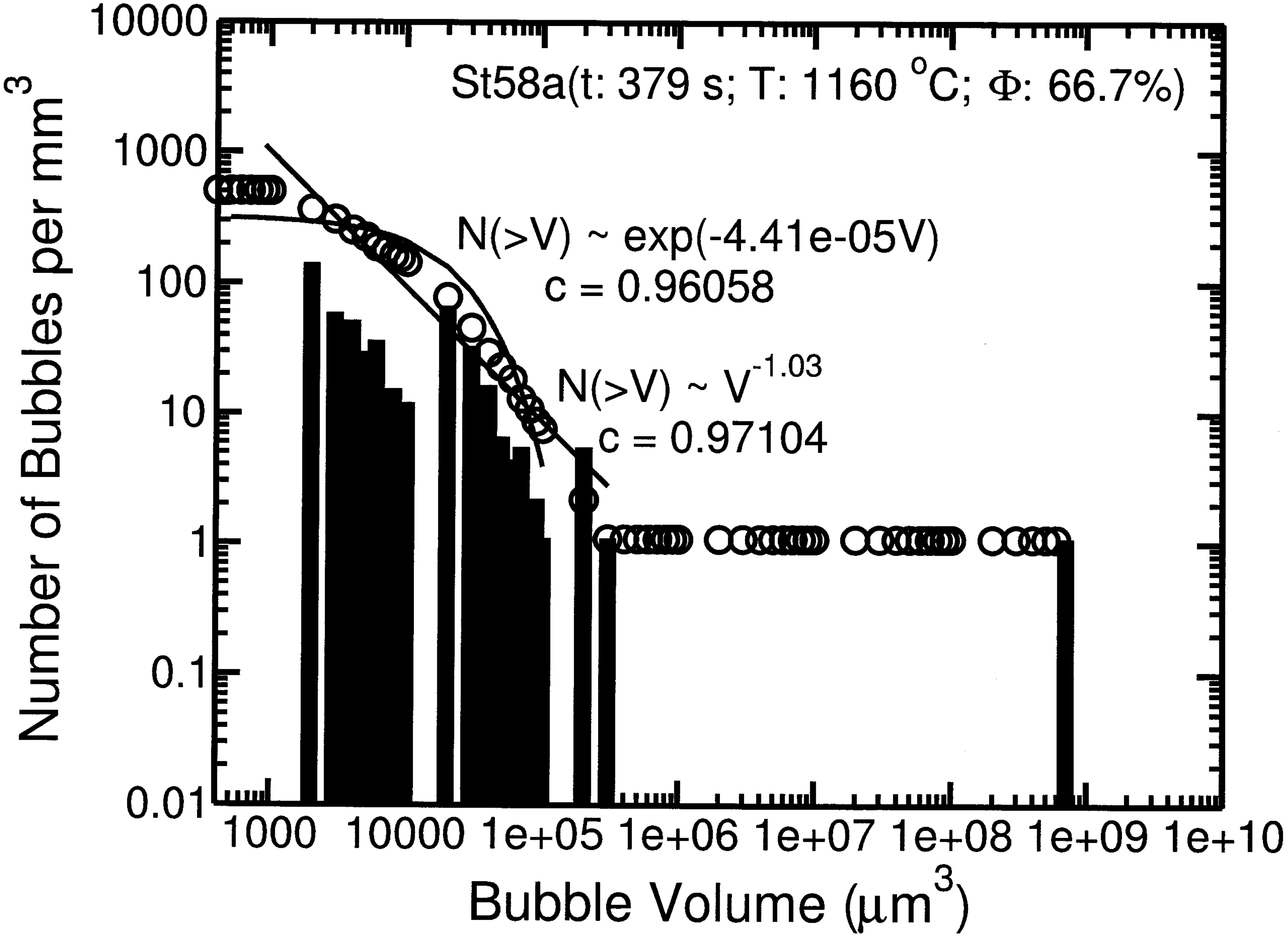
St58a(t: 379 s; T: 1160 °C; Φ: 66.7%)
N(>V) ~ exp(-4.41e-05V)
c = 0.96058
N(>V) ~ V^-1.03
c = 0.97104
Number of Bubbles per mm^3
10000
1000
100
10
1
0.1
0.01
1000
10000
1e+05
1e+06
1e+07
1e+08
1e+09
1e+10
Bubble Volume (μm^3)

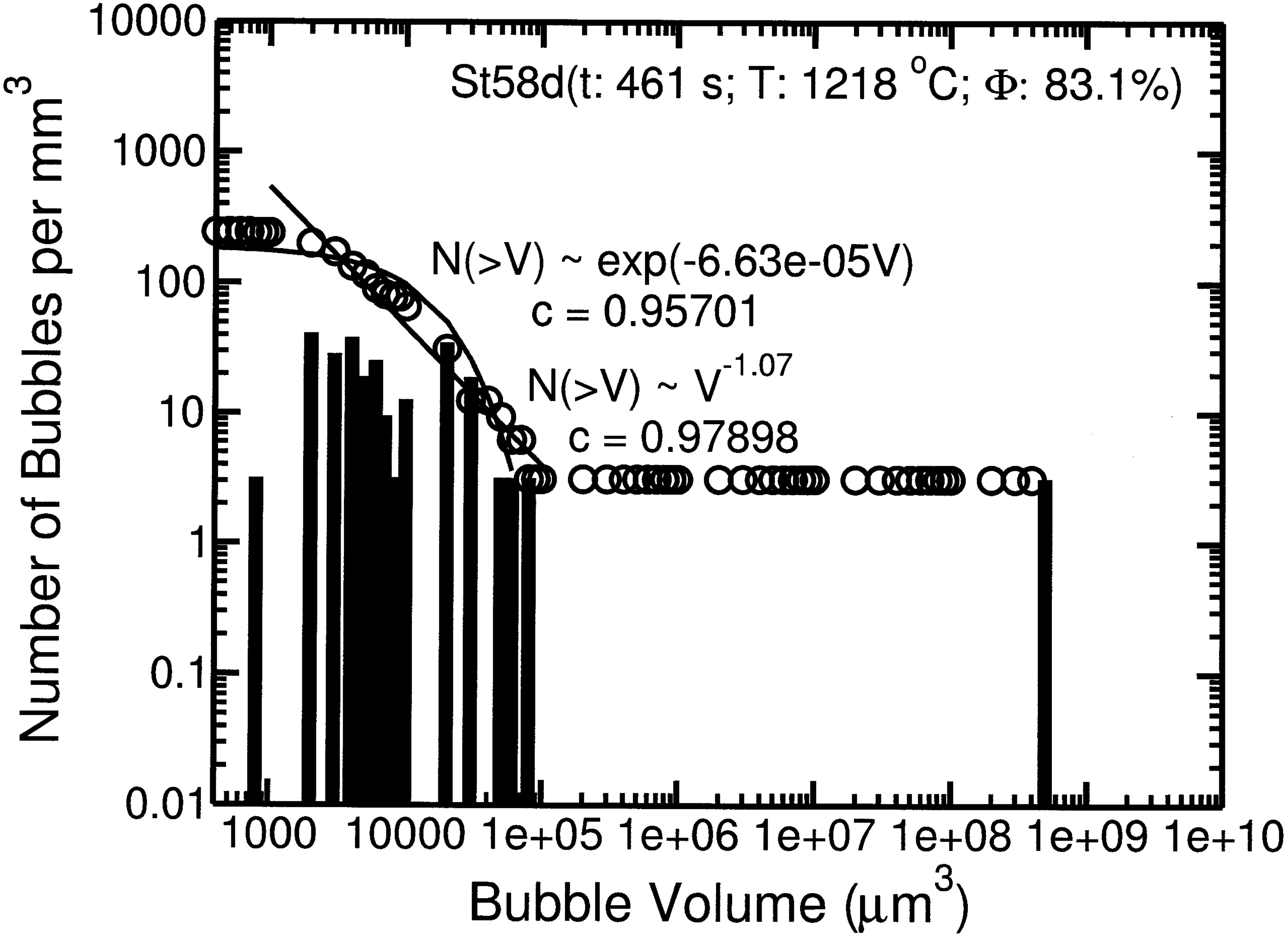
St58d(t: 461 s; T: 1218 °C; Φ: 83.1%)
N(>V) ~ exp(-6.63e-05V)
c = 0.95701
N(>V) ~ V^-1.07
c = 0.97898
Number of Bubbles per mm^3
10000
1000
100
10
1
0.1
0.01
1000
10000
1e+05
1e+06
1e+07
1e+08
1e+09
1e+10
Bubble Volume (μm^3)

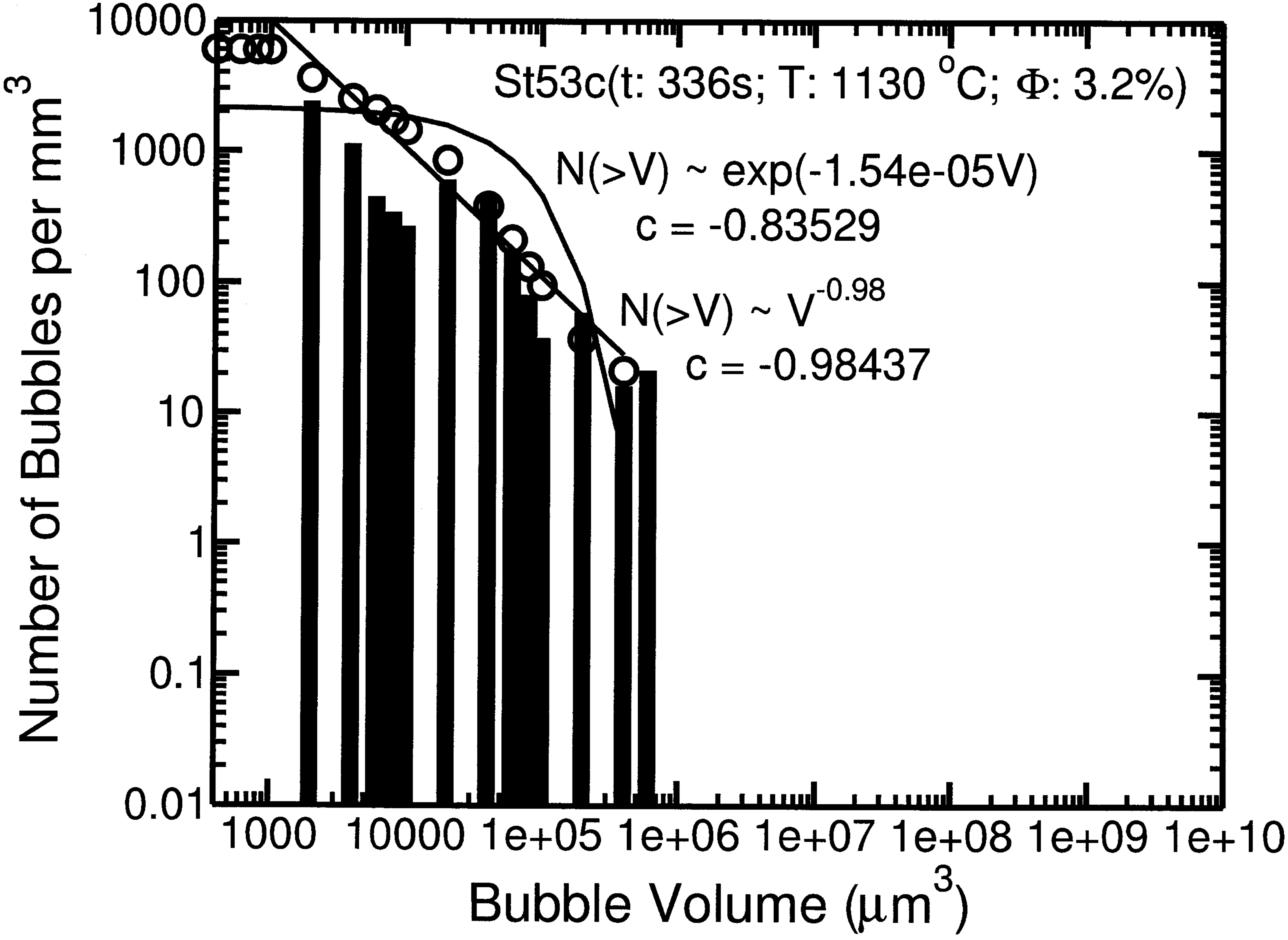
St53c(t: 336s; T: 1130 °C; Φ: 3.2%)
N(>V) ~ exp(-1.54e-05V)
c = -0.83529
N(>V) ~ V^-0.98
c = -0.98437
Number of Bubbles per mm^3
10000
1000
100
10
1
0.1
0.01
1000
10000
1e+05
1e+06
1e+07
1e+08
1e+09
1e+10
Bubble Volume (μm^3)

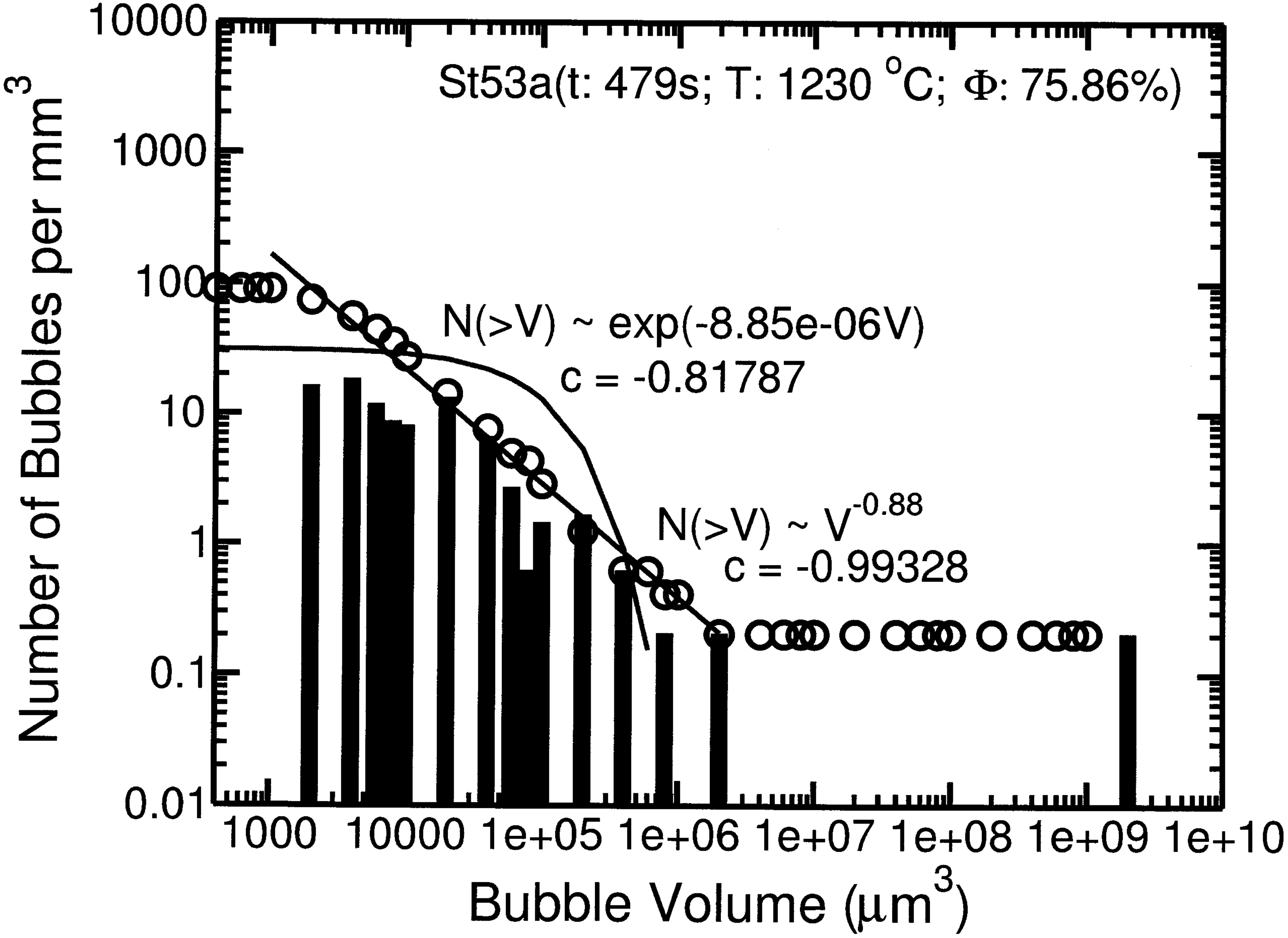
St53a(t: 479s; T: 1230 °C; Φ: 75.86%)
N(>V) ~ exp(-8.85e-06V)
c = -0.81787
N(>V) ~ V^-0.88
c = -0.99328
Number of Bubbles per mm^3
Bubble Volume (μm^3)
10000
1000
100
10
1
0.1
0.01
1000
10000
1e+05
1e+06
1e+07
1e+08
1e+09
1e+10

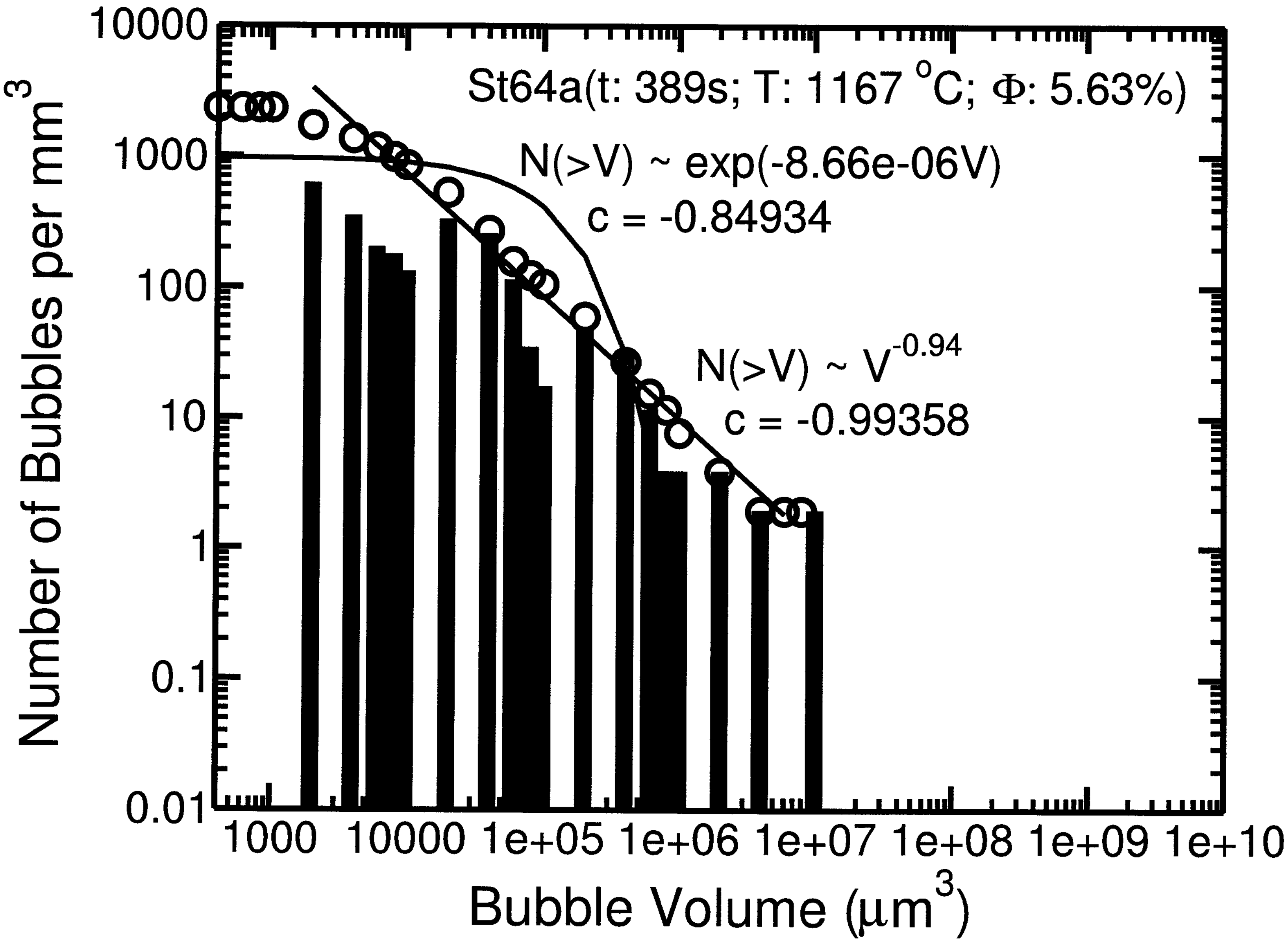
St64a(t: 389s; T: 1167 °C; Φ: 5.63%)
N(>V) ~ exp(-8.66e-06V)
c = -0.84934
N(>V) ~ V^-0.94
c = -0.99358
Number of Bubbles per mm³
10000
1000
100
10
1
0.1
0.01
1000
10000
1e+05
1e+06
1e+07
1e+08
1e+09
1e+10
Bubble Volume (μm³)

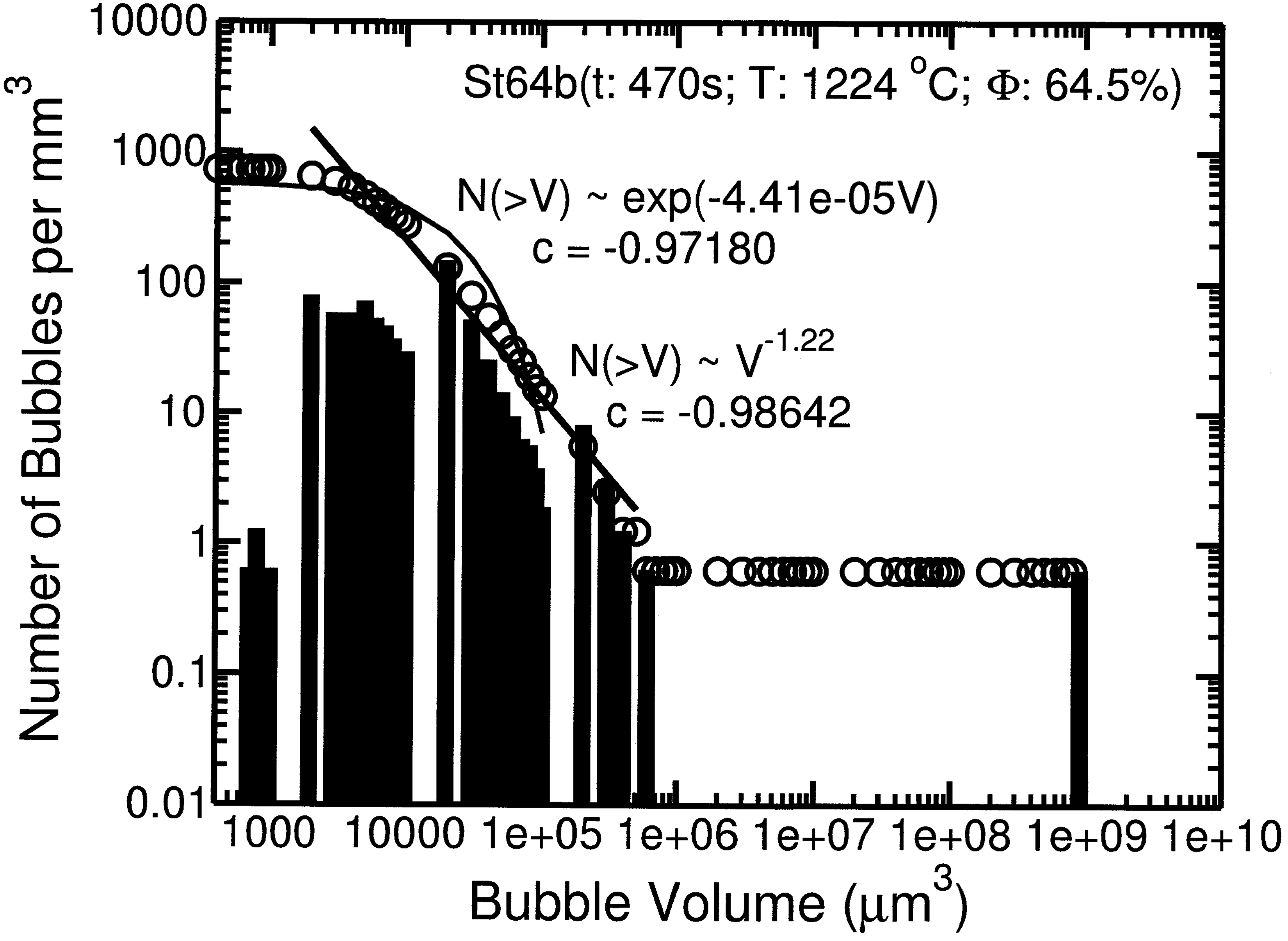
St64b(t: 470s; T: 1224 °C; Φ: 64.5%)
N(>V) ~ exp(-4.41e-05V)
c = -0.97180
N(>V) ~ V^-1.22
c = -0.98642
Number of Bubbles per mm^3
10000
1000
100
10
1
0.1
0.01
1000
10000
1e+05
1e+06
1e+07
1e+08
1e+09
1e+10
Bubble Volume (μm^3)

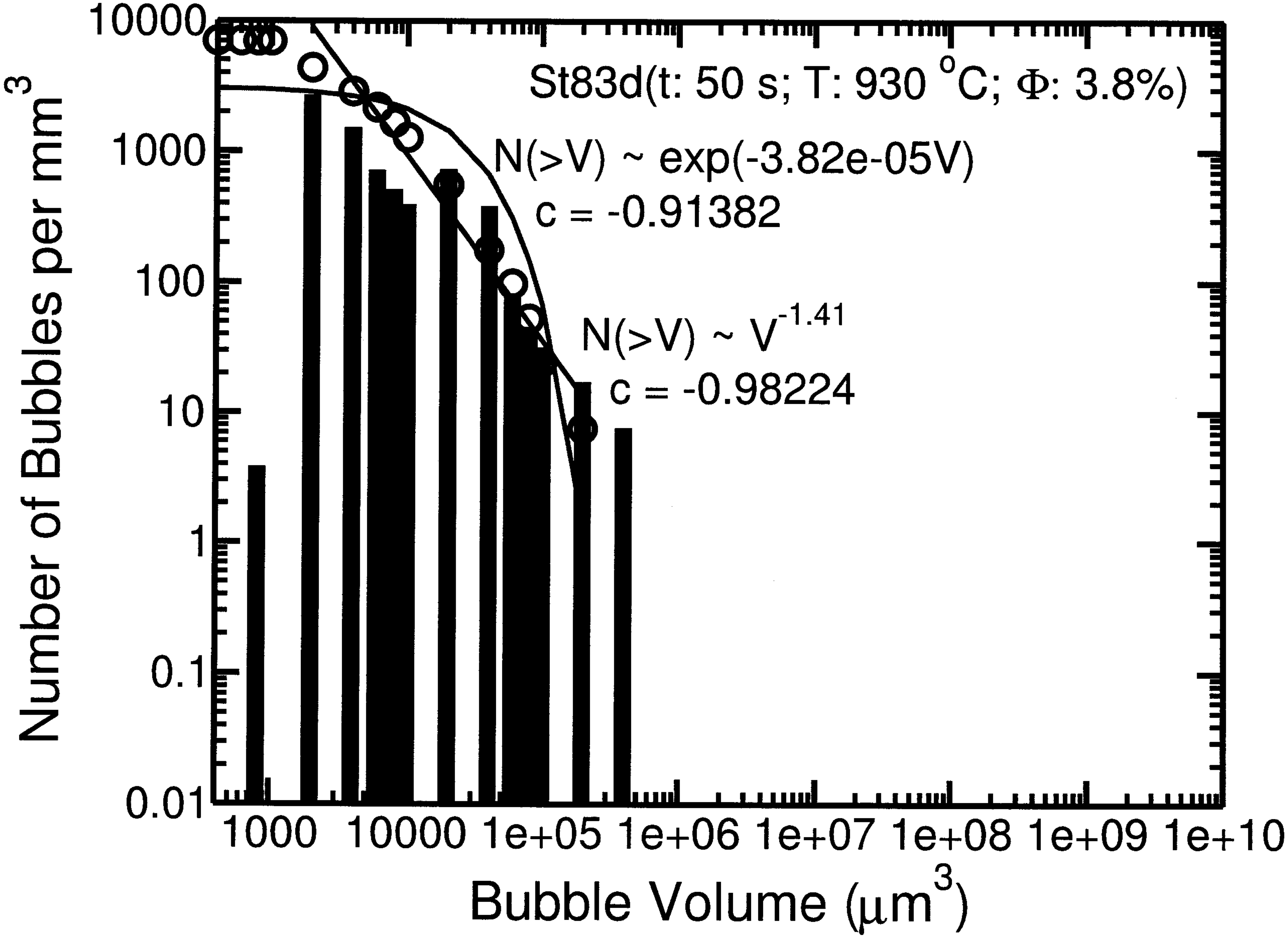
St83d(t: 50 s; T: 930 °C; Φ: 3.8%)
N(>V) ~ exp(-3.82e-05V)
c = -0.91382
N(>V) ~ V^-1.41
c = -0.98224
Number of Bubbles per mm^3
10000
1000
100
10
1
0.1
0.01
1000
10000
1e+05
1e+06
1e+07
1e+08
1e+09
1e+10
Bubble Volume (μm^3)

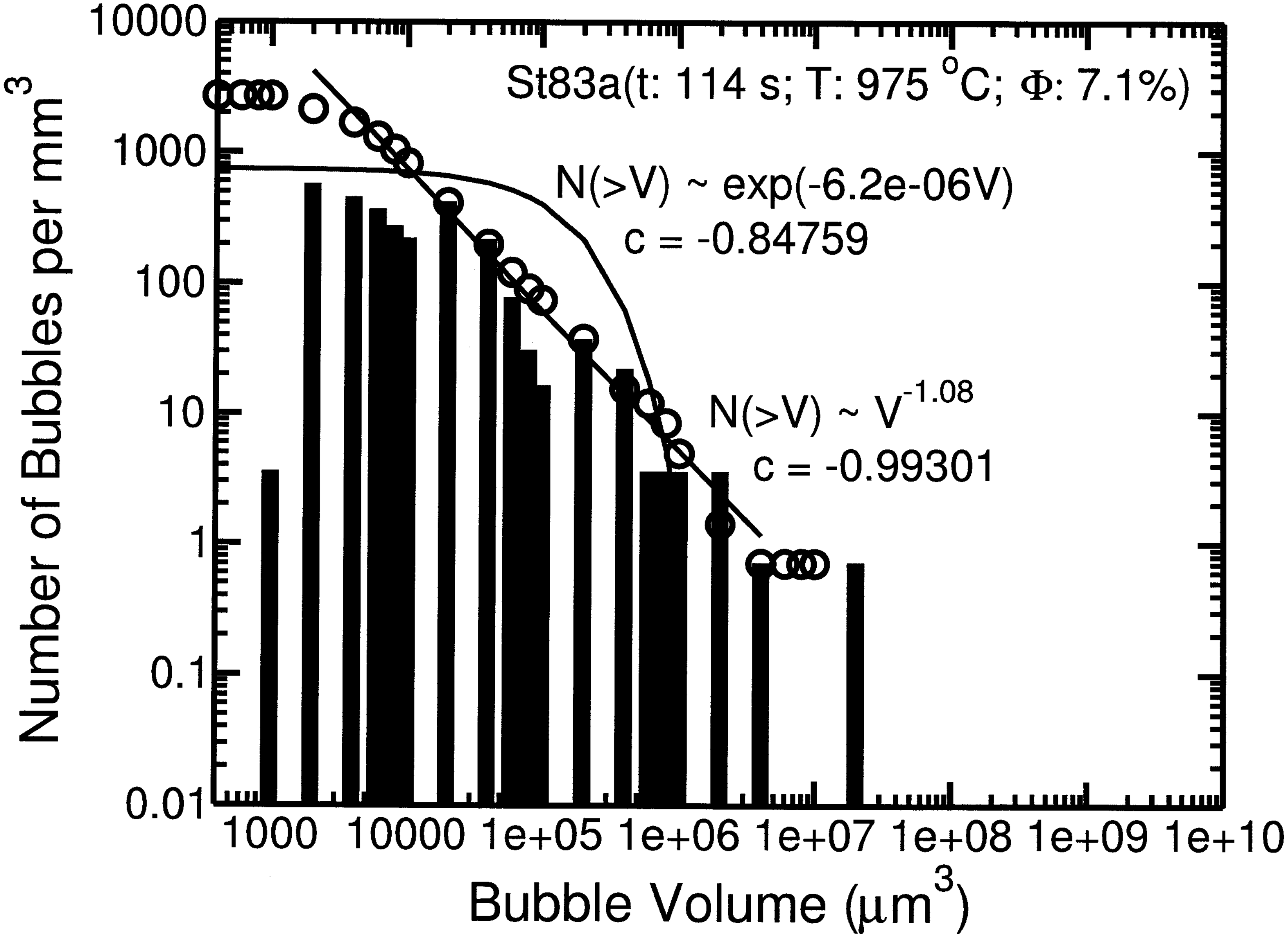
St83a(t: 114 s; T: 975 °C; Φ: 7.1%)
N(>V) ~ exp(-6.2e-06V)
c = -0.84759
N(>V) ~ V^-1.08
c = -0.99301
Number of Bubbles per mm^3
10000
1000
100
10
1
0.1
0.01
1000
10000
1e+05
1e+06
1e+07
1e+08
1e+09
1e+10
Bubble Volume (μm^3)

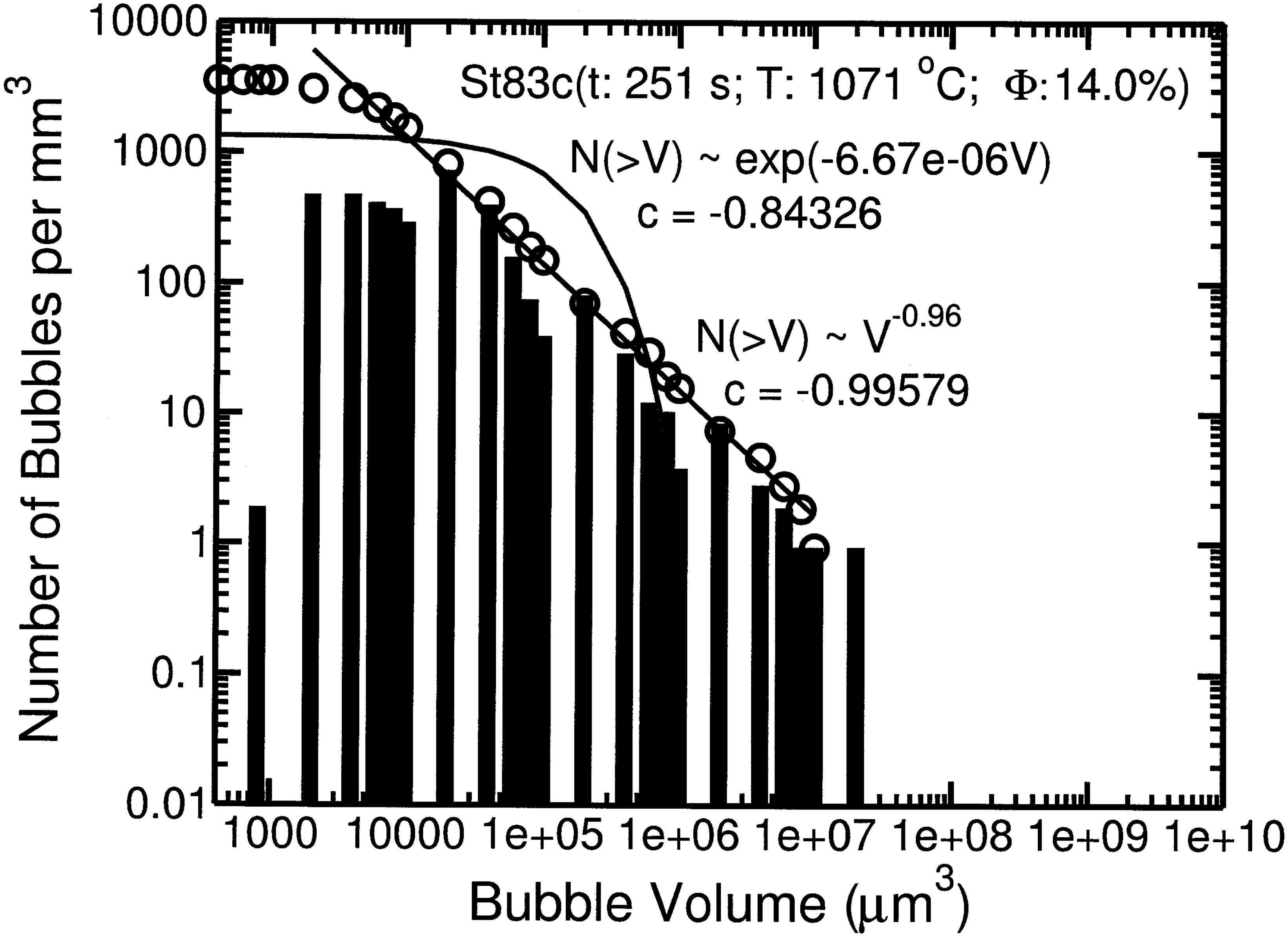
St83c(t: 251 s; T: 1071 °C; Φ:14.0%)
N(>V) ~ exp(-6.67e-06V)
c = -0.84326
N(>V) ~ V^-0.96
c = -0.99579
Number of Bubbles per mm^3
10000
1000
100
10
1
0.1
0.01
1000
10000
1e+05
1e+06
1e+07
1e+08
1e+09
1e+10
Bubble Volume (µm^3)

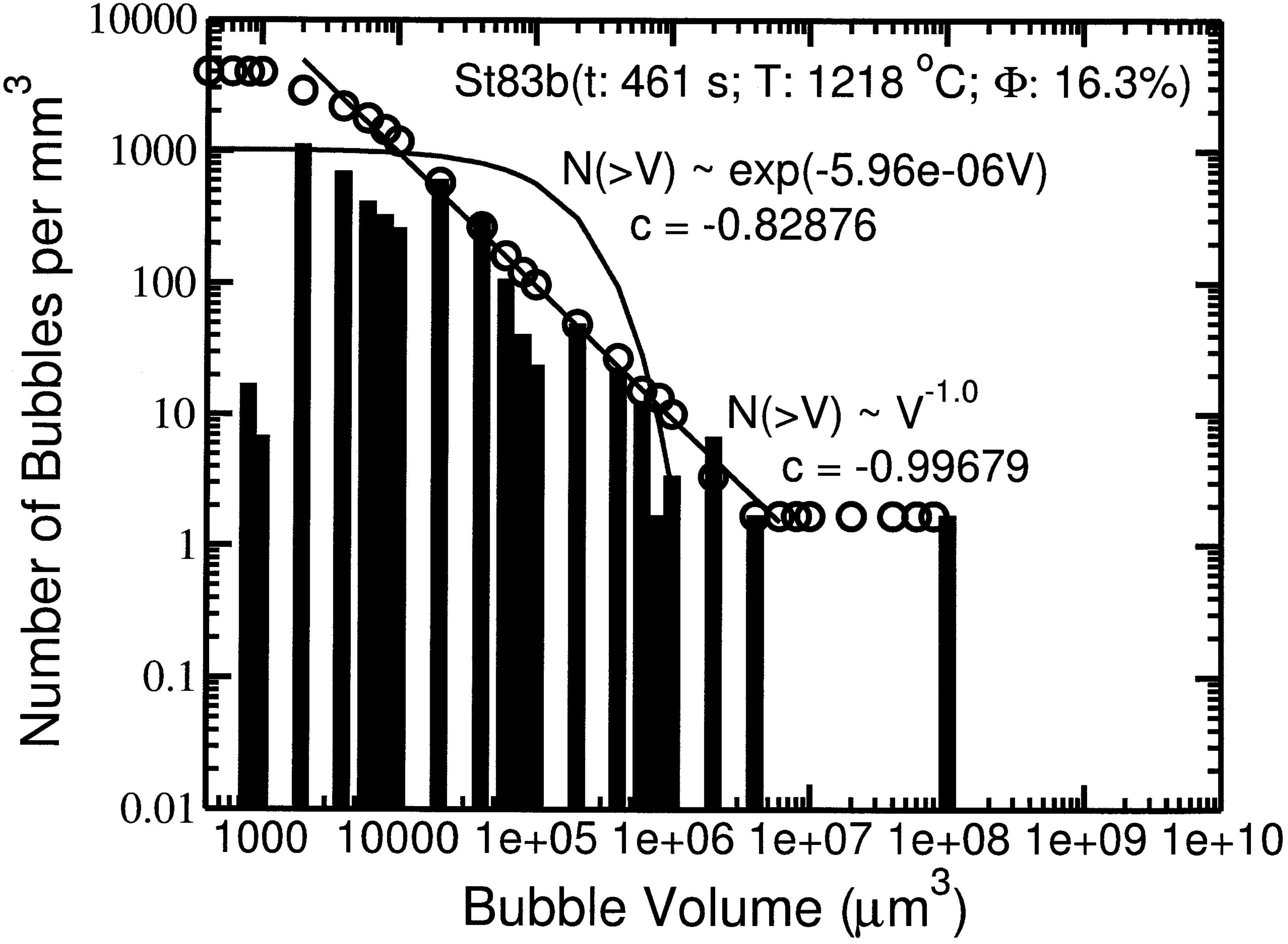
St83b(t: 461 s; T: 1218 °C; Φ: 16.3%)
N(>V) ~ exp(-5.96e-06V)
c = -0.82876
N(>V) ~ V^-1.0
c = -0.99679
Number of Bubbles per mm^3
10000
1000
100
10
1
0.1
0.01
1000
10000
1e+05
1e+06
1e+07
1e+08
1e+09
1e+10
Bubble Volume (μm^3)

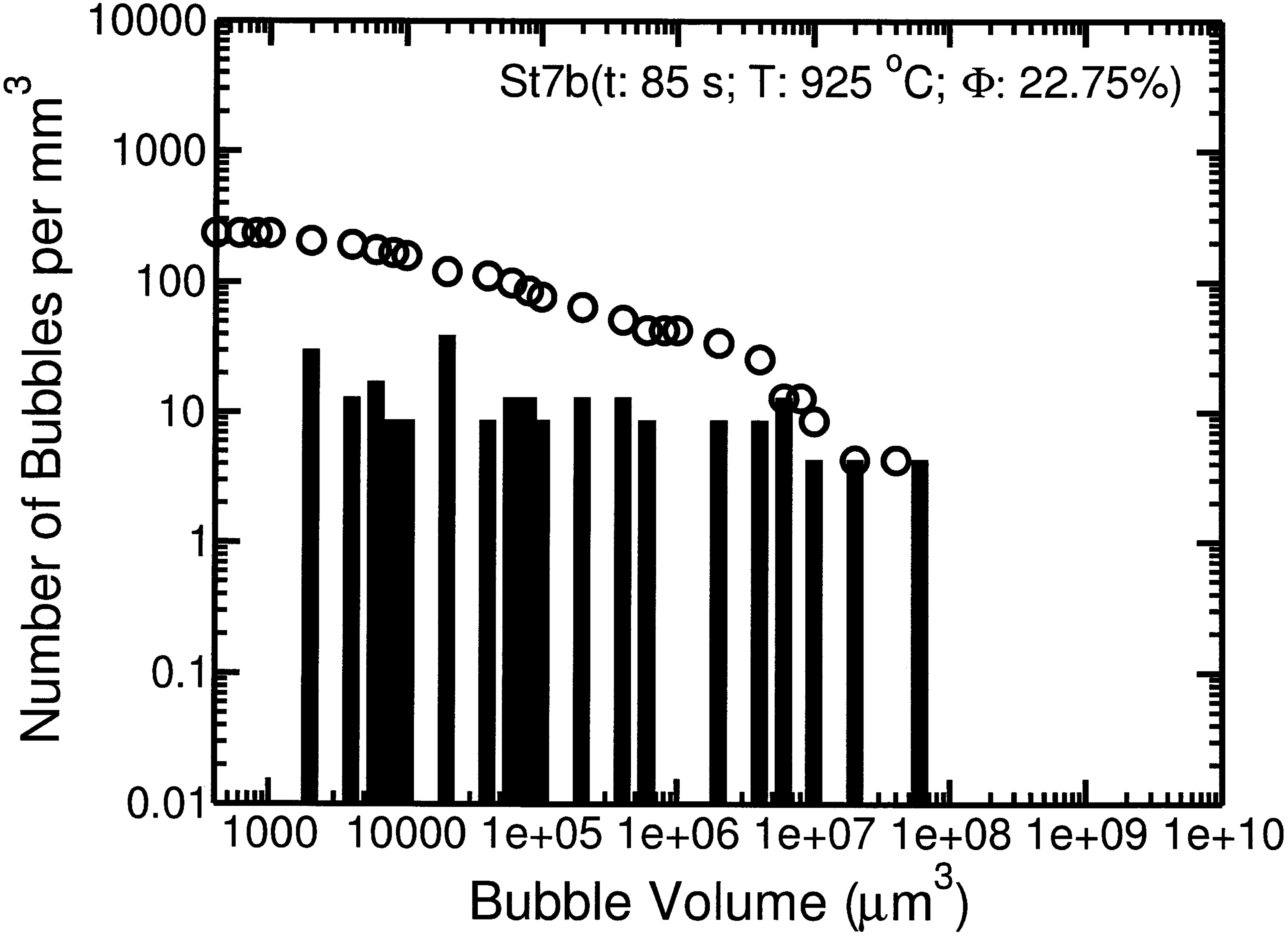
St7b(t: 85 s; T: 925 °C; Φ: 22.75%)
Number of Bubbles per mm$^3$
10000
1000
100
10
1
0.1
0.01
1000
10000
1e+05
1e+06
1e+07
1e+08
1e+09
1e+10
Bubble Volume (µm$^3$)

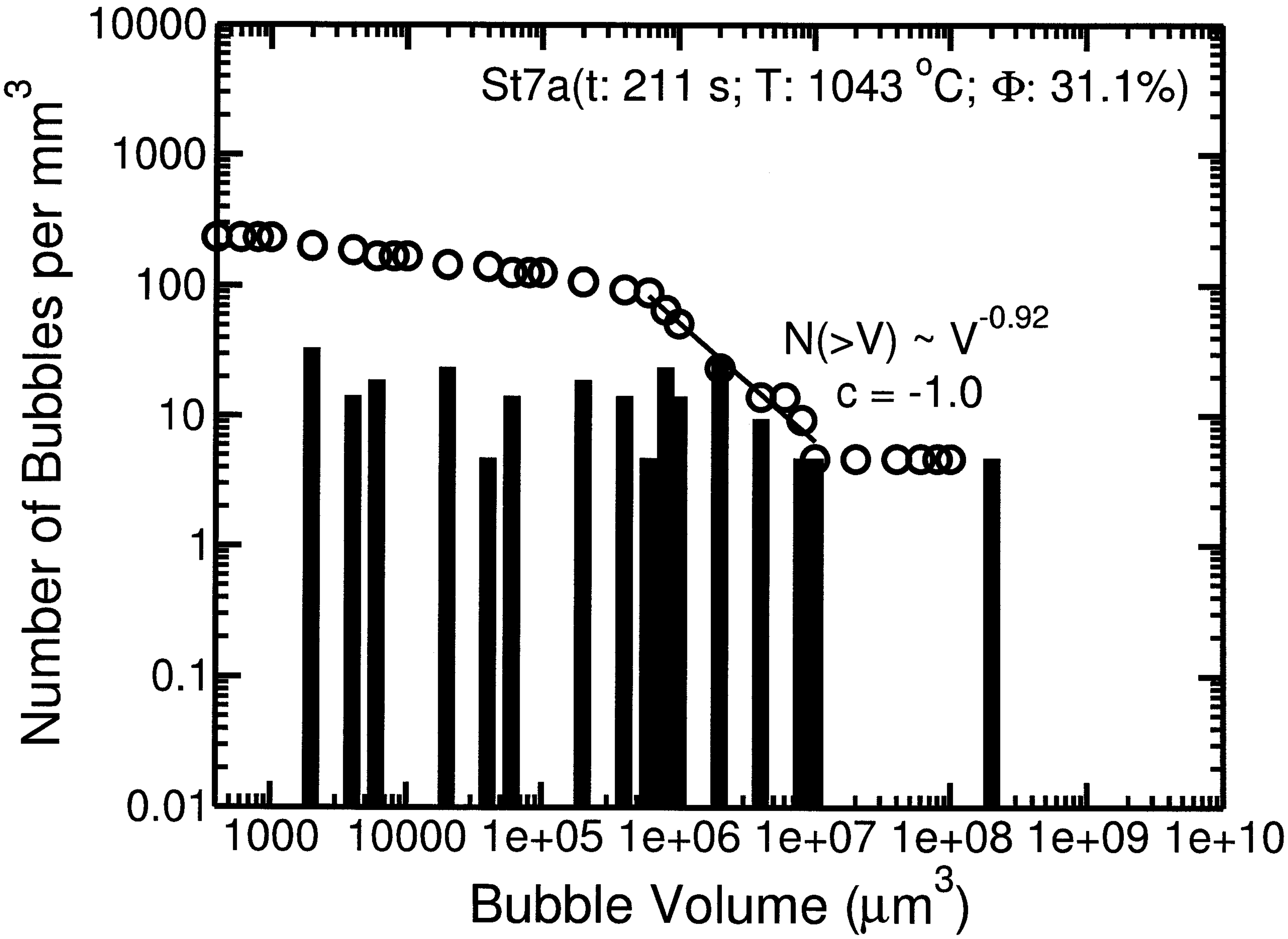
St7a(t: 211 s; T: 1043 °C; Φ: 31.1%)
N(>V) ~ V^-0.92
c = -1.0
Number of Bubbles per mm^3
10000
1000
100
10
1
0.1
0.01
1000
10000
1e+05
1e+06
1e+07
1e+08
1e+09
1e+10
Bubble Volume (μm^3)

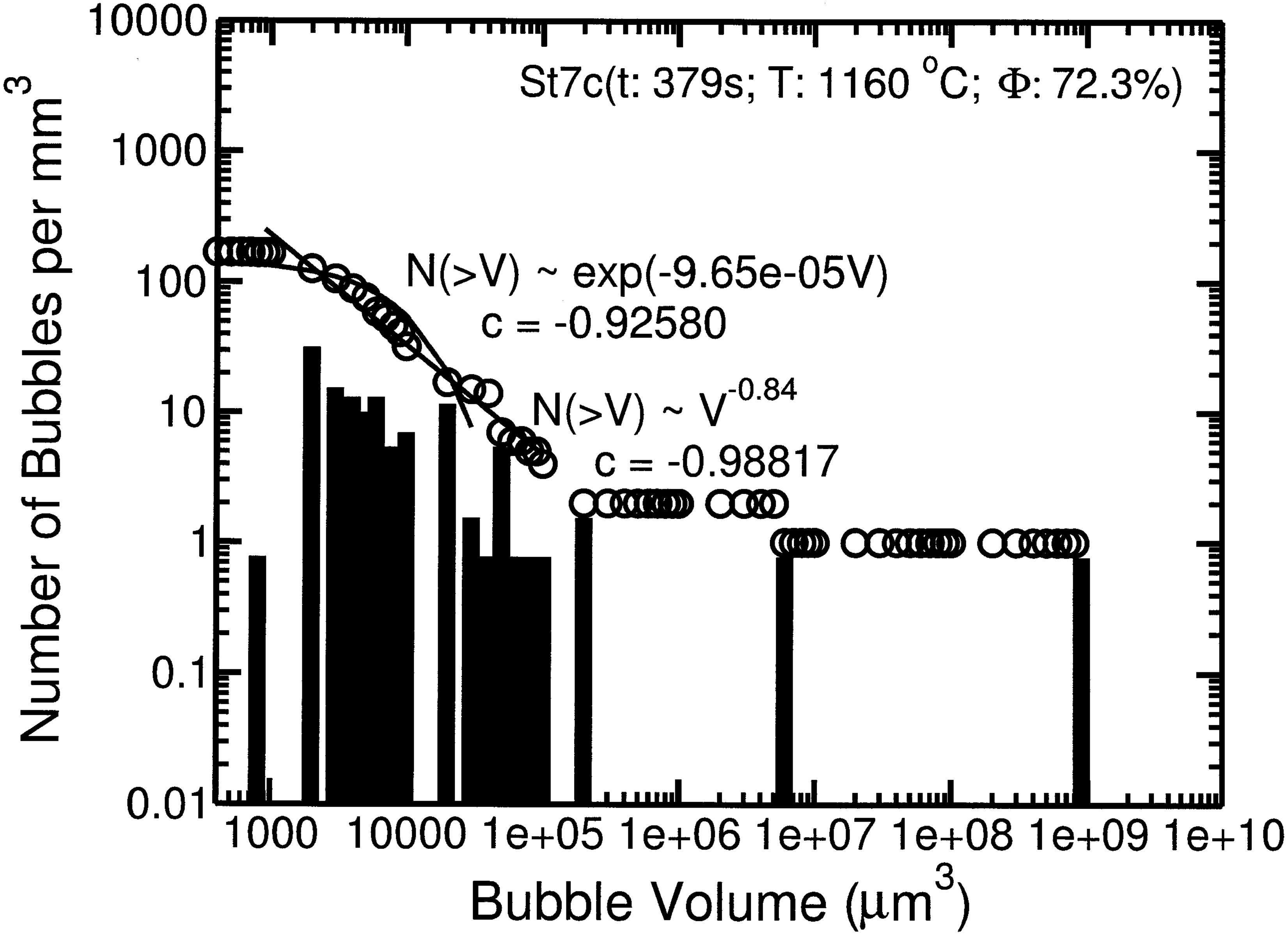
St7c(t: 379s; T: 1160 °C; Φ: 72.3%)
N(>V) ~ exp(-9.65e-05V)
c = -0.92580
N(>V) ~ V^-0.84
c = -0.98817
Number of Bubbles per mm^3
10000
1000
100
10
1
0.1
0.01
1000
10000
1e+05
1e+06
1e+07
1e+08
1e+09
1e+10
Bubble Volume (μm^3)

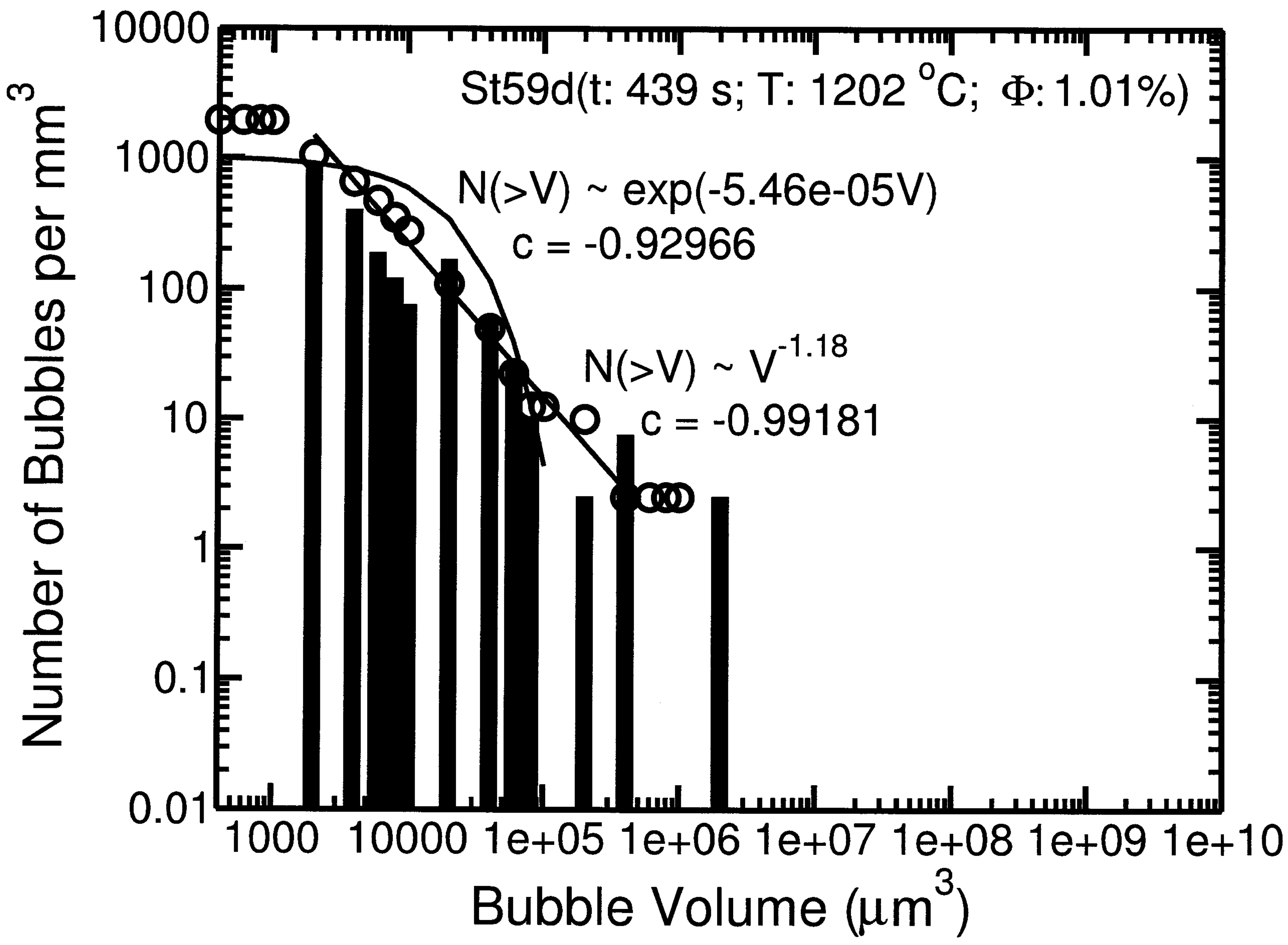
St59d(t: 439 s; T: 1202 °C; Φ: 1.01%)
N(>V) ~ exp(-5.46e-05V)
c = -0.92966
N(>V) ~ V^-1.18
c = -0.99181
Number of Bubbles per mm³
10000
1000
100
10
1
0.1
0.01
1000
10000
1e+05
1e+06
1e+07
1e+08
1e+09
1e+10
Bubble Volume (μm³)

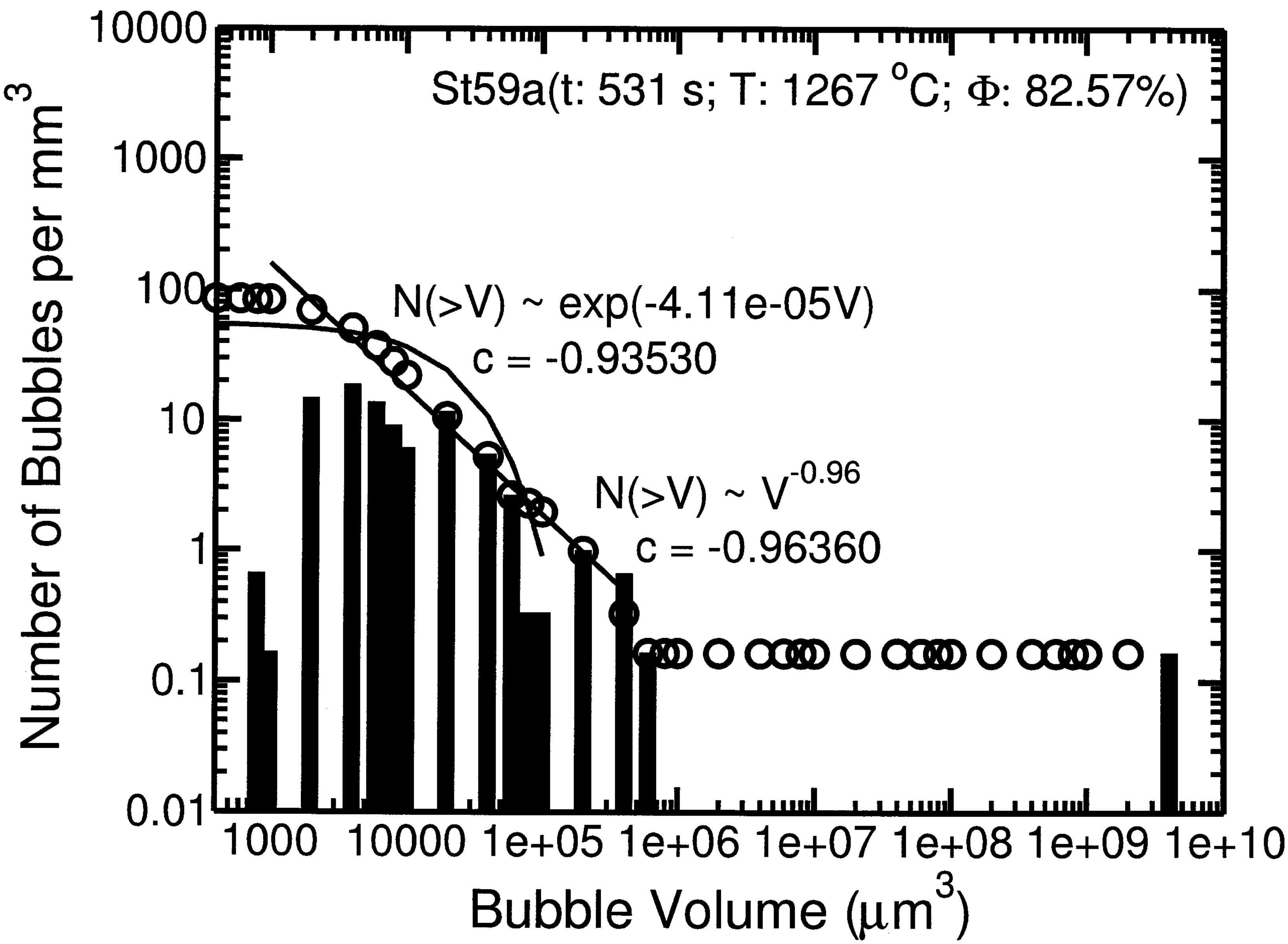
St59a(t: 531 s; T: 1267 °C; Φ: 82.57%)
N(>V) ~ exp(-4.11e-05V)
c = -0.93530
N(>V) ~ V^-0.96
c = -0.96360
Number of Bubbles per mm^3
10000
1000
100
10
1
0.1
0.01
1000
10000
1e+05
1e+06
1e+07
1e+08
1e+09
1e+10
Bubble Volume (μm^3)

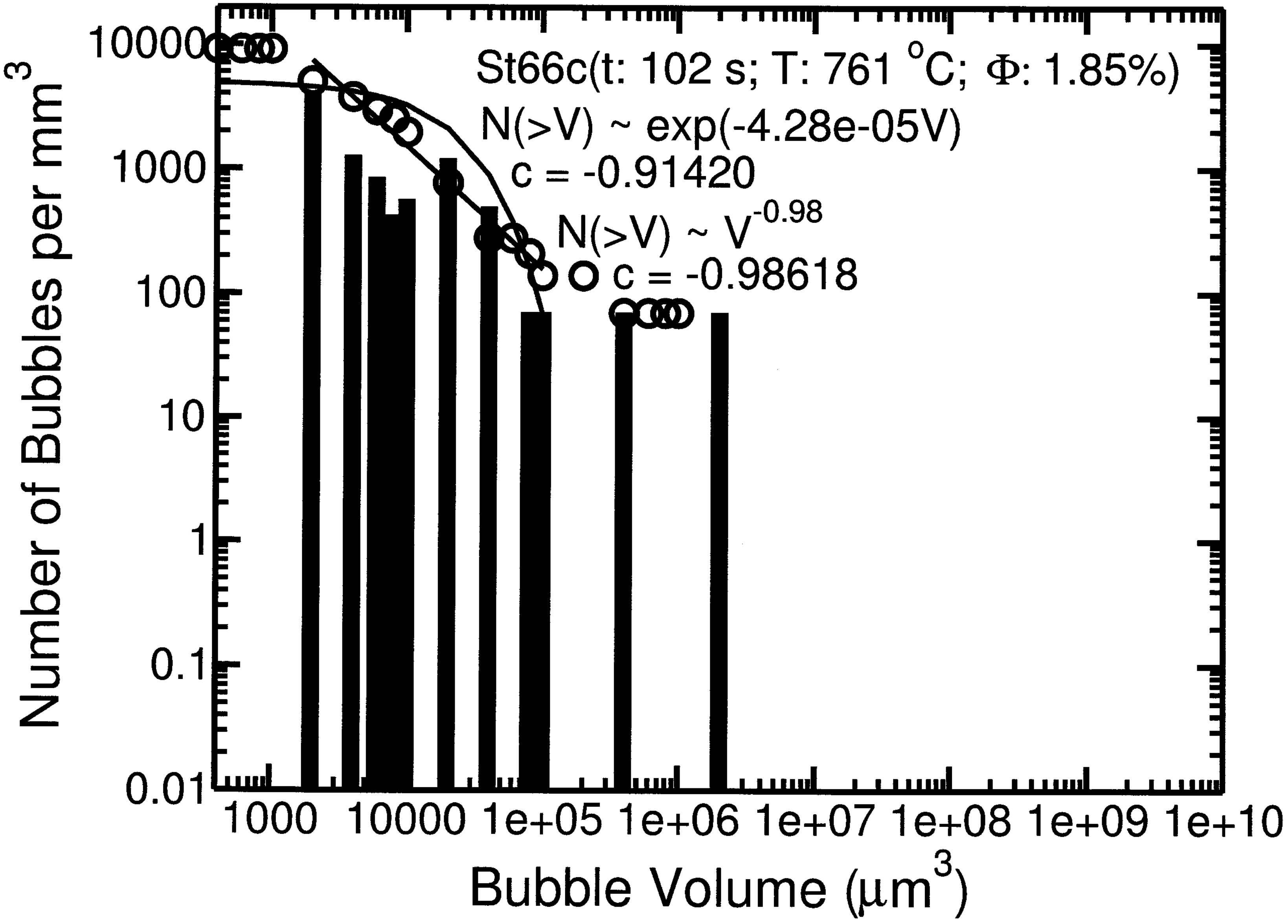
St66c(t: 102 s; T: 761 °C; Φ: 1.85%)
N(>V) ~ exp(-4.28e-05V)
c = -0.91420
N(>V) ~ V^-0.98
c = -0.98618
Number of Bubbles per mm^3
10000
1000
100
10
1
0.1
0.01
1000
10000
1e+05
1e+06
1e+07
1e+08
1e+09
1e+10
Bubble Volume (μm^3)

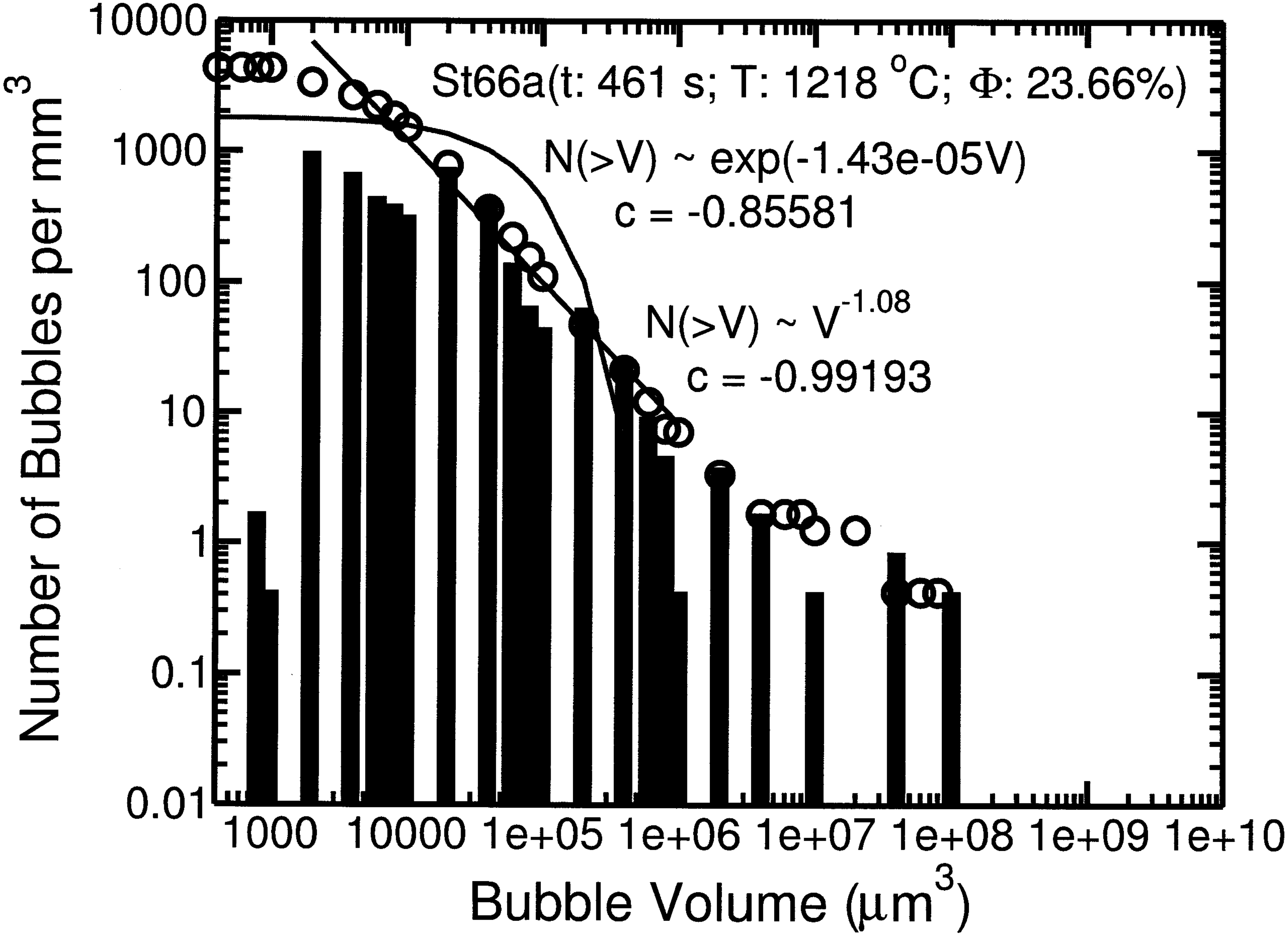
St66a(t: 461 s; T: 1218 °C; Φ: 23.66%)
N(>V) ~ exp(-1.43e-05V)
c = -0.85581
N(>V) ~ V^-1.08
c = -0.99193
Number of Bubbles per mm^3
Bubble Volume (μm^3)
10000
1000
100
10
1
0.1
0.01
1000
10000
1e+05
1e+06
1e+07
1e+08
1e+09
1e+10

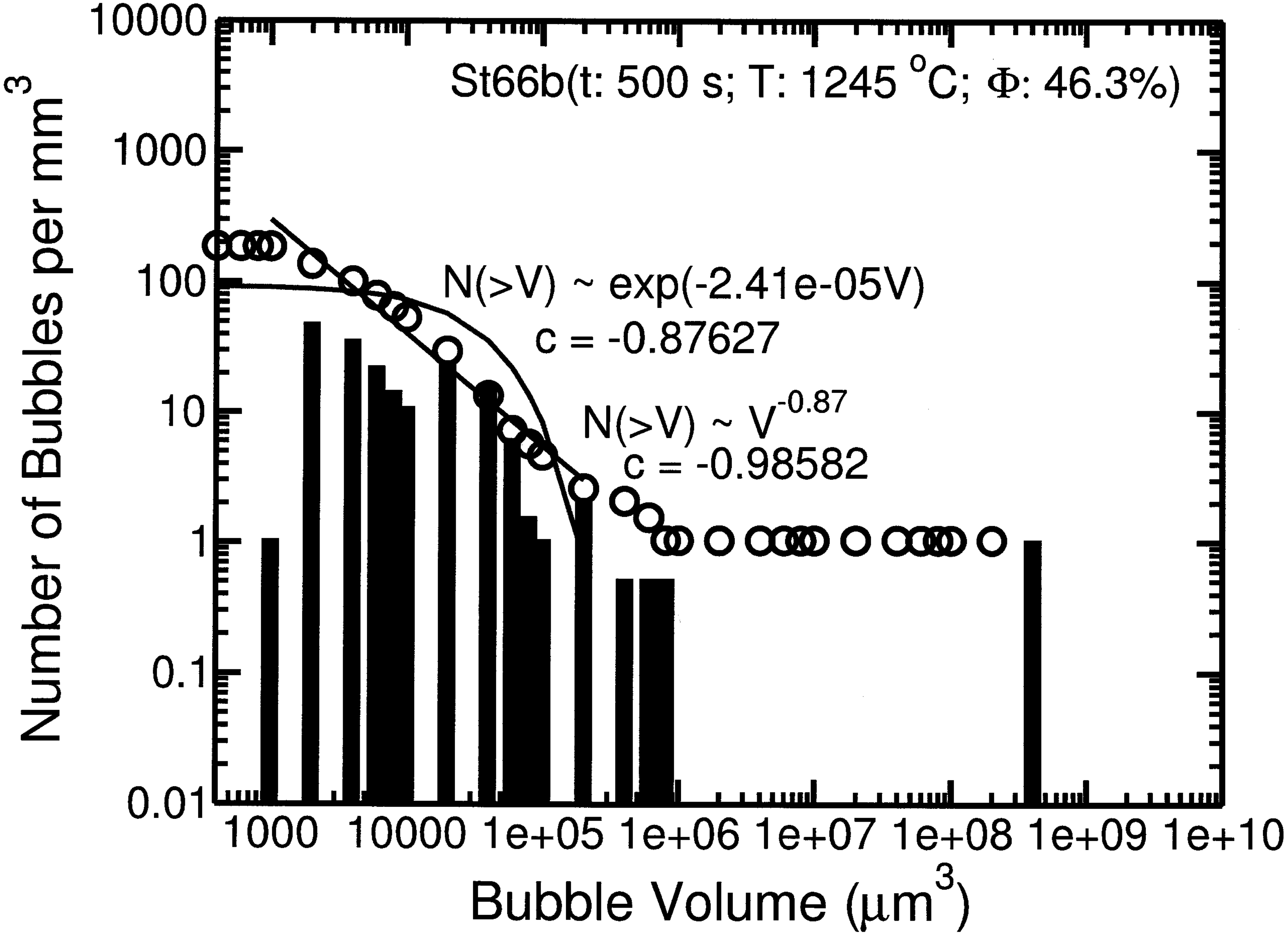
St66b(t: 500 s; T: 1245 °C; Φ: 46.3%)
N(>V) ~ exp(-2.41e-05V)
c = -0.87627
N(>V) ~ V^-0.87
c = -0.98582
Number of Bubbles per mm^3
10000
1000
100
10
1
0.1
0.01
1000
10000
1e+05
1e+06
1e+07
1e+08
1e+09
1e+10
Bubble Volume (μm^3)

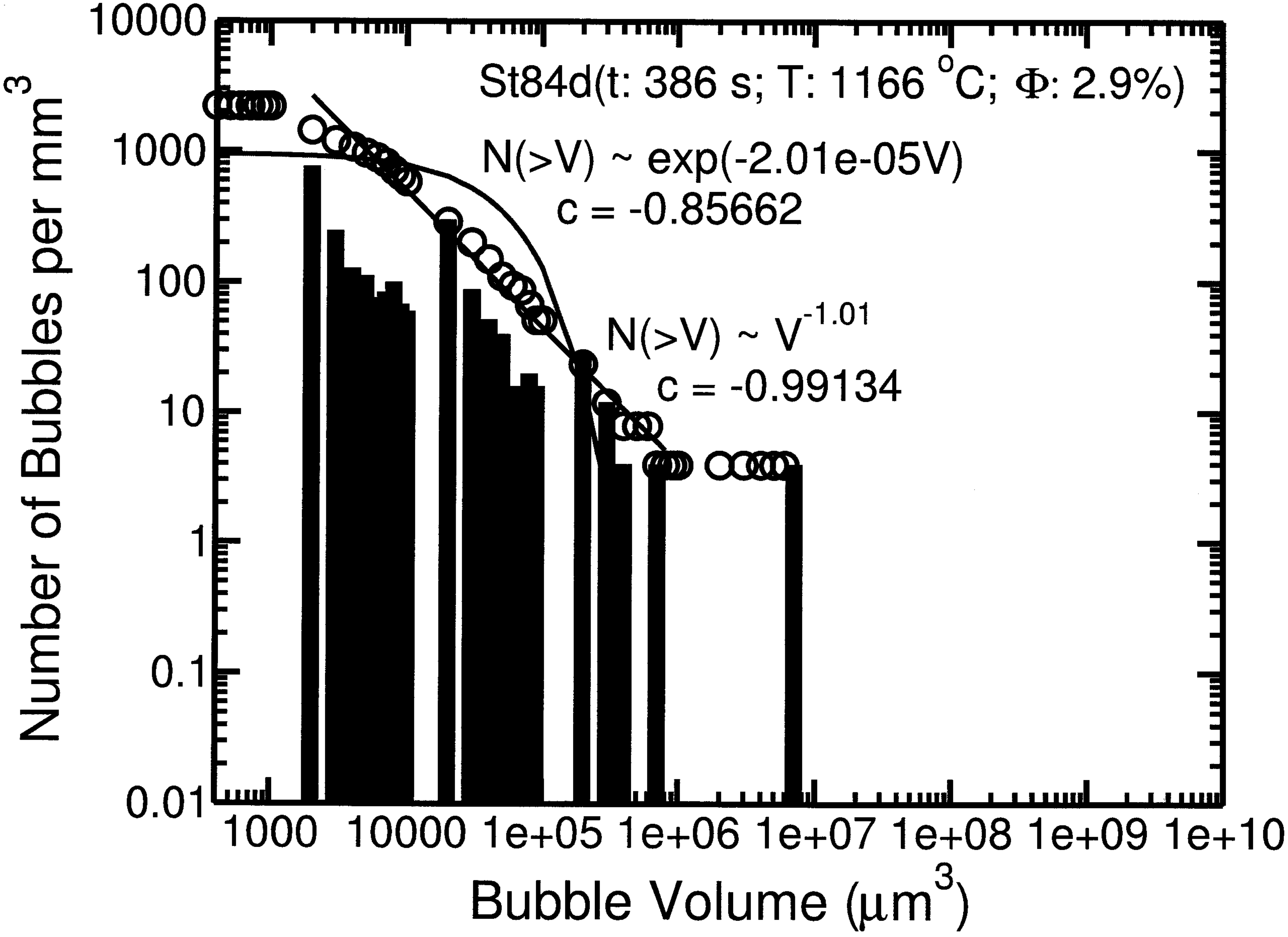
St84d(t: 386 s; T: 1166 °C; Φ: 2.9%)
N(>V) ~ exp(-2.01e-05V)
c = -0.85662
N(>V) ~ V^-1.01
c = -0.99134
Number of Bubbles per mm^3
10000
1000
100
10
1
0.1
0.01
1000
10000
1e+05
1e+06
1e+07
1e+08
1e+09
1e+10
Bubble Volume (μm^3)

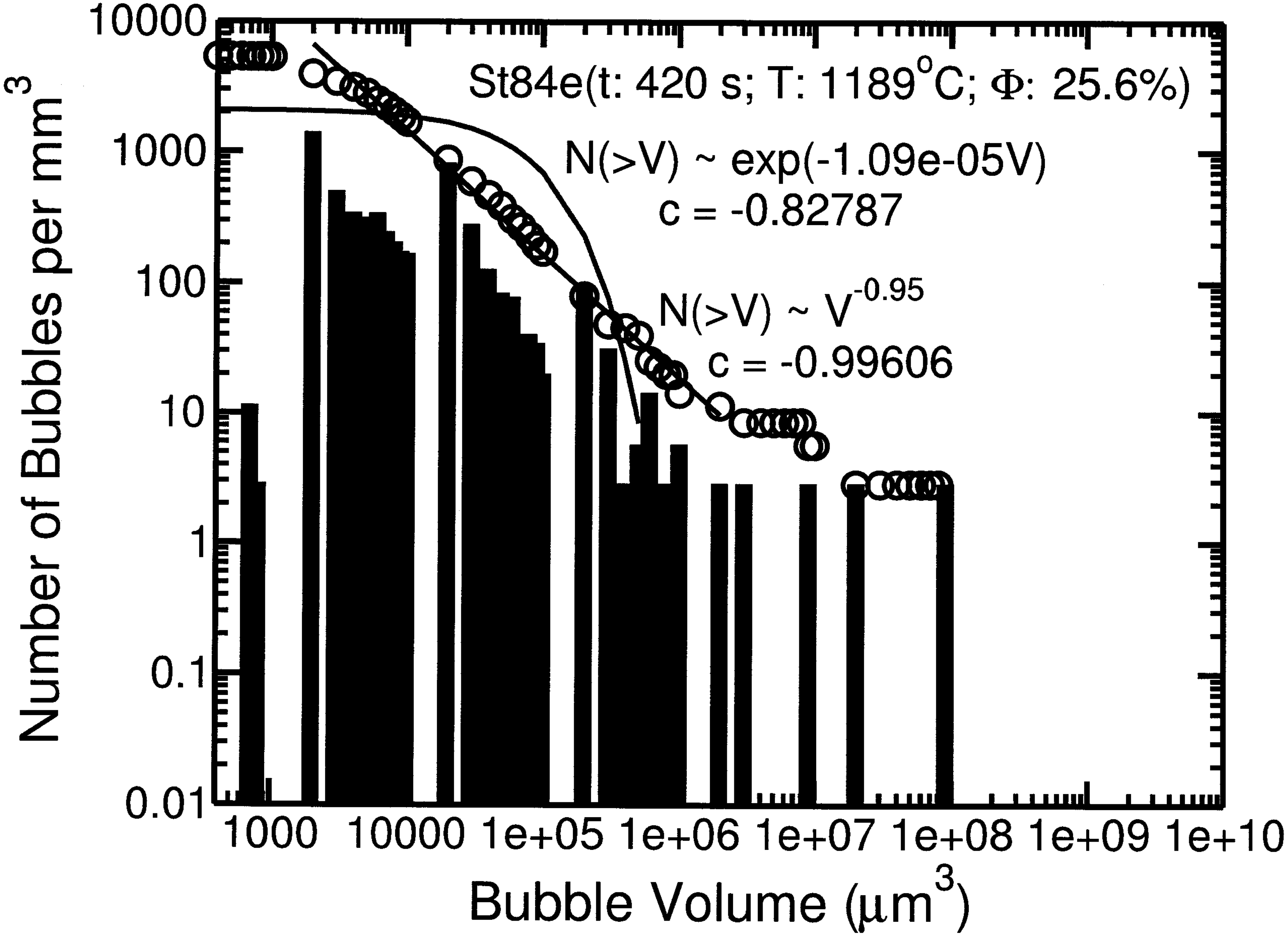
St84e(t: 420 s; T: 1189°C; Φ: 25.6%)
N(>V) ~ exp(-1.09e-05V)
c = -0.82787
N(>V) ~ V^-0.95
c = -0.99606
Number of Bubbles per mm^3
10000
1000
100
10
1
0.1
0.01
1000
10000
1e+05
1e+06
1e+07
1e+08
1e+09
1e+10
Bubble Volume (μm^3)

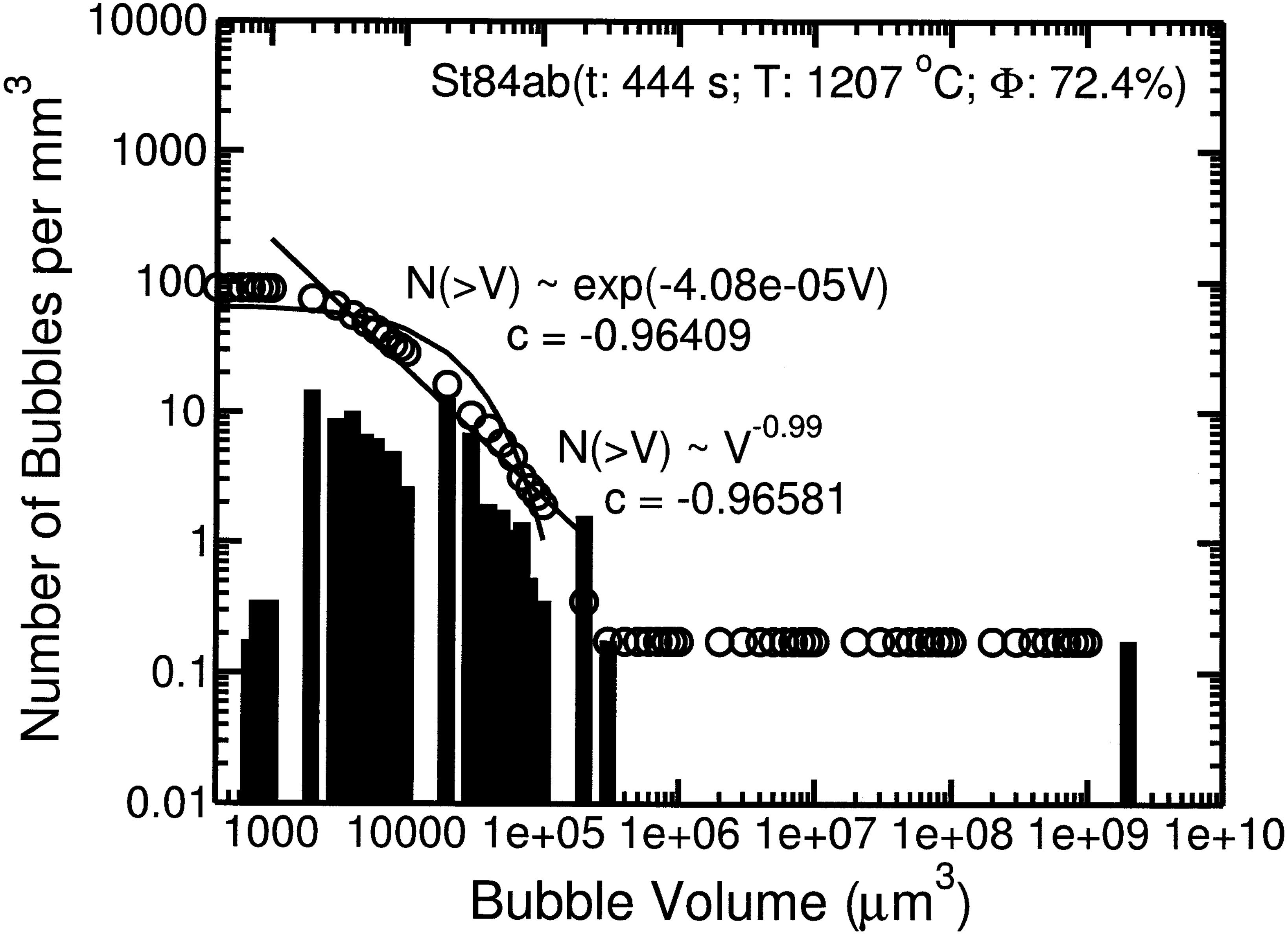
St84ab(t: 444 s; T: 1207 °C; Φ: 72.4%)
N(>V) ~ exp(-4.08e-05V)
c = -0.96409
N(>V) ~ V^-0.99
c = -0.96581
Number of Bubbles per mm^3
10000
1000
100
10
1
0.1
0.01
1000
10000
1e+05
1e+06
1e+07
1e+08
1e+09
1e+10
Bubble Volume (μm^3)

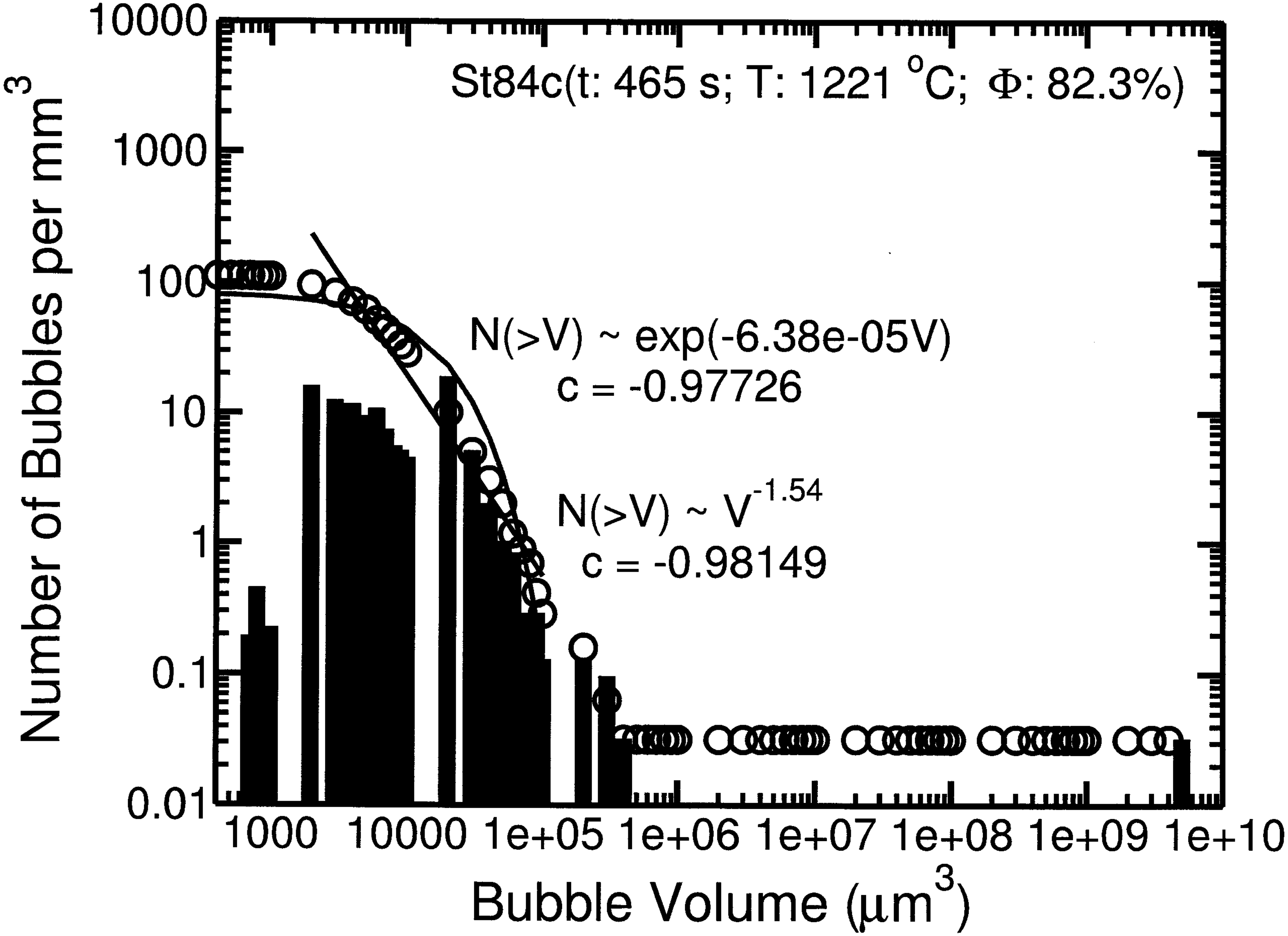
St84c(t: 465 s; T: 1221 °C; Φ: 82.3%)
N(>V) ~ exp(-6.38e-05V)
c = -0.97726
N(>V) ~ V^-1.54
c = -0.98149
Number of Bubbles per mm^3
10000
1000
100
10
1
0.1
0.01
1000
10000
1e+05
1e+06
1e+07
1e+08
1e+09
1e+10
Bubble Volume (μm^3)

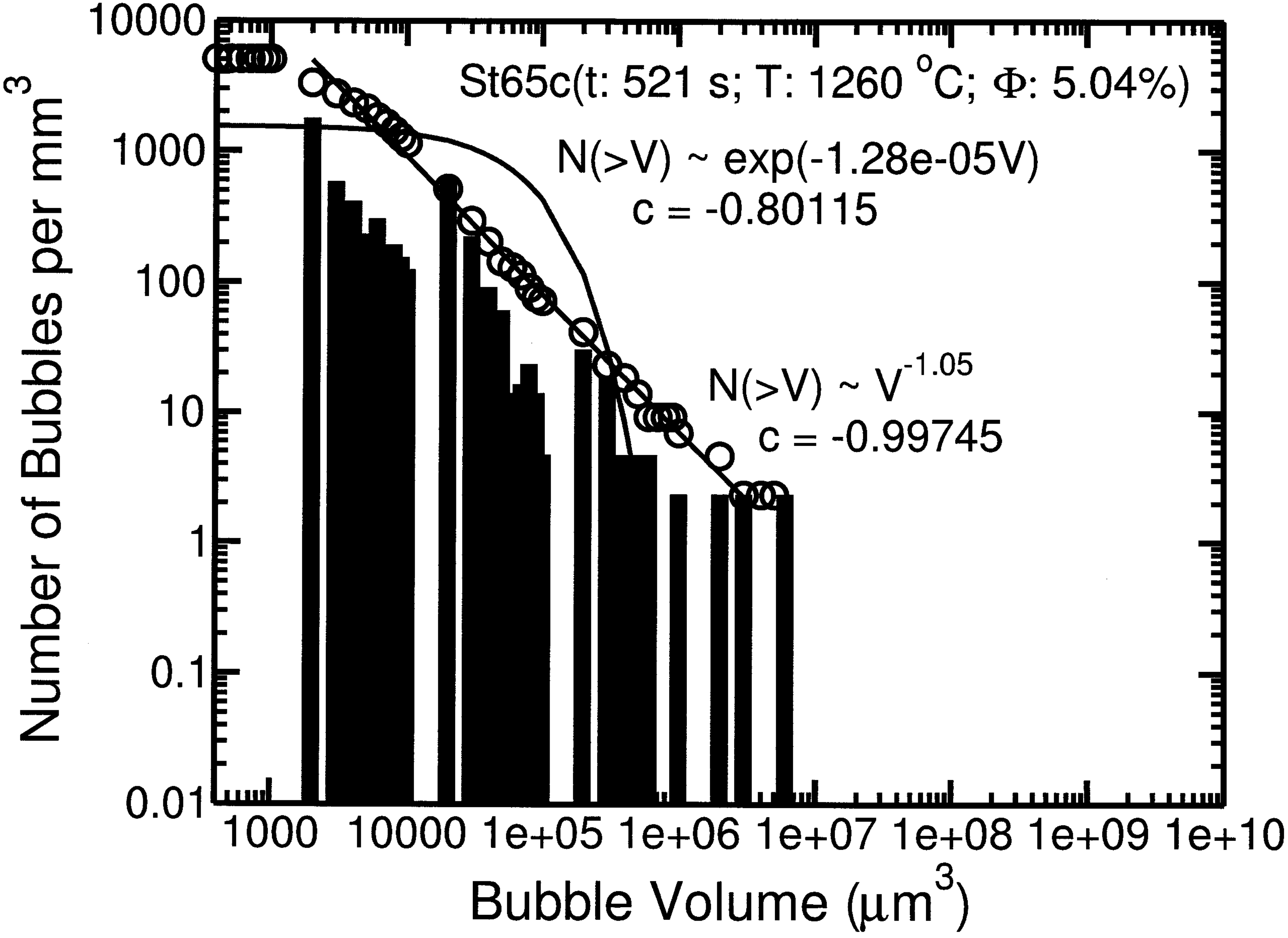
St65c(t: 521 s; T: 1260 °C; Φ: 5.04%)
N(>V) ~ exp(-1.28e-05V)
c = -0.80115
N(>V) ~ V^-1.05
c = -0.99745
Number of Bubbles per mm³
10000
1000
100
10
1
0.1
0.01
1000
10000
1e+05
1e+06
1e+07
1e+08
1e+09
1e+10
Bubble Volume (μm³)

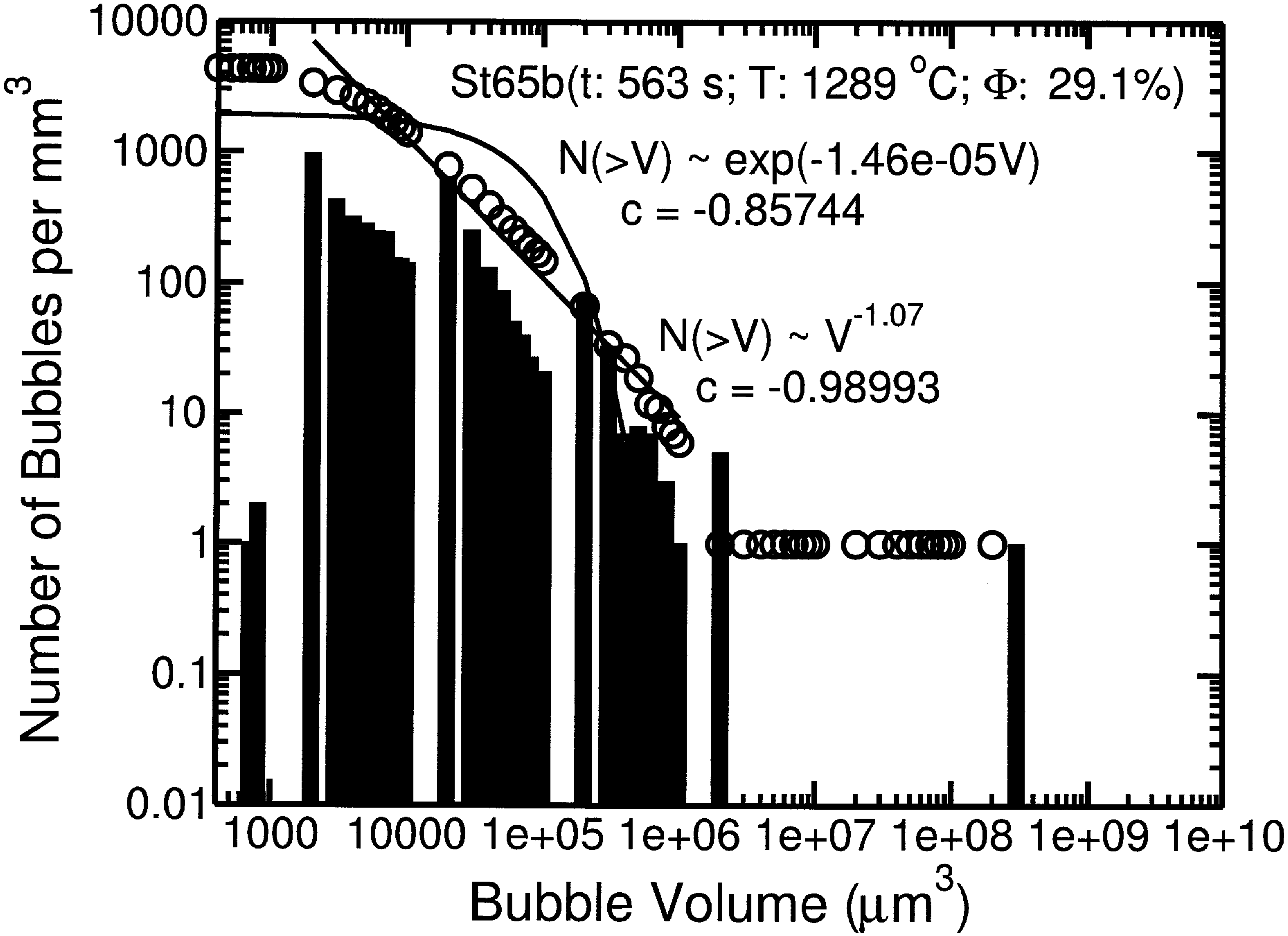
St65b(t: 563 s; T: 1289 °C; Φ: 29.1%)
N(>V) ~ exp(-1.46e-05V)
c = -0.85744
N(>V) ~ V^-1.07
c = -0.98993
Number of Bubbles per mm³
10000
1000
100
10
1
0.1
0.01
1000
10000
1e+05
1e+06
1e+07
1e+08
1e+09
1e+10
Bubble Volume (μm³)

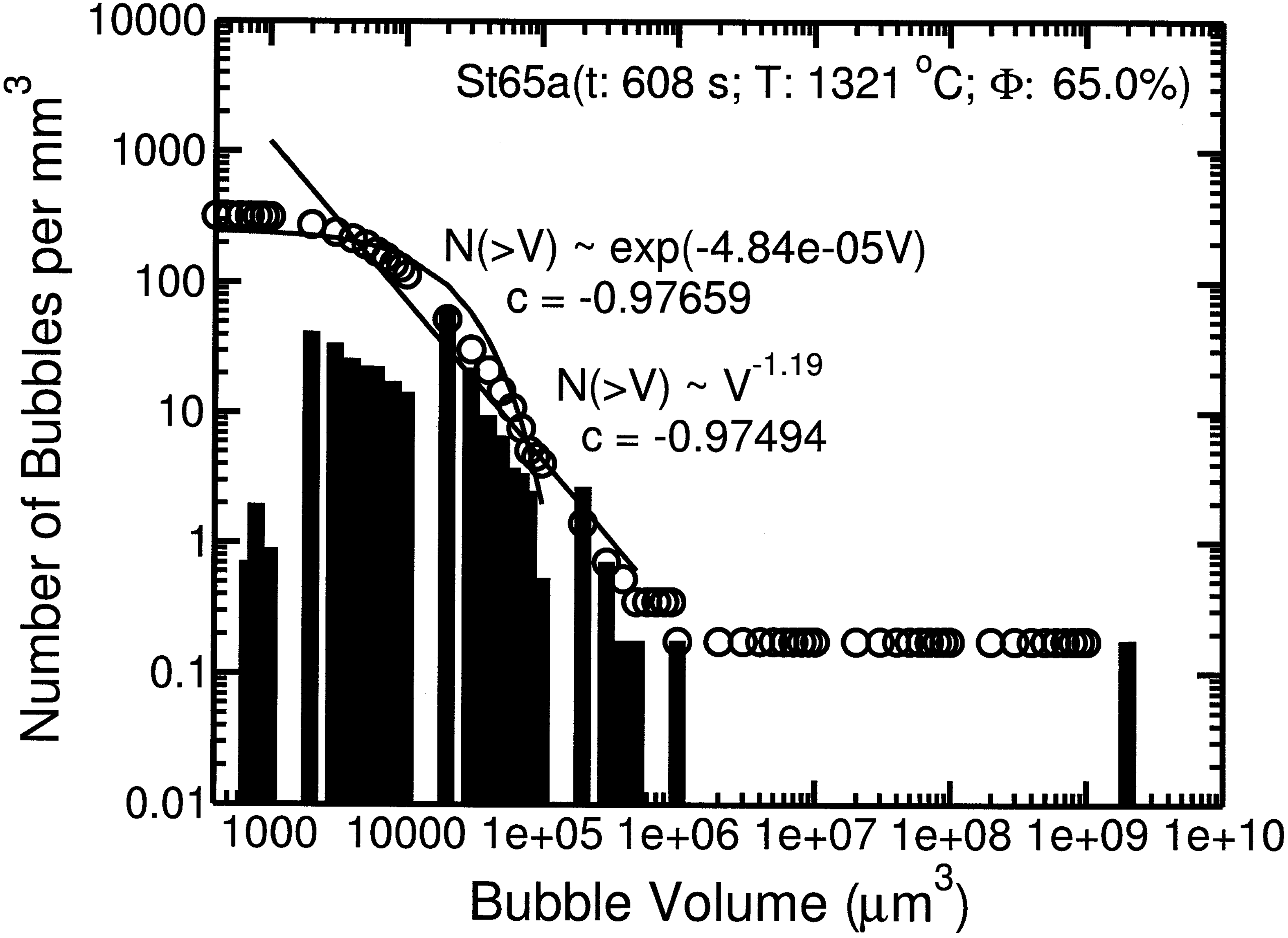
St65a(t: 608 s; T: 1321 °C; Φ: 65.0%)
N(>V) ~ exp(-4.84e-05V)
c = -0.97659
N(>V) ~ V^-1.19
c = -0.97494
Number of Bubbles per mm3
10000
1000
100
10
1
0.1
0.01
1000
10000
1e+05
1e+06
1e+07
1e+08
1e+09
1e+10
Bubble Volume (μm3)

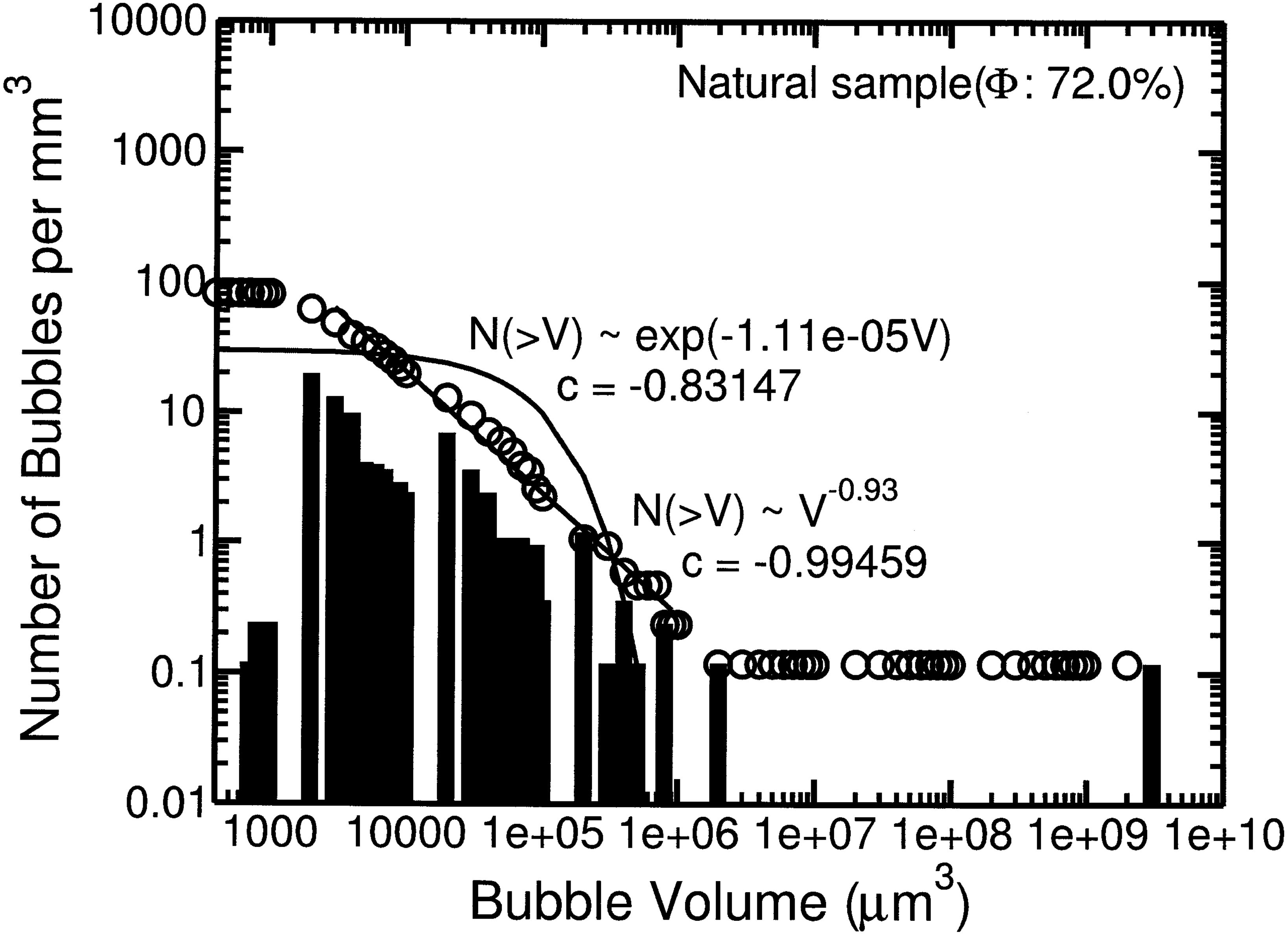
Natural sample(Φ: 72.0%)
N(>V) ~ exp(-1.11e-05V)
c = -0.83147
N(>V) ~ V$^{-0.93}$
c = -0.99459
Number of Bubbles per mm$^3$
10000
1000
100
10
1
0.1
0.01
1000
10000
1e+05
1e+06
1e+07
1e+08
1e+09
1e+10
Bubble Volume (μm$^3$)

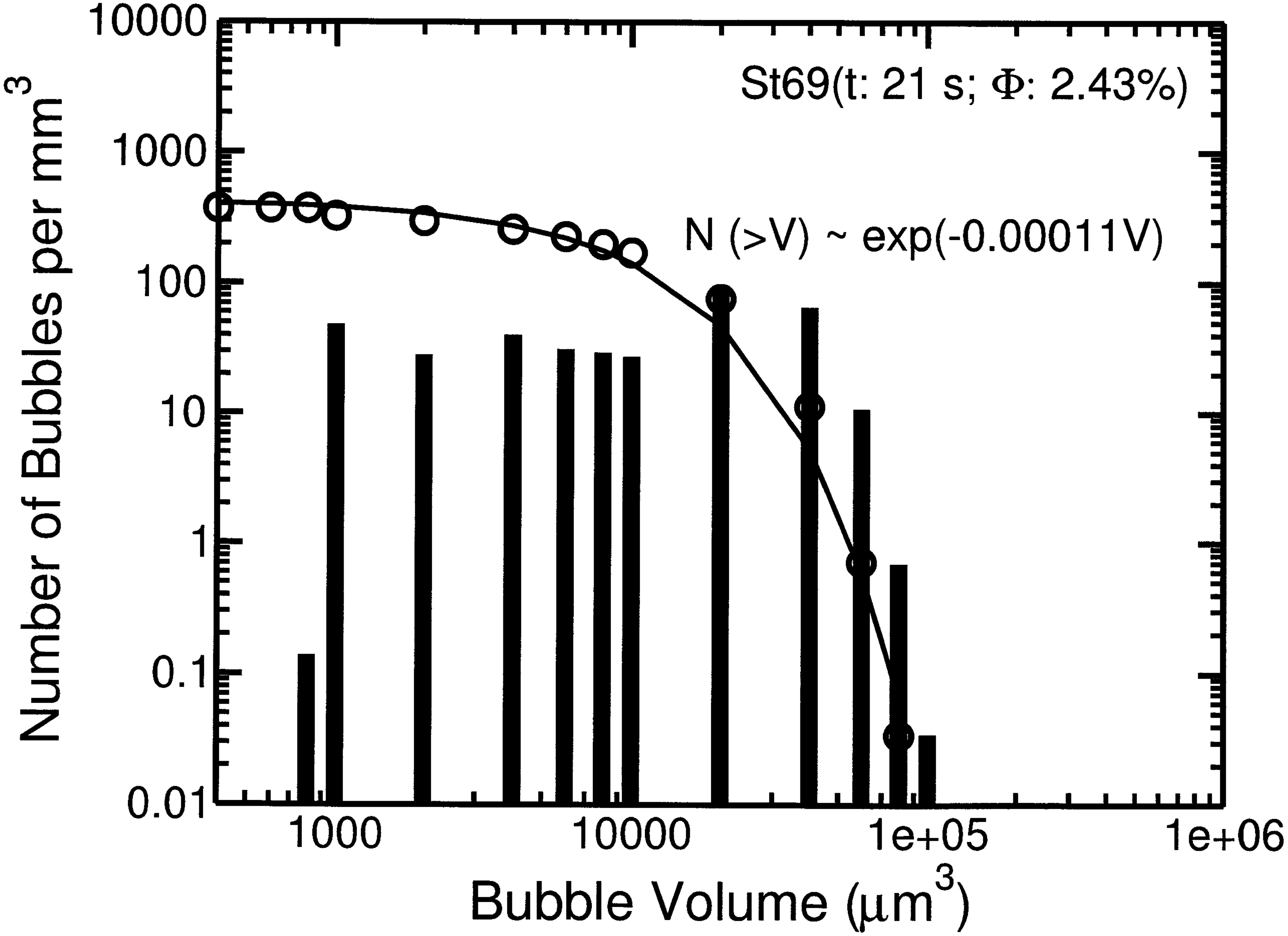
St69(t: 21 s; Φ: 2.43%)
N (>V) ~ exp(-0.00011V)
Number of Bubbles per mm$^3$
10000
1000
100
10
1
0.1
0.01
1000
10000
1e+05
1e+06
Bubble Volume (μm$^3$)

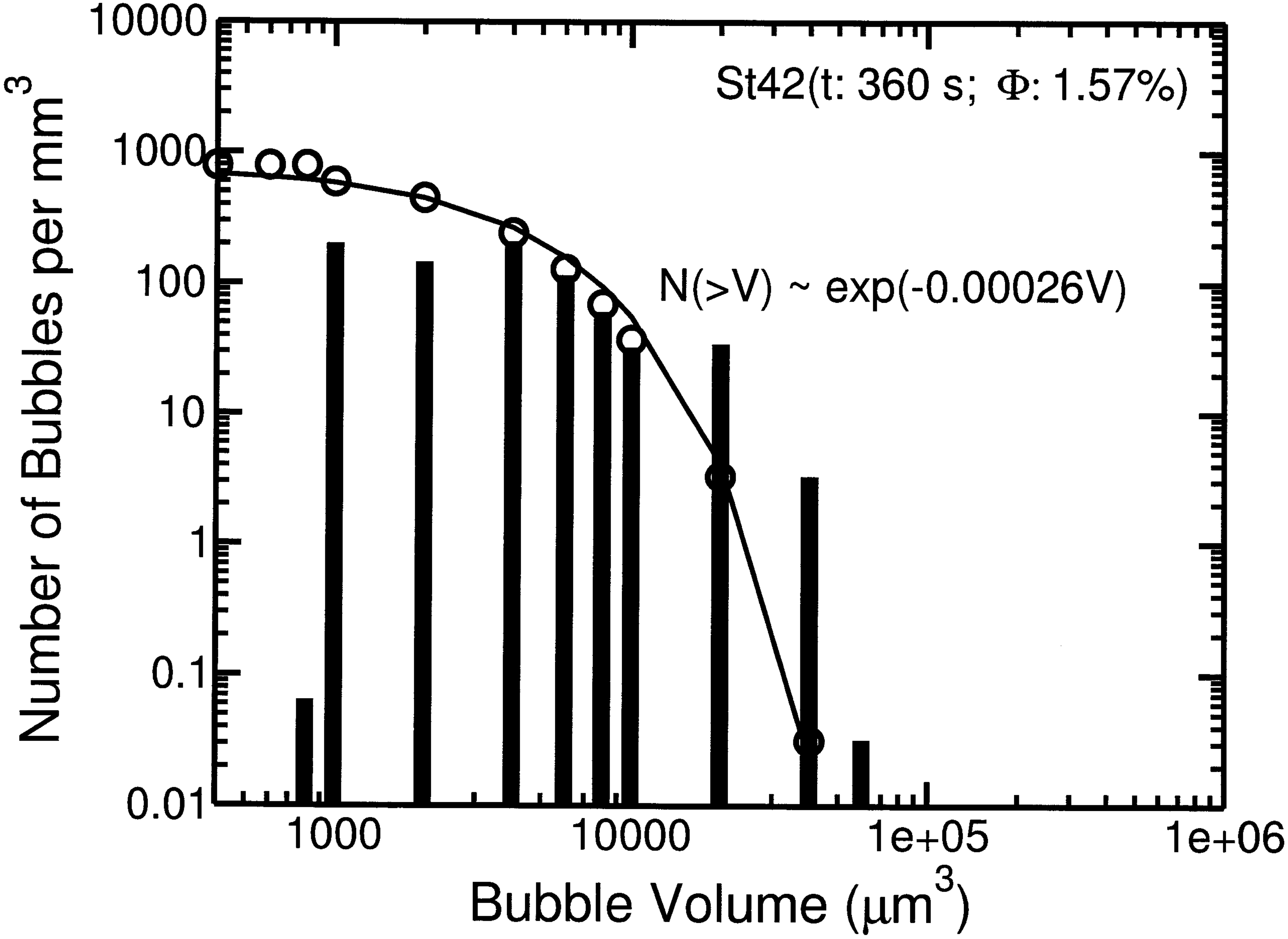
St42(t: 360 s; Φ: 1.57%)
N(>V) ~ exp(-0.00026V)
Number of Bubbles per mm^3
10000
1000
100
10
1
0.1
0.01
1000
10000
1e+05
1e+06
Bubble Volume (μm^3)

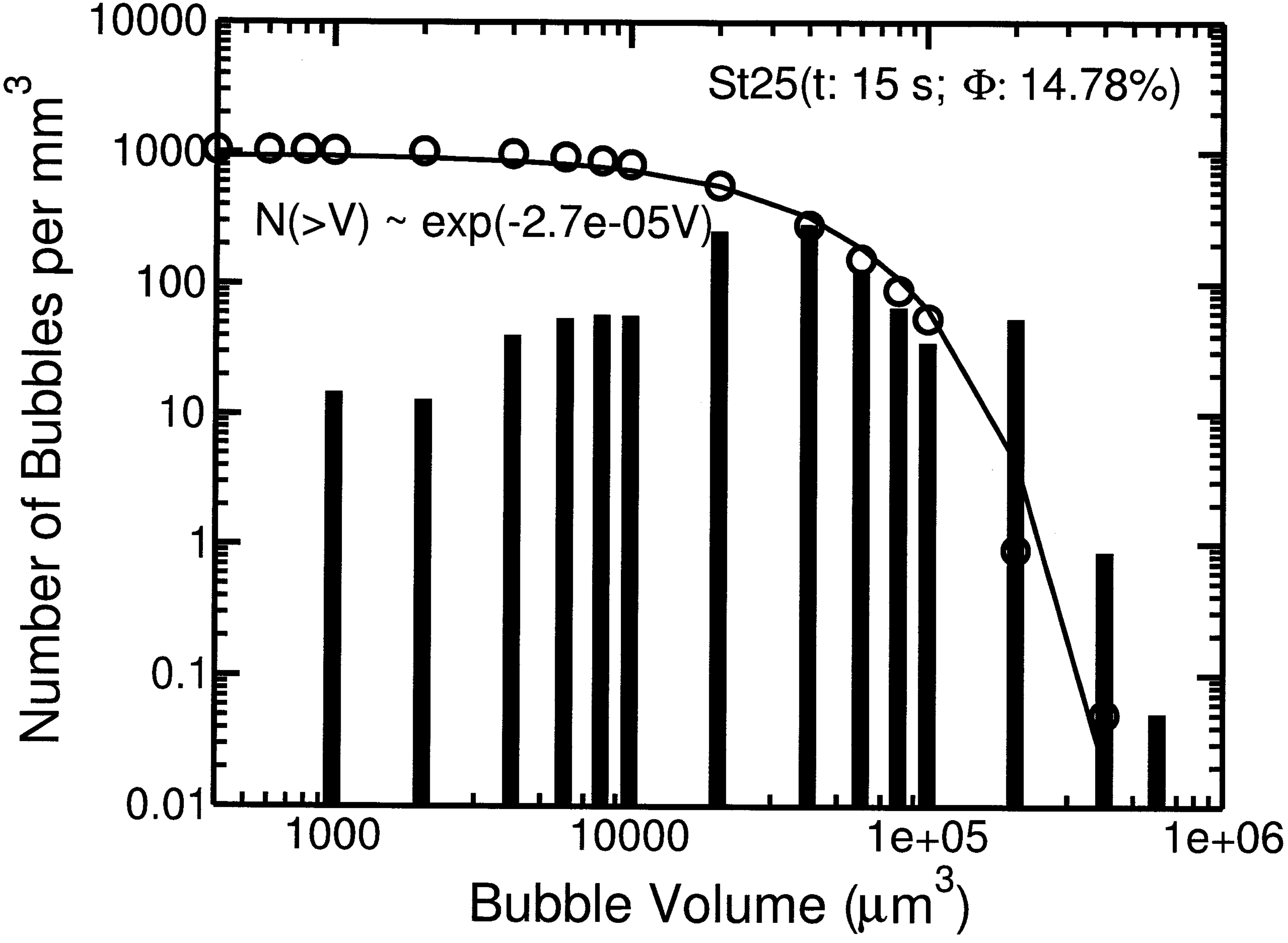
St25(t: 15 s; Φ: 14.78%)
N(>V) ~ exp(-2.7e-05V)
Number of Bubbles per mm$^3$
10000
1000
100
10
1
0.1
0.01
1000
10000
1e+05
1e+06
Bubble Volume (μm$^3$)

# APPENDIX III: MPG MOVIES

**St84ab:** Degassing sample St84ab observed by radiography.

**St84c:** Degassing sample St84c observed by radiography.